Volume 1, Issue 1 **2013**

INTERFACIAL PHENOMENA AND HEAT TRANSFER

International Journal of Interfacial Phenomena and Heat Transfer from Macro- to Nano- Scale Systems

EDITOR-IN-CHIEF
OLEG A. KABOV (Russia)

ASSOCIATE EDITORS
ALIDAD AMIRFAZLI (Canada)
HARUHIKO OHTA (Japan)

begell
New York · Connecticut

INTERFACIAL PHENOMENA AND HEAT TRANSFER

International Journal of Interfacial Phenomena and Heat Transfer from Macro- to Nano- Scale Systems

AIMS AND SCOPE

Interfacial Phenomena and Heat Transfer aims to serve as a forum to advance understanding of fundamental and applied areas on interfacial phenomena, fluid flow, and heat transfer through interdisciplinary research. The special feature of *Interfacial Phenomena and Heat Transfer* is to highlight multi-scale phenomena involved in physical and/or chemical behaviors in the context of both classical and new unsolved problems of thermal physics, fluid mechanics, and interfacial phenomena. Our goal is fulfilled by publishing novel research on experimental, theoretical and computational methods, assigning priority to comprehensive works covering at least two of the above three approaches. The scope of the Journal covers interdisciplinary areas of physics of fluids, heat and mass transfer, physical chemistry and engineering in macro-, meso-, micro-, and nano-scale. As such, review papers, full-length articles, and short communications are sought on the following areas: intense heat and mass transfer systems; flows in channels and complex fluid systems; physics of contact line, wetting and thermocapillary flows; instabilities and flow patterns; two-phase systems behavior including films, drops, rivulets, spray, jets, and bubbles; phase change phenomena such as boiling, evaporation, condensation and solidification; multi-scaled textured, soft or heterogeneous surfaces; and gravity dependent phenomena, e.g., processes in micro- and hyper-gravity. Significant contributions related to the development of innovative experimental techniques, and instrumentation demonstrating advancement of science in the focus areas of this publication, may also be considered.

Interfacial Phenomena and Heat Transfer:*International Journal of Interfacial Phenomena and Heat Transfer from Macro- to Nano-Scale Systems* (ISSN 0000-0000) is published quarterly and owned by Begell House, Inc., 50 Cross Highway, Redding, Connecticut 06896.

Copyright® 2013 by Begell House, Inc. All rights reserved. Printed in the United States of America. Authorization to photocopy items for internal or personal use, or the internal or personal use of specific clients, is granted by Begell House, Inc. for libraries and other users registered with the Copyright Clearance Center (CCC). Transactional Reporting Service, provided that the base fee of $35.00 per copy, plus .00 per page is paid directly to CCC, 222 Rosewood Drive, Danvers, MA 01923, USA. For those organizations that have been granted a photocopy license by CCC, a separate payment system has been arranged. The fee code for users of the Transactional Reporting Service is: [ISSN 0000-000/13/$35.00 + $0.00]. The fee is subject to change without notice. Begell House, Inc.'s consent does not extend to copying for general distribution, for promotion, for creating new works, or for resale. Specific permission must be obtained from Begell House, Inc., for such copying.

Subscriptions: United States rates for 2013 is $967.00. For orders outside the United State and Canada please add an additional $10.00 per issue for foreign airmail shipping and handling fees. All subscriptions are payable in advance. Subscriptions are entered on an annual basis, i.e., January to December. For immediate service and charge card sales, call Begell House at (203) 938-1300. Monday through Friday, 9 A.M.-5 P.M. EST. To order by fax: (203) 938-1304. Send written orders to Begell House, Inc., Subscriptions Department, 50 Cross Highway, Redding, Connecticut 06896. This journal contains information from authentic and highly regarded sources. Reprinted material is quoted with permission, and sources are indicated. A wide variety of references are listed. Reasonable efforts have been made to publish reliable data and information, but the editor and the publisher assume no responsibility for any statements of fact or opinion expressed in the published papers or in the advertisements.

Published: June 30, 2013

EDITOR-IN-CHIEF

OLEG A. KABOV
Kutateladze Institute of Thermophysics
Siberian Branch of Russian Academy of Sciences
Lavrentiev avenue, 1, Novosibirsk, 630090, Russia
Email: kabov@itp.nsc.ru

ASSOCIATE EDITORS

ALIDAD AMIRFAZLI
Department of Mechanical Engineering
York University
Toronto, ON, Canada M3J 1P3
E-mail: alidad.amirfazli@lassonde.yorku.ca

HARUHIKO OHTA
Department of Aeronautics and Astronautics
Faculty of Engineering
Kyushu University
Motooka 744, Nishi-ku, Fukuoka 819-0395, Japan
E-mail: ohta@aero.kyushu-u.ac.jp

EDITORS' ASSISTANTS

DR. ELENA F. BYKOVSKAYA
Kutateladze Institute of Thermophysics
Siberian Branch of Russian Academy of Sciences
Lavrentiev avenue, 1,
Novosibirsk, 630090, Russia
E-mail: bykovskaya@itp.nsc.ru

DR. DMITRY V. ZAITSEV
Kutateladze Institute of Thermophysics
Siberian Branch of Russian Academy of Sciences
Lavrentiev avenue, 1,
Novosibirsk, 630090, Russia
E-mail: zaitsev@itp.nsc.ru

EDITORIAL BOARD

YUTAKA ABE
Chair, Department of Engineering Mechanics and Energy
Professor, Faculty of Engineering, Information and Systems
University of Tsukuba, 1-1-1 Tennoudai,
Tsukuba, Ibaraki 305-8573, Japan
E-mail: abe@kz.tsukuba.ac.jp

VLADIMIR AJAEV
Southern Methodist University, Department of Mathematics,
Dallas, Texas 75275-0156, USA
E-mail: ajaev@smu.edu

SERGEY V. ALEKSEENKO
Director, Kutateladze Institute of Thermophysics, Siberian
Branch of Russian Academy of Sciences
1, Lavrentiev avenue, Novosibirsk, 630090, Russia
E-mail: aleks@itp.nsc.ru

DAVID BRUTIN
Associate Professor; Dept. of Mechanical Engineering
Aix-Marseille University, IUSTI UMR 7343 CNRS
5 rue Enrico Fermi; 13453 Marseille, France
E-mail: dbrutin@yahoo.fr

AVRAM BAR-COHEN
Distinguished University Professor
President, Assembly of International Heat Transfer Conf.
Editor, Encyclopedia of Thermal Packaging (WSPC)
University of Maryland, Department of Mechanical Engineering
2106B Glenn Martin Hall, College Park, MD 20742, USA
E-mail: abc@umd.edu

BO-FENG BAI
State Key Laboratory of Multiphase Flow in Power Engineering
School of Energy and Power Eng., X'an Jiaotong University
No.28, Xianing West Street, Xi'an, 710049, China
E-mail: bfbai@mail.xjtu.edu.cn

RICHARD J. BRAUN
University of Delaware
Department of Mathematical Sciences
Newark DE 19716, USA
E-mail: braun@math.udel.edu

LUIS ANTONIO DAVALOS-OROZCO
Instituto de Investigaciones en Materiales
Departamento de Polimeros
Universidad Nacional Autonoma de Mexico
Ciudad Universitaria, Circuito Exterior S/N
Delegación Coyoacán, 10000 México D. F., México
E-mail: ldavalos@unam.mx

JAVIER ALBERTO DIEZ
Instituto de Física Arroyo Seco
Facultad de Ciencias Exactas,
Universidad Nacional del Centro
de la Provincia de Buenos Aires
Pinto 399, 7000, Tandil, Argentina
E-mail: jdiez@exa.unicen.edu.ar

ANDREY G. FEDOROV
Georgia Institute of Technology,
George W. Woodruff School of Mechanical Engineering
Parker H. Petit Inst. for Bioengineering and Bioscience
Love Bldg. Room 307, 771 Ferst Drive
Atlanta, Georgia 30332-0405, USA
E-mail: andrei.fedorov@me.gatech.edu

MANOLIS GAVAISES
Director of the Energy and Transport Research Centre
City University London, Room: C171, Northampton Square
London EC1V 0HB, United Kingdom
E-mail: M.Gavaises@city.ac.uk

HANG GUO
Beijing University of Technology
College of Environmental & Energy Engineering
Beijing, 100124, P.R. China
E-mail: hangguo@bjut.edu.cn**SANG W. JOO**
Yeungnam University
School of Mechanical Engineering
Gyongsan 712-749, Korea
E-mail: swjoo@ynu.ac.kr

SAMEER KHANDEKAR
P. K. Kelkar Research Fellow
Indian Institute of Technology Kanpur
Department of Mechanical Engineering
Kanpur (UP) 208016 India
E-mail: samkhan@iitk.ac.in

ALEXANDER KUPERSHTOKH
Lavrentyev Institute of Hydrodynamics
Siberian Branch of Russian Academy of Sciences
Lavrentyev prosp. 15, Novosibirsk 630090, Russia
E-mail: skn@hydro.nsc.ru

FABRICE LEMOINE
Professor at University of Lorraine; Head of LEMTA
CNRS UMR – 7563 ; LEMTA-ENSEM;
2, avenue de la forêt de Haye
TSA60604 ; 54518 Vandoeuvre lès Nancy, France
E-mail: fabrice.lemoine@univ-lorraine.fr

QIU-SHENG LIU
Chinese Academy of Sciences, Institute of Mechanics National Microgravity Laboratory
15 Beisihuan Xilu, Beijing 100, China
E-mail: liu@imech.ac.cn

MARCO MARENGO
Associate Professor of Thermal Physics
Department of Industrial Engineering, University of Bergamo
viale Marconi 5, I-24044 Dalmine, Italy
E-mail: marco.marengo@unibg.it

YURI MUZYCHKA
Memorial University of Newfoundland
Faculty of Engineering and Applied Science
St. John's, Newfoundland, Canada
E-mail: y.s.muzychka@mun.ca

AMIR RIAZ
Department of Mechanical Engineering
University of Maryland; 3127 Martin Hall
College Park, MD 20742 USA
E-mail: ariaz@umd.edu

ILYA B. SIMANOVSKII
Technion - Israel Institute of Technology
Department of Mathematics
32000 Haifa, Israel
E-mail: cesima@tx.technion.ac.il

VALENTINA SHEVTSOVA
Université Libre de Bruxelles
Microgravity Research Centre
Chimie-Physique EP - CP165/62
Avenue F.D. Roosevelt, 50
B-1050 Bruxelles, Belgium
E-mail: vshev@ulb.ac.be

LOUNÈS TADRIST
Professor, Head of IUSTI Laboratory
Aix-Marseille Université, Polytech'Marseille
Laboratoire IUSTI,
UMR CNRS 7343
5, rue Enrico Fermi,
13453 Marseille Cedex 13, France
E-mail: lounes.tadrist@polytech.univ-mrs.fr

ICHIRO UENO
Department of Mechanical Engineering
Faculty of Science and Technology
Tokyo University of Science
2641 Yamazaki, Noda
Chiba 278-8510, Japan
E-mail: ich@rs.noda.tus.ac.jp

AMOS ULLMANN
Head, Environmental Engineering Program
School of Mechanical Engineering
Faculty of Engineering
Tel-Aviv University
Ramat Aviv 69978, Israel
E-mail: ullmann@eng.tau.ac.il

LESLIE YEO
RMIT University
School of Electrical and Computer Engineering
Micro/Nanophysics Research Laboratory
Melbourne, VIC 3000, Australia
E-mail: leslie.yeo@rmit.edu.au

JIAN-FU ZHAO
Chinese Academy of Sciences
Institute of Mechanics
National Microgravity Laboratory
15 Beisihuan Xilu, Beijing 100190, China
E-mail: jfzhao@imech.ac.cn

AUTHOR INSTRUCTIONS

INTERFACIAL PHENOMENA AND HEAT TRANSFER

(IPHT)

GENERAL INSTRUCTIONS: Articles should be submitted through the Begell House Online Submission Program by registering on the website (http://submission.begellhouse.com/) and then navigate to the IPHT submission site. Complete detailed Author Instructions can be found at http://www.begellhouse.com/journals/728e68e739b67efe.

SUBMISSION INSTRUCTIONS: If you are a first-time user of our Submission Program, begin on the home page, click on ***Journals*** from the list of products, then click on the ***New User*** icon located at the top of the screen. Please complete the registration form and then click on the ***Submit*** button at the bottom left side of the form. Your completed form will be reviewed and a registration confirmation will be emailed to you within 24 hours. Please make sure you keep your username and password available for further use on the submission site. Although you will have the option to change your password you should never register again on the submission site.

If you have previously completed a registration form please select the ***Journals*** item from the list of products, enter your username and password and click on the ***Login*** button.

PREPARATION OF ELECTRONIC ARTICLE FILES:

(1) Write in clear, concise English. The author is responsible for all aspects of article preparation. Extensive changes to the article will not be undertaken by the Editor or during the production process.

(2) **ORIGINAL ARTICLES SUBMITTED:** for possible publication in IPHT, the **initial manuscript** should be in a single file that includes all figures and tables in single column text and be submitted in either MS-Word or PDF format. Please use 12-point type and Times New Roman typeface for all text and figure captions. Please ensure that high quality figures and tables are provided and that any text that is an actual part of the figures be no less than 9-point type.

(3) **REVISIONS:** After your article has been reviewed the Editor will inform you if any revisions must be made before your article can be accepted for publication. If revisions are required you must upload your revised files onto the submission site using your original username and password. ***DO NOT*** register again on the submission site.

(4) **ACCEPTED ARTICLE:** After your article has been accepted for publication, please provide your electronic files in the following format: 12-point type, on US Letter (preferred) or A4, double spaced with 1-inch margins all around. Times New Roman is the preferred typeface for text. Acceptable formats for text files are Microsoft Word (using .doc extension) or LaTex. All pages should be numbered consecutively, centered at the bottom of each page. Your article should begin with the title information and end with pages containing references, tables, and figure legends. Figures must be submitted in either a separate file containing all figures or individual figure files. All figures must be labeled (example: 1, 2, 3, etc) clearly for proper placement within the text. Figures can be submitted in the following formats: word, tiff, jpeg, or eps. All files should be uploaded onto the submission site using your original username and password.

(5) **TRANSMITTAL AND COPYRIGHT FORM:** These forms can be found on the Begell House submission site when you upload your manuscript files. Each article submitted for publication must include a signed copyright form. All accepted articles, artwork, and photographs become the property of the publisher. Copyright forms can also be found in the Authors Hub (http://submission.begellhouse.com/). We also require that you fill out a transmittal form. The transmittal form includes the following information: article title, short title for running heads, keywords (no more than 10 keywords), and all author names (include affiliation and e-mail addresses). Corresponding authors must include their complete mailing address, e-mail address, telephone number, and fax number.

(6) **PERMISSIONS:** Authors are responsible for obtaining permission to reproduce copyrighted material from other sources and are required to sign an agreement for the transfer of copyright to the publisher. **ALL PERMISSIONS MUST BE INCLUDED WITH THE FINAL DRAFT OF YOUR ARTICLE.**

(7) **DECLARATION OF ORIGINALITY:** Each article submitted must be accompanied by a statement that the article has not been published elsewhere and that it has not been simultaneously submitted for publication elsewhere. The original electronic files of drawings, photos, and the article should be retained by the author until the conclusion of the publication process.

(8) **OTHER ITEMS:** All articles must include the following items:

Author Information: Senior authors full name, affiliation, and e-mail address. Corresponding authors complete mailing address and e-mail address. Co-authors' affiliation and email address.

Abstract: All articles must have an abstract not to exceed 250 words. Avoid abbreviations, diagrams, and reference to the text.

Key Words: All articles should have a list of key terms for indexing purposes. Three to ten key words or terms not in the title will assist indexers in cross-indexing your article.

Body: Group all tables, figures, and figure captions at the end of the article, following the references. Equations should be numbered sequentially. Use no more than two levels of headings. Number headings sequentially using numerals, as

follows: level 1 headings 1., 2., 3., etc.; level 2 headings 1.1., 2.1., etc. For articles containing more than a few symbols, include a nomenclature list in alphabetical order, with Greek symbols (also in alphabetical order and with a separate heading) following the alphabetical listing in English. The Nomenclature section should be placed after keywords and before the Introduction section. All articles must use SI units throughout; English units may be included parenthetically. The superscripts and subscripts should follow the Greek symbols at the end of the nomenclature list.

Figures: Prepare figures so that they do not exceed the size of the journal pages (size requirements can be obtained by emailing journals@begellhouse.com). Use only Arial and Symbol fonts for text within figures. Text/symbols within the figure must be at least a size 9 point after rescaling to the final publication format. Acceptable formats for figures are TIFF, JPEG, or EPS files saved from the original application at 300-600 dpi. Because of the loss of resolution, embedding figure files in MS Word is not recommended. **Please do not send final figures in PDF format.** The preferred format is TIFF; however, maintaining a clear quality of the figures is most important. Do not use gray rules, only black. If the text is printed over gray backgrounds for any reason, the gray must be at least 50% lighter than the text. If possible, avoid grayscales entirely. In general, for best results, figures must be submitted at the highest possible quality. Figure captions should be typed, on a separate sheet. The author can submit color figures that will print in black and white, but will be in color online. Color reproduction of figures is possible at the author's expense, rates will be provided upon request.

Tables: Tables should not be embedded in the text, but should be included at the end of the article. A short descriptive title should appear above each table with a clear legend and any footnotes suitably identified below. All units must be included.

LaTex File: If you are providing your final approved article in LaTex please follow all the above instructions, however, please also include a PDF file that is double spaced, no figures only figure captions at the end of the article.

Reference Format: Cite references in the text using the last name of the author(s) and the year of publication, either as "(Doe and Johnson, 1992) or "Doe and Johnson (1992)." For more than two authors, use "Doe et al. (1992)." If any references contain identical authors and year of publication, cite in the form "Doe et al. (1992a)" and "Doe et al. (1992b)." References should be in alphabetical order and formatted according to the following samples. Incorrectly formatted reference lists will be returned to the author for correction before acceptance.

- **Journal:** Nakayama, W. and Nakajima, T., (1982) Effects of Pore Diameters and System Pressure on Saturated Pool Nucleate Boiling Heat Transfer from Porous Surfaces, *J. Enhanced Heat Trans.*, 104(2), pp. 286–291.
- **Book:** Nield, D.A. and Bejan, A., (2005) *Convection in Porous Media,* New York: Springer- Verlag, pp. 125–176.
- **E-Books** Buyevich, Yu.A. and Alexandrov, D.V. (2005) *Heat Transfer in Dispersons*, Connecticut: Begell House, Available at http://www.edata-center.com/ebooks/b7f98f1e271b3e77a.html/ EBooks [accessed May 5, 2005]
- **Edited Book:** Yang, W. and Kim J.H. Eds., (1992) *Rotating Machinery*, New York: Begell House.
- **Chapters of Edited Book:** Nishikawa, K. and Ito, T., (1982) Augmentation of Nucleate Boiling Heat Transfer by Prepared Surfaces, In T. Mizushima and W.J. Yang, Eds., *Heat Transfer in Energy Problems*, Washington, D.C.: Hemisphere Publishing, pp. 111–1182.
- **Conference Proceedings:** Ma, T.M. (1987) Effects of Geometrical Shapes of Reentrant Grooves on Boiling Heat Transfer from Porous Surfaces, Heat Transfer 1986, *Proc. of 8th Intl. Heat Trans. Conf.*, vol. 4, pp. 2013–2018.
- **Dissertation:** Richmond, J., (2004) *Steady State Thermal Conductivity*, Ph.D. Thesis, University of Connecticut.
- **Footnotes:** Footnotes should be identified in the text by superscript Arabic numerals and cited consecutively within the paper. All footnotes should be compiled on a separate sheet.
- **Webpages: Nonperiodical Web Document -** Author, A. A. and Author, B. B. (Date of publication). *Title of document*. Retrieved month day, year, from http://Web address.
- **Chapter or Section of a Web document -** Author, A. A. and Author, B. B. (Date of publication). Title of article. In Title of book or larger document (chapter or section number). Retrieved month day, year, from http://www.someaddress.com/full/url/.
- **Online Scholarly Journal Article -** Author, A. A., & Author, B. B. (Date of publication). Title of article. *Title of Journal, volume number*. Retrieved month day, year, from http://www.someaddress.com/full/url/

REVIEW PROCESS: The Editor-in-Chief will seek reviews of submitted articles from appropriate experts and will assure rapid turnaround. Each article will be reviewed by at least two reviewers. Submission implies that the author is willing to make any necessary revisions. Retain all original figures until the conclusion of the publication process. Please upload your corrections onto the submission site.

AUTHOR PROOFS: A proof of the typeset article will be sent to the corresponding author for review and correction of technical information. Proofs should be carefully checked and returned promptly. Alterations made in proof should be absolutely minimal. The usual turnaround time for corrections is 48 hours (not counting weekends).

OFFPRINTS: An order form for offprints, copies of issues, subscriptions, and orders for color figures will be sent to the corresponding author with the author proofs. Authors who wish to purchase any of the above should fill out the order form and return it with author's corrections. Corresponding authors are asked to provide their co-authors with the above information. If you wish to order extra issues or offprints, please fill in the appropriate areas and submit with your corrections Corresponding Authors will receive a complimentary PDF file of their article upon publication of the journal issue in which the article will appear. This PDF file is for your own personal use and cannot be posted on any other websites or used for distribution purposes.

Interfacial Phenomena and Heat Transfer

Volume 1, Issue 1 **2013**

TABLE OF CONTENTS

Standing Symmetric Oscillations and Traveling Waves in Two-Layer Systems with Periodic Boundary Conditions **1**
I.B. Simanovskii

Enhanced Heat Transfer of Flow Boiling Combined with Jet Impingement **13**
J. Wei, Y. Zhang, J. Zhao, & D. Guo

Determination of Apparent Contact Angle and Shape of a Static Pendant Drop on a Physically Textured Inclined Surface **29**
G. Bhutani, K. Muralidhar, & S. Khandekar

Coalescence of a Droplet Cluster Suspended over a Locally Heated Liquid Layer **51**
A.A. Fedorets, I.V. Marchuk, & O.A. Kabov

Boiling Heat Transfer by Nucleate Boiling of Immiscible Liquids **63**
S. Onishi, H. Ohta, N. Ohtani, Y. Fukuyama, & H. Kobayashi

Instability and Rupture of Thin Liquid Films on Solid Substrates **81**
V.S. Ajaev

STANDING SYMMETRIC OSCILLATIONS AND TRAVELING WAVES IN TWO-LAYER SYSTEMS WITH PERIODIC BOUNDARY CONDITIONS

Ilya B. Simanovskii

Department of Mathematics, Technion – Israel Institute of Technology, 32000 Haifa, Israel, E-mail: cesima@tx.technion.ac.il

Nonlinear oscillatory convective flows developed under the joint action of buoyant and thermocapillary effects in the 47v2 silicone oil — water system with periodic boundary conditions on the lateral walls have been investigated. Two-dimensional convective regimes are studied by the finite difference method. Transitions between the flows with different spatial structures have been considered. Regimes of standing symmetric oscillations, traveling waves and modulated traveling waves have been found.

KEY WORDS: *instabilities, interface, two-layer system*

1. INTRODUCTION

Interfacial convection in systems with interfaces has been a subject of extensive investigation in the past few decades (for a review, see Simanovskii and Nepomnyashchy, 1993; Nepomnyashchy et al., 2012). Traditional fields of application of the interfacial convection are chemical engineering (Levich and Krylov, 1969) and materials processing (Szekely, 1979). Among the modern techniques requiring investigation of convection in systems with interfaces, one can mention the liquid encapsulation crystal growth technique (Doi and Koster, 1993) used in space laboratory missions, droplet — droplet coalescence processes, where the Marangoni convection in the interdroplet film can considerably affect the coalescence time during extraction (Groothuis and Zuiderweg, 1960), and others.

It is known that the stability problem for mechanical equilibrium in a system with an interface is not self-adjoint (see, e.g., Simanovskii and Nepomnyashchy, 1993; Renardy, 1996); thus an oscillatory instability is possible. The mechanism of oscillations, which develops without interfacial deformations due to the hydrodynamic and thermal interaction between convective flows on both sides of the interface, was found by Gershuni and Zhukhovitsky (1982) in the case of transformer oil — formic acid systems. The nonlinear oscillatory convective structures near the instability threshold for some model systems have been studied by Colinet and Legros (1994) and Renardy et al. (1999).

An oscillatory instability of the mechanical equilibrium can be caused by the joint action of buoyancy and thermocapillary effect in a two-layer system heated from below. This phenomenon was first discovered by Nepomnyashchy and Simanovskii (1984) (see also Simanovskii and Nepomnyashchy, 1993; Juel et al., 2000). Oscillations just above the instability threshold have been observed in experiments of Degen et al. (1998). It should be noted that the linear stability theory for the onset of the buoyancy convection has predicted a monotonic instability (Nepomnyashchy and Simanovskii, 2004). In our opinion, the oscillations observed in experiments by Degen et al. (1998) can be caused by the influence of the thermocapillary effect (Simanovskii and Nepomnyashchy, 2006).

In the present paper, nonlinear oscillatory convective regimes, developed under the joint action of buoyant and thermocapillary effects in the 47v2 silicone oil — water system with periodic boundary conditions on the lateral boundaries, have been studied. Regimes of standing symmetric oscillations, traveling waves and modulated traveling waves have been found.

2169–2785/13/$35.00 © 2013 by Begell House, Inc.

The paper is organized as follows. In Sec. 2, the mathematical formulation of the problem in the two-layer system is presented. The nonlinear approach is described in Sec. 3. Nonlinear simulations of the finite-amplitude convective regimes are considered in Sec. 4. Section 5 contains some concluding remarks.

2. FORMULATION OF THE PROBLEM

We consider a system of two horizontal layers of immiscible viscous fluids with different physical properties (see Fig. 1). The system is bounded from above and from below by two isothermal rigid plates kept at constant different temperatures (the total temperature drop is θ). It is assumed that the interfacial tension σ decreases linearly with an increase of the temperature: $\sigma = \sigma_0 - \alpha T$, where $\alpha > 0$. The variables referring to the top layer are marked by subscript 1, and the variables referring to the bottom layer are marked by subscript 2.

Assume that ρ_m, ν_m, η_m, κ_m, χ_m, β_m, and a_m are, respectively, density, kinematic and dynamic viscosity, heat conductivity, thermal diffusivity, thermal expansion coefficient, and the thickness of the mth layer ($m = 1, 2$). Let us introduce the following non-dimensional parameters, corresponding to parameter ratios of different fluids,

$$\rho = \rho_1/\rho_2, \quad \nu = \nu_1/\nu_2, \quad \eta = \eta_1/\eta_2,$$

$$\kappa = \kappa_1/\kappa_2, \quad \chi = \chi_1/\chi_2, \quad \beta = \beta_1/\beta_2,$$

and to the ratio of layer thicknesses,

$$a = a_2/a_1.$$

As the units of length, time, velocity, pressure, and temperature we choose a_1, a_1^2/ν_1, ν_1/a_1, $\rho_1\nu_1^2/a_1^2$, and θ, respectively.

The nonlinear equations of convection in the framework of the Boussinesq approximation for both fluids have the following form (see Simanovskii and Nepomnyashchy, 1993):

$$\begin{gathered}\frac{\partial \vec{v}_m}{\partial t} + (\vec{v}_m \cdot \nabla)\vec{v}_m = -e_m \nabla p_m + c_m \nabla^2 \vec{v}_m + b_m G T_m \vec{\gamma}, \\ \frac{\partial T_m}{\partial t} + \vec{v}_m \cdot \nabla T_m = \frac{d_m}{P} \nabla^2 T_m, \\ \nabla \cdot \vec{v}_m = 0.\end{gathered} \tag{1}$$

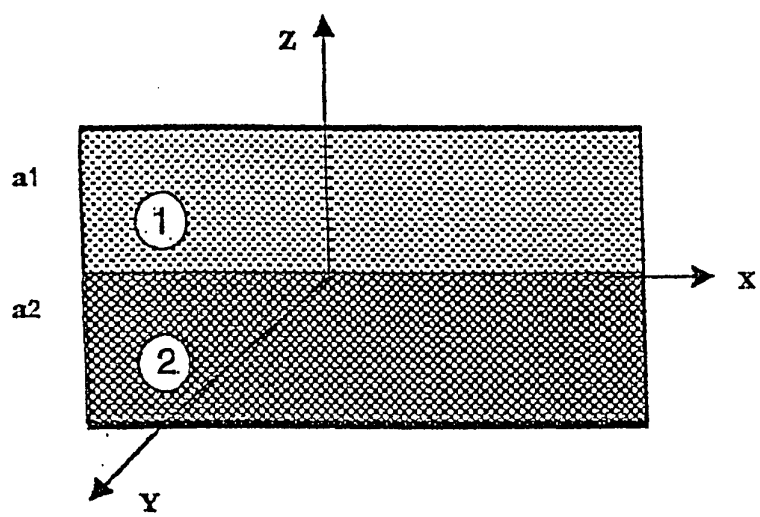

FIG. 1: Geometrical configuration of the two-layer system and coordinate axes.

Here $\vec{v}_m = (v_{mx}, v_{my}, v_{mz})$ is the velocity vector, T_m is the temperature, and p_m is the pressure in the mth fluid; $\vec{\gamma}$ is the unit vector directed upward; $b_1 = c_1 = d_1 = e_1 = 1$; $b_2 = 1/\beta$, $c_2 = 1/\nu$, $d_2 = 1/\chi$, $e_2 = \rho$; $G = g\beta_1\theta a_1^3/\nu_1^2$ is the Grashof number, which characterizes the buoyancy force, and $P = \nu_1/\chi_1$ is the Prandtl number for the liquid in layer 1. The conditions on the isothermal rigid horizontal boundaries are

$$z = 1: \quad \vec{v}_1 = 0; \quad T_1 = 0, \tag{2}$$

$$z = -a: \quad \vec{v}_2 = 0; \quad T_2 = 1. \tag{3}$$

The boundary conditions on the interface include relations for the tangential stresses:

$$z = 0: \quad \eta\frac{\partial v_{1x}}{\partial z} = \frac{\partial v_{2x}}{\partial z} + \frac{\eta M}{P}\frac{\partial T_1}{\partial x}, \quad \eta\frac{\partial v_{1y}}{\partial z} = \frac{\partial v_{2y}}{\partial z} + \frac{\eta M}{P}\frac{\partial T_2}{\partial x}; \tag{4}$$

the continuity of the velocity field:

$$v_1 = v_2; \tag{5}$$

the continuity of the temperature field:

$$T_1 = T_2; \tag{6}$$

and the continuity of the heat flux normal components:

$$\kappa\frac{\partial T_1}{\partial z} - \frac{\partial T_2}{\partial z} = 0. \tag{7}$$

Here $M = \alpha\theta a_1/\eta_1\chi_1$ is the Marangoni number, which is the basic nondimensional parameter characterizing the thermocapillary effect.

The problem (1)–(7) for any choice of parameters has the solution

$$\vec{v}_m^0 = 0, \quad p_m = p_m^0(z), \quad T_m = T_m^0(z), \quad m = 1, 2, \tag{8}$$

corresponding to the quiescent state. The temperature gradients in the quiescent state are

$$A_1 = dT_1^0/dz = -\frac{1}{(1+\kappa a)}, \quad A_2 = dT_2^0/dz = -\frac{\kappa}{(1+\kappa a)}. \tag{9}$$

Let us define the "local" Rayleigh numbers

$$R_m = \frac{g\beta_m|\bar{A}_m|a_m^4}{\nu_m\chi_m}, \quad m = 1, 2, \tag{10}$$

constructed using the parameters of the corresponding fluids ($\bar{A}_m$ is the dimensional temperature gradient in the mth fluid). The values of R_m are connected with the nondimensional parameters in the following way:

$$R_1 = \frac{GP}{1+\kappa a}, \quad R_2 = \frac{GP\kappa}{1+\kappa a}\frac{\nu\chi a^4}{\beta}. \tag{11}$$

The ratio of local Rayleigh numbers

$$r = \frac{R_2}{R_1} = \frac{\kappa\nu\chi a^4}{\beta} \tag{12}$$

depends on the physical properties of both fluids as well as on the ratio of layer thicknesses a. When the local Rayleigh numbers are close, one can observe the appearance of an oscillatory instability, if the linearized eigenvalue problem is not self-adjoint, i.e., if $\eta\beta\chi/\nu \neq 1$ (see Simanovskii and Nepomnyashchy, 1993).

3. NONLINEAR APPROACH

In order to investigate the flow regimes generated by the convective instabilities, we perform nonlinear simulations of two-dimensional flows [$v_{my} = 0$ ($m = 1, 2$); the fields of physical variables do not depend on y]. In his case we can introduce the stream function ψ:

$$v_{mx} = \frac{\partial \psi_m}{\partial z}, \quad v_{mz} = -\frac{\partial \psi_m}{\partial x}, \quad (m = 1, 2).$$

Eliminating the pressure and defining the vorticity

$$\phi_m = \frac{\partial v_{mz}}{\partial x} - \frac{\partial v_{mx}}{\partial z},$$

we can rewrite the boundary value problem (1)–(7) in the following form:

$$\frac{\partial \phi_m}{\partial t} + \frac{\partial \psi_m}{\partial z} \cdot \frac{\partial \phi_m}{\partial x} - \frac{\partial \psi_m}{\partial x} \cdot \frac{\partial \phi_m}{\partial z} = c_m \nabla^2 \phi_m + b_m G \frac{\partial T_m}{\partial t}, \tag{13}$$

$$\nabla^2 \psi_m = -\phi_m, \tag{14}$$

$$\frac{\partial T_m}{\partial t} + \frac{\partial \psi_m}{\partial z} \cdot \frac{\partial T_m}{\partial x} - \frac{\partial \psi_m}{\partial x} \cdot \frac{\partial T_m}{\partial z} = \frac{d_m}{P} \nabla^2 T_m \tag{15}$$

$$(m = 1, 2).$$

$$z = 1: \quad \psi_1 = \frac{\partial \psi_1}{\partial z} = 0; \quad T_1 = 0; \tag{16}$$

$$z = -a: \quad \psi_2 = \frac{\partial \psi_2}{\partial z} = 0; \quad T_2 = 1; \tag{17}$$

$$z = 0: \quad \psi_1 = \psi_2 = 0, \quad \frac{\partial \psi_1}{\partial z} = \frac{\partial \psi_2}{\partial z}, \quad \phi_2 = \eta \phi_1 + \frac{\eta M}{P} \frac{\partial T_1}{\partial x}; \tag{18}$$

$$T_1 = T_2, \quad \kappa \frac{\partial T_1}{\partial z} = \frac{\partial T_2}{\partial z}. \tag{19}$$

The calculations were performed in a finite region $-L/2 \le x \le L/2$, $-a \le z \le 1$ with the periodic boundary conditions

$$\psi_m(x + L, z) = \psi_m(x, z); \quad \phi_m(x + L, z) = \phi_m(x, z); \quad T_m(x + L, z) = T_m(x, z); \tag{20}$$

$$m = 1, 2,$$

where $L = l/a_1$.

The problem (13)–(20) is integrated in time with some initial conditions for ψ_m and T_m ($m = 1, 2$) by means of a finite-difference method. Equations and boundary conditions are approximated on a uniform mesh using a second-order approximation for the spatial coordinates. The nonlinear equations are solved using an explicit scheme on a rectangular uniform mesh 84×84. We checked the results on 112×112 and 168×168 meshes. The relative changes of the stream function amplitudes for all the mesh sizes do not exceed 1.5%. The variation of vortices at the corners of the region is about 2.5%. The Poisson equation is solved by the iterative Liebman successive over-relaxation method on each time step. The accuracy of the solution is 10^{-5}.

At the interface the expression for the vorticity is approximated with the second-order accuracy for the spatial coordinates and has a form

$$\phi_1(x, 0) = \frac{-2[\psi_2(x, -\triangle z) + \psi_1(x, \triangle z)]}{(\triangle z)^2 (1 + \eta)} - \frac{M}{P} \frac{\eta}{1 + \eta} \frac{\partial T_1(x, 0)}{\partial x}; \tag{21}$$

$$\phi_2(x, 0) = \eta \phi_1(x, 0) + \frac{M \eta}{P} \frac{\partial T_1(x, 0)}{\partial x}. \tag{22}$$

Here $\triangle x$, $\triangle z$ are the mesh sizes for the corresponding coordinates. The temperatures on the interfaces were calculated by the second-order approximation formulas:

$$T_1(x,0) = T_2(x,0) = \frac{[4T_2(x,-\triangle z) - T_2(x,-2\triangle z)] + \kappa[4T_1(x,\triangle z) - T_1(x,2\triangle z)]}{3(1+\kappa)}. \tag{23}$$

The details of the numerical method can been found in the book by Simanovskii and Nepomnyashchy (1993).

4. NUMERICAL RESULTS

We investigate the nonlinear regimes of convection in the 47v2 silicone oil-water system (the Rhodorsil Oil 47 is polydimethylsiloxane oil with a viscosity 2 mm^2/s) with the following set of parameters: $\nu = 2.0$; $\eta = 1.7375$; $\kappa = 0.184$; $\chi = 0.778$; $\beta = 5.66$; $P = 25.7$. The given system has been taken because of the following reasons. First, this system was used in experiments carried out by Degen et al. (1998). Also, for the system under consideration, the value of the "non-self-adjointness" parameter $\eta\beta\chi/\nu = 3.83$ is rather far from 1, which is favorable for the appearance of an oscillatory instability (see Simanovskii and Nepomnyashchy, 1993).

To simulate the motions in a laterally infinite two-layer system, we use periodic boundary conditions (20) for $L = 2.74$. Let us take the ratio of the layer thicknesses $a = 1$.

In the case $r > 1$, where the buoyancy convection develops mainly in the bottom layer, a temperature disturbance on the interface generates buoyancy volume forces and thermocapillary tangential stresses acting in the same direction. In this case, the monotonic instability of the mechanical equilibrium takes place.

In the opposite case $r < 1$ [for the system under consideration $r = 0.0506$, see (12)], where the buoyancy convection develops mainly in the top layer, a temperature disturbance on the interface generates buoyancy volume forces and the thermocapillary tangential stresses acting in the opposite way. The asynchronic action of these two factors working in the opposite direction can produce oscillations.

Under the conditions of the experiment, when the geometric configuration of the system is fixed while the temperature difference θ is changed, the Marangoni number M and the Grashof number G are proportional. We define the inverse dynamic Bond number

$$K = \frac{M}{GP} = \frac{\alpha}{g\beta_1\rho_1 a_1^2}.$$

Let us fix $K = 0.025$.

When the Grashof number is sufficiently small, disturbances decay in an oscillatory way and the system keeps the mechanical equilibrium. With an increase of the Grashof number ($G \geq G_* = 93.5$), the mechanical equilibrium state becomes unstable and a *perfectly symmetric standing wave* (type 1) develops near the instability threshold.

In order to describe the time evolution of the solution, we use four integral variables defined in the following way:

$$S_{l1}(t) = \int_0^{L/2} dx \int_0^1 dz \psi_1(x,z,t), \quad S_{r1}(t) = \int_{L/2}^{L} dx \int_0^1 dz \psi_1(x,z,t), \tag{24}$$

$$S_{l2}(t) = \int_0^{L/2} dx \int_{-a}^0 dz \psi_2(x,z,t), \quad S_{r2}(t) = \int_{L/2}^{L} dx \int_{-a}^0 dz \psi_2(x,z,t). \tag{25}$$

The time evolution of quantities $S_{lm}(t)$, $m = 1, 2$, for different values of the Grashof number is shown in Fig. 2. Close to the threshold, oscillations are of rather simple, almost sinusoidal form (lines 1a, 2a in Fig. 2). At the larger values of G, the period of oscillations decreases and oscillations become rather complicated (lines 1c, 2c in Fig. 2). The corresponding phase trajectories constructed in the plane (S_{l1}, S_{l2}) confirm the periodicity of oscillations and show a significant phase delay of the oscillations in the top layer with respect to the oscillations in the bottom layer (see Fig. 3). Snapshots of streamlines for the symmetric standing wave at $G = 101.7$ are presented in Fig. 4. This oscillatory regime is characterized by the symmetry properties:

$$\psi_m(L-x,z,t) = -\psi_m(x,z,t), \quad T_m(L-x,z,t) = T_m(x,z,t), \quad m = 1,2. \tag{26}$$

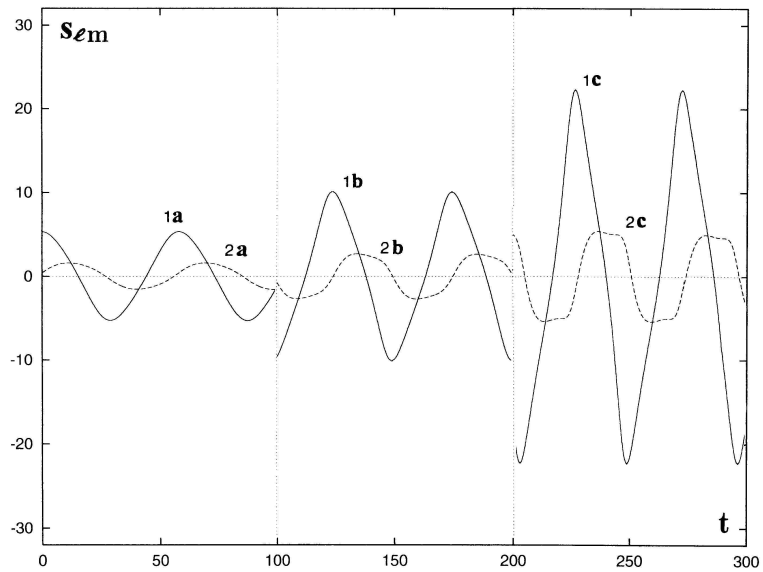

FIG. 2: Dependencies of $S_{l,m}$ on time ($m = 1, 2$) at $G = 95.2$ (lines 1a, 2a); 98.0 (lines 1b, 2b); 101.7 (lines 1c, 2c); $K = 0.025$; $L = 2.74$; $a = 1$.

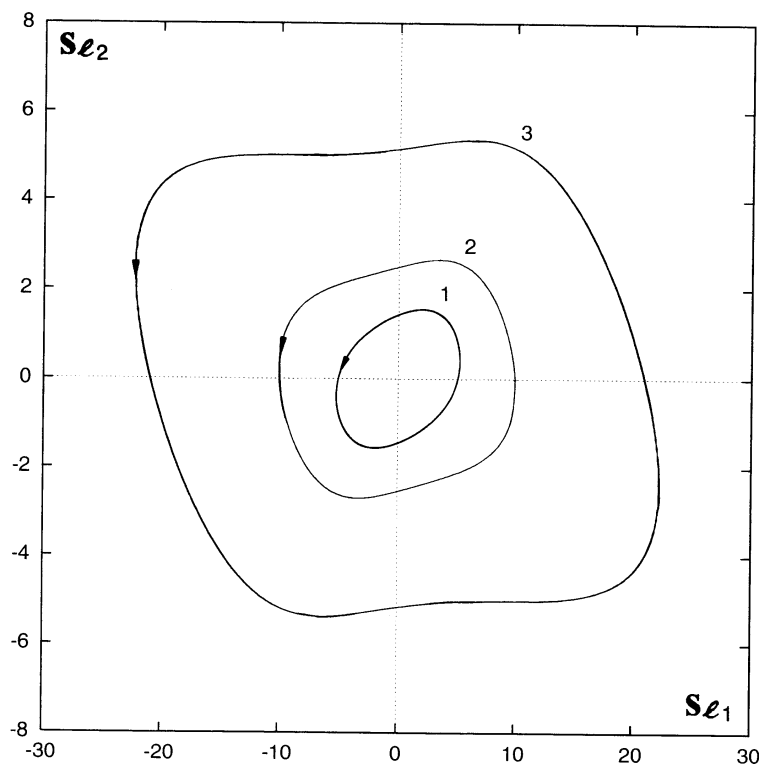

FIG. 3: Phase trajectories in the plane (S_{l1}, S_{l2}) for symmetric oscillatory flows at $G = 95.2$ (line 1); 98.0 (line 2); 101.7 (line 3); $K = 0.025$; $L = 2.74$; $a = 1$.

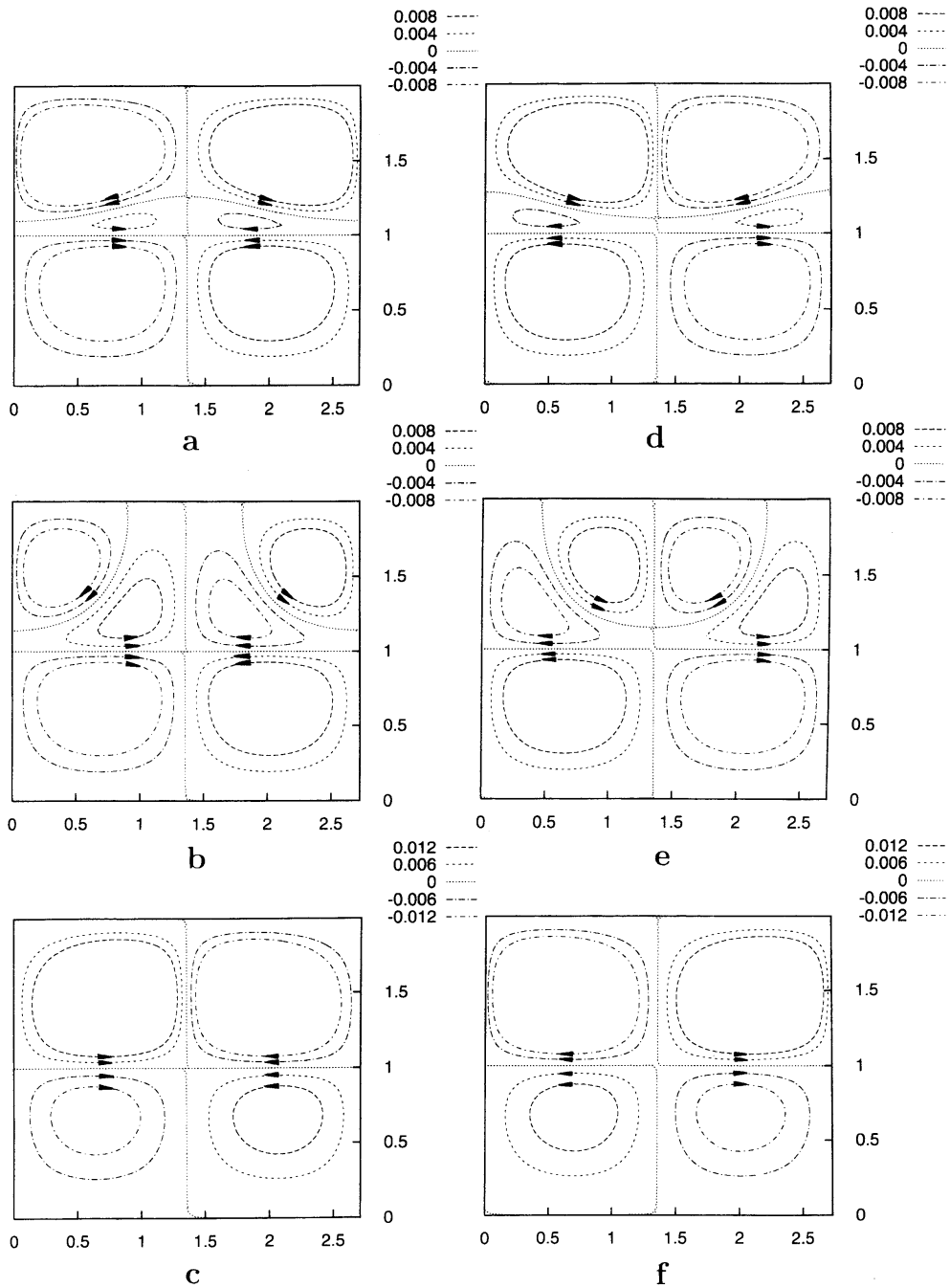

FIG. 4: (a)–(f) A time sequence of snapshots of streamlines for the symmetric time-periodic motion during one period at $G = 101.7$; $K = 0.025$; $L = 2.74$; $a = 1$.

One can see that during one half of the period the corresponding vortices change the direction of rotation [cf. Figs. 4(a) and 4(d)].

At $G \geq G_* = 106$, the standing wave becomes unstable and *a traveling wave* (type 2) develops in the system (see Figs. 5 and 6):

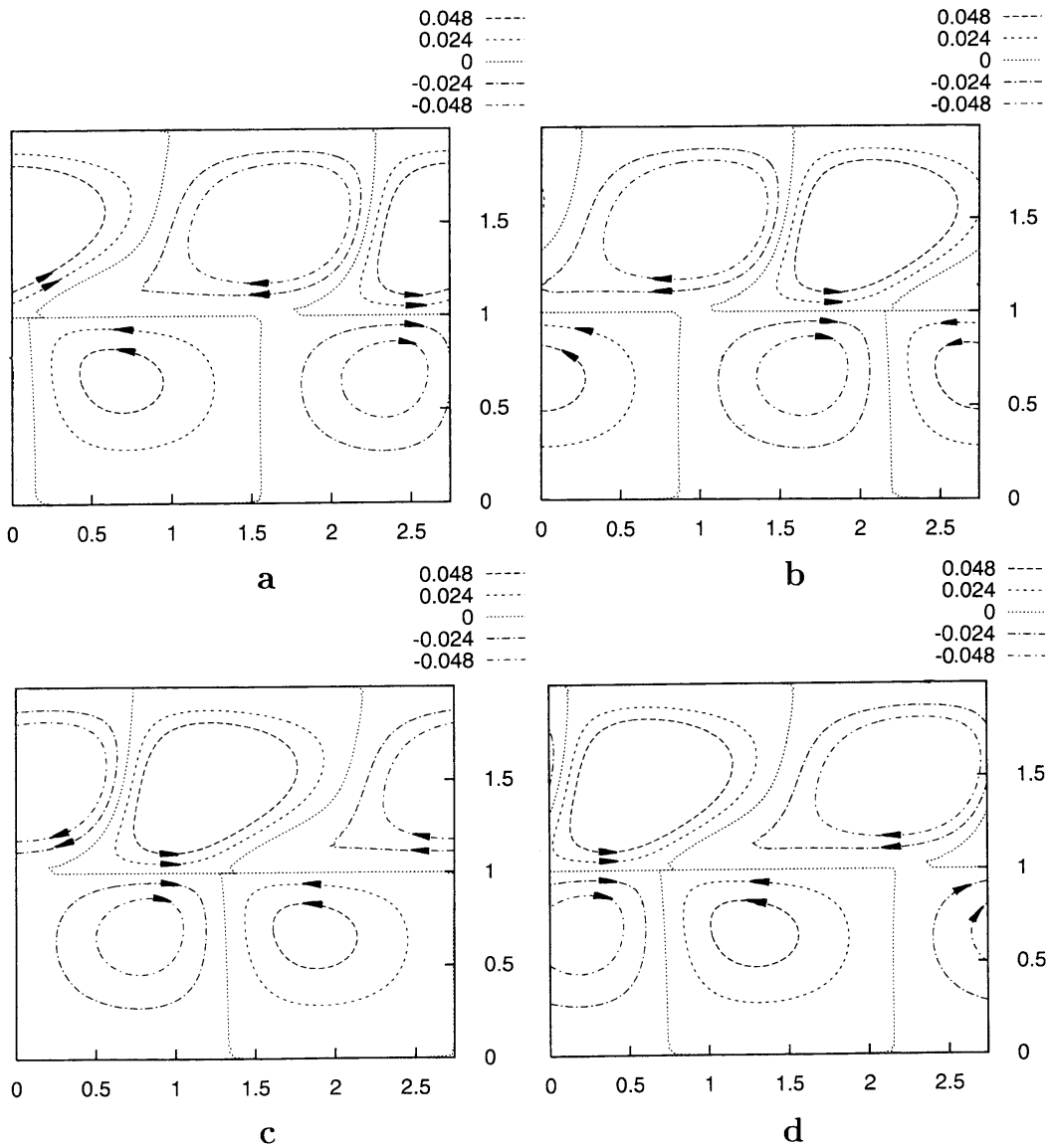

FIG. 5: (a)–(d) A time sequence of snapshots of streamlines for the traveling wave at $G = 153$; $K = 0.025$; $L = 2.74$; $a = 1$. The wave moves from the right- to the left-hand side.

$$\psi_m(x, z, t) = \psi_m(x - ct, z), \quad T_m(x, z, t) = T_m(x - ct, z), \tag{27}$$

where c is the phase velocity of the traveling wave. The time evolution of quantities $S_{lm}(t)$, $m = 1$, 2, and the corresponding phase trajectories in the plane (S_{l1}, S_{l2}), are presented in Figs. 7 and 8. The phase trajectory in Fig. 8, shows a significant phase delay of the oscillations in the top layer with respect to the oscillations in the bottom layer.

With an increase of the Grashof number, the traveling wave becomes unstable and at $G > 158$, *the modulated traveling wave* (type 3) appears in the system. The phase trajectory in the plane (S_{l1}, S_{l2}) is presented in Fig. 9. At the larger values of the Grashof number ($G > 187.2$), the modulated traveling wave disappears and the system makes a transition to the steady four-vortex flow. The stream lines and the isotherms of the steady state are shown in Fig. 10.

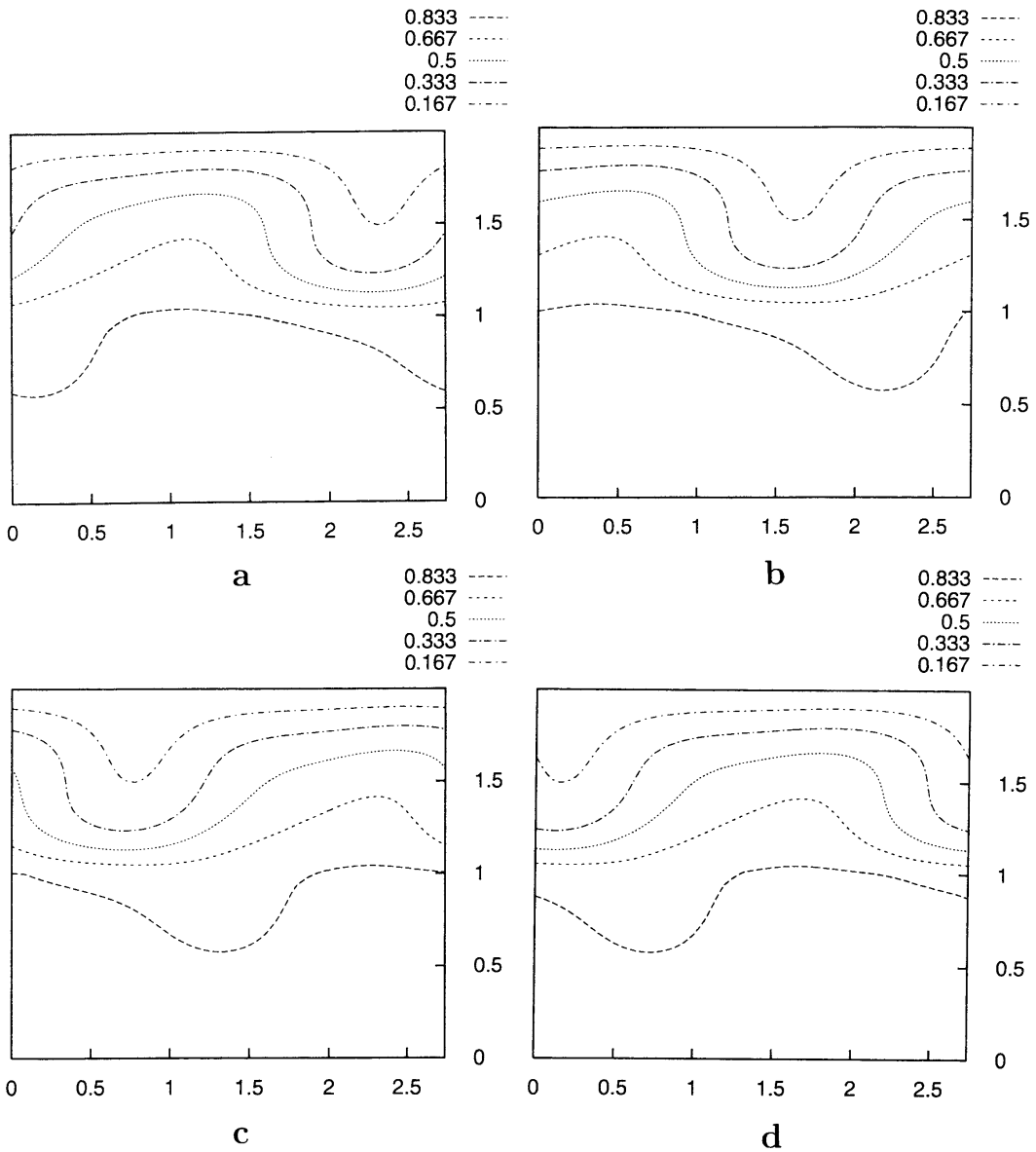

FIG. 6: (a)–(d) A time sequence of isotherms for the traveling wave at $G = 153$; $K = 0.025$; $L = 2.74$; $a = 1$.

One can see that the corresponding vortices in the top and bottom layers rotate in the opposite direction [Fig. 10(a)] and the isotherms in both layers are distorted in the opposite way [Fig. 10(b)]. Let us note that the stability regions of the modulated traveling wave and a stationary convection are overlapped.

5. CONCLUSION

The nonlinear development of the oscillatory instability in a two-layer system in the presence of buoyancy and the thermocapillary effect is investigated. Periodic boundary conditions on the lateral boundaries have been considered. Transitions between the flows with different spatial structures have been studied. It is shown that under the joint action of buoyancy and the thermocapillary effect, the development of oscillatory instability can lead to the appearance of

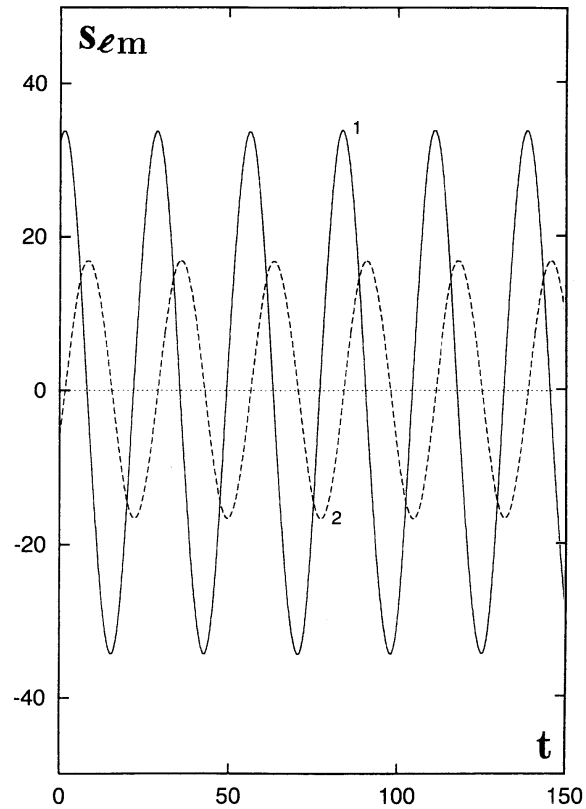

FIG. 7: Dependencies of $S_{l,1}$ (line 1) and $S_{l,2}$ (line 2) on time at $G = 153$; $K = 0.025$; $L = 2.74$; $a = 1$.

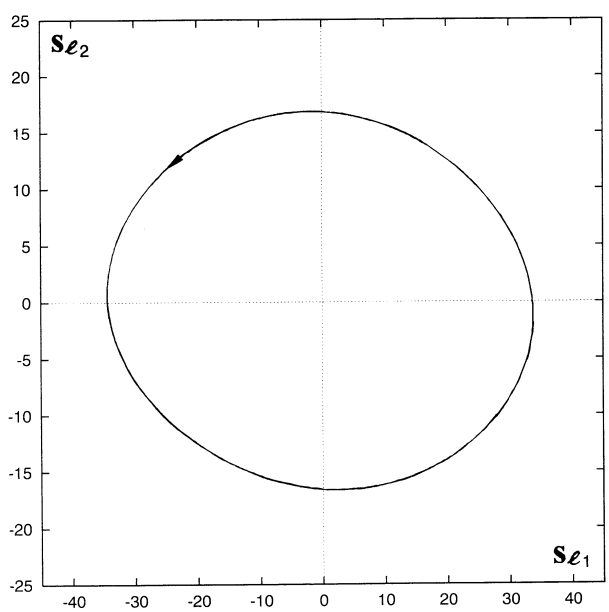

FIG. 8: Phase trajectory in the plane (S_{l1}, S_{l2}) for the traveling wave at $G = 153$; $K = 0.025$; $L = 2.74$; $a = 1$.

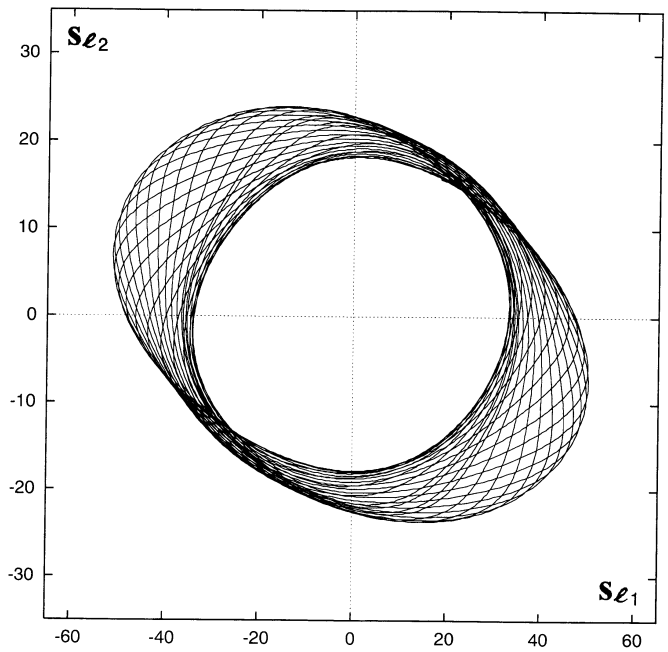

FIG. 9: Phase trajectory in the plane (S_{l1}, S_{l2}) for the modulated traveling wave at $G = 179$; $K = 0.025$; $L = 2.74$; $a = 1$.

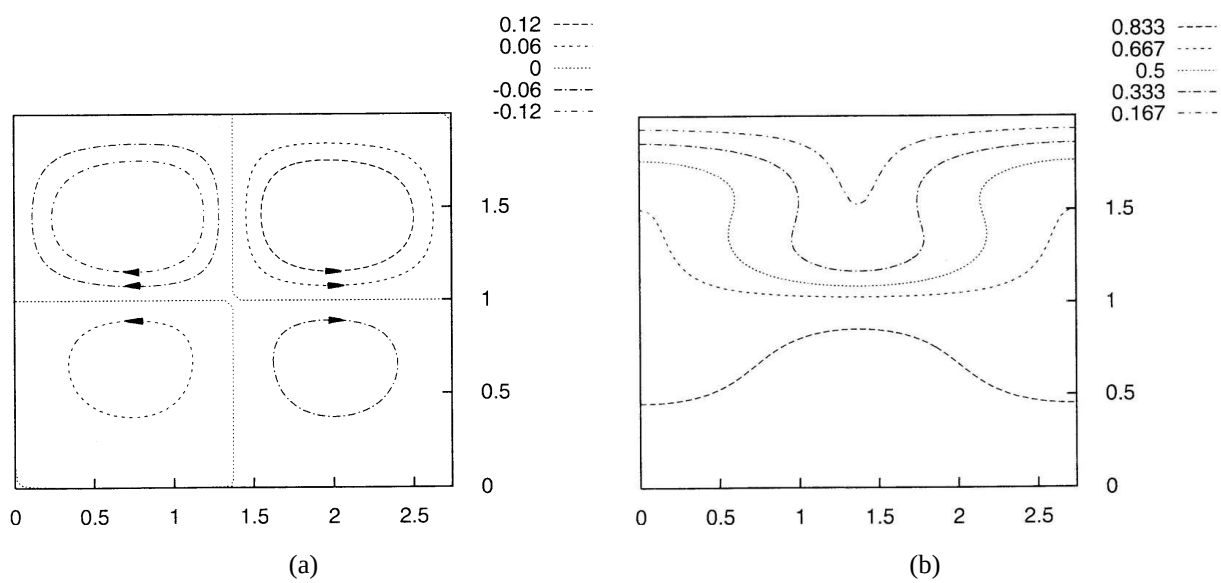

FIG. 10: (a) Streamlines and (b) isotherms for the symmetric steady state at $G = 190$; $K = 0.025$; $L = 2.74$; $a = 1$.

different nonsteady flows. Specifically, regimes of standing symmetric oscillations, traveling waves and modulated traveling waves have been found. It is shown that nonlinear oscillatory flows exist in a finite interval of the Grashof number values, between the stability regions of a mechanical equilibrium and a stationary convection.

REFERENCES

Colinet, P. and Legros, J. C., On the Hopf bifurcation occuring in the two-layer Rayleigh-Bénard convective instability, *Phys. Fluids*, vol. **6**, pp. 2631–2639, 1994.

Degen, M. M., Colovas, P. W., and Andereck C. D., Time-dependent patterns in the two-layer Rayleigh-Bénard system, *Phys. Rev. E*, vol. **57**, pp. 6647–6659, 1998.

Doi, T. and Koster, J. N., Thermocapillary convection in two immiscible layers with free surface, *Phys. Fluids*, vol. **A5**, pp. 1914–1927, 1993.

Gershuni, G. Z. and Zhukhovitsky, E. M., On monotonic and oscillatoty instability of a two-layer immiscible fluids system heated from below, *Sov. Phys. Dokl.*, vol. **27**, pp. 531–533, 1982.

Groothuis, H. and Zuiderweg, F. G., Influence of mass transfer on coalescence of drops, *Chem. Eng. Sci*, vol. **12**, pp. 288–289, 1960.

Juel, A., Burgess, J. M., McCormick, W. D., Swift, J. B., and Swinney, H. L., Surface-tension-driven convection patterns in two liquid layers, *Physica D*, vol. **143**, pp. 169–186, 2000.

Levich, V. G. and Krylov, V. S., Surface-tension-driven phenomena, *Annu. Rev. Fluid. Mech.*, vol. **1**, pp. 293–316, 1969.

Nepomnyashchy, A. A. and Simanovskii, I. B., Thermocapillary and thermogravitational convection in a two-layer system with a distorted interface, *Fluid Dyn.*, vol. **19**, pp. 494–499, 1984.

Nepomnyashchy, A. A. and Simanovskii, I. B., Influence of thermocapillary effect and interfacial heat release on convective oscillations in a two-layer system, *Phys. Fluids*, vol. **16**, pp. 1127–1139, 2004.

Nepomnyashchy, A. A., Simanovskii, I. B., and Legros, J. C., *Interfacial Convection in Multilayer Systems*, 2nd ed., New York: Springer, 2012.

Renardy, Y. Y., Pattern formation for oscillatory bulk-mode competition in a two-layer Bénard problem, *Z. Angew. Math. Phys.*, vol. **47**, pp. 567–590, 1996.

Renardy, Y., Renardy, M., and Fujimura, K., Takens-Bogdanov bifurcation on the hexagonal lattice for double-layer convection, *Physica D*, vol. **129**, p. 171, 1999.

Simanovskii, I. B. and Nepomnyashchy, A. A., *Convective Instabilities in Systems with Interface*, London: Gordon and Breach, 1993.

Simanovskii, I. B. and Nepomnyashchy, A. A., Nonlinear development of oscillatory instability in a two-layer system under the combined action of buoyancy and thermocapillary effect, *J. Fluid Mech.*, vol. **555**, pp. 177–202, 2006.

Szekely, J., *Fluid Flow Phenomena in Metals Processing*, New York: Academic, 1979.

ENHANCED HEAT TRANSFER OF FLOW BOILING COMBINED WITH JET IMPINGEMENT

Jinjia Wei,[1,*] Yonghai Zhang,[1] Jianfu Zhao,[2] & Dong Guo[3]

[1]*State Key Laboratory of Multiphase Flow in Power Engineering, Xi'an Jiaotong University, Xi'an, 710049, China*

[2]*Key Laboratory of Microgravity (National Microgravity Laboratory)/CAS, Institute of Mechanics, Chinese Academy of Sciences, 100190, Beijing*

[3]*YanTai WanHua Group, YanTai, 264000, China*

[*]Address all correspondence to Jinjia Wei, E-mail: jjwei@mail.xjtu.edu.cn

The experiment was made at flow boiling heat transfer of FC-72 on micro-pin-finned chips with jet impingement. The experimental conditions cover two different liquid subcooling degrees (25, 35 K), three different crossflow velocities (V_c = 0.5, 1, 1.5 m/s), and three different jet velocities (V_j = 0, 1, 2 m/s) in the direction perpendicular to chip surface. The dimension of the silicon chips is 10 mm × 10 mm × 0.5 mm (length × width × thickness) on which four kinds of micro-pin-fins with the dimensions of 30 × 30 × 60 μm^3, 50 × 50 × 60 μm^3, 30 × 30 × 120 μm^3, 50 × 50 × 120 μm^3 (width × thickness × height, named PF30-60, PF50-60, PF30-120, PF50-120) were fabricated using the dry etching technique. A smooth surface (named chip S) was also tested for comparison. The results have shown that flow boiling combined with jet impingement gives a large heat transfer enhancement compared with pool boiling and flow boiling. It has been also found that micro-pin-finned surfaces enhance heat transfer compared with the smooth surface. For all chips, the maximum q_{CHF} increases in the order of chips S, PF50-60, PF30-60, PF50-120, PF30-120, and q_{CHF} increases with crossflow or jet velocities. The maximum allowable heat flux $q_{\max}$ is given by the q_{CHF} if $T_{w,\mathrm{CHF}} < 85°$C and by q at $T_w = 85°$C, if $T_{w,\mathrm{CHF}} > 85°$C. Effects of liquid subcooling, surface structure, and boiling heat transfer mode on maximum allowable heat flux were also investigated in the present experiment, and the combination of these influence factors of maximum allowable heat flux exerts a synergistic effect. The maximum allowable heat flux of chip S is 15.1 W/cm^2 at $\Delta T_{\mathrm{sub}} = 25$ K by pool boiling, and the maximum allowable heat flux of micro-pin-fins by crossflow–jet combined boiling in the experiment is 167 W/cm^2, which is 11.06 times as large as that for the smooth surface without additional flow.

KEY WORDS: *flow boiling, jet impingement, micro-pin-fins, synergistic effect, FC-72*

1. INTRODUCTION

As is well known, with fast increase of signal speed for improving computer performance, electronic circuits become smaller and smaller, and integrated circuit densities become higher and higher, which leads to an increasing power dissipation rate from a unit area and a great increase in the chip temperature. The possible maximum junction temperature is about 85°C for most chips, and an electronic component operating 10 K beyond this temperature can reduce its reliability by as much as 50% (Nelson et al., 1978). The traditional air cooling method cannot meet the high heat flux requirement due to low thermal conductivity, so it is necessary to find an effective cooling method to remove the heat dissipation from chips. As an alternative scheme, liquid cooling is a promising way due to the high conductivity of liquid. There are two types of liquid cooling—indirect liquid cooling and direct liquid cooling. When boiling heat transfer with phase change occurs, heat dissipation ability from chips can be increased much more.

2169–2785/13/$35.00 © 2013 by Begell House, Inc.

NOMENCLATURE

h	height of micro-pin-fin (μm)
q	heat flux (W/cm^2)
q_{CHF}	critical heat flux (W/cm^2)
$q_{\max}$	maximum allowable heat flux (W/cm^2)
t	thickness of micro-pin-fin (μm)
T_b	bulk liquid temperature (K)
T_{sat}	boiling temperature (K)
T_w	wall temperature (K)
$T_{w,\mathrm{CHF}}$	wall temperature at critical heat flux (°C)
V_c	crossflow velocity in crossflow–jet combined boiling (m/s)
V_j	jet velocity in crossflow–jet combined boiling (m/s)

Greek Symbols

ΔT_b	temperature difference between wall and bulk liquid, $T_w - T_b$ (K)
ΔT_{sat}	wall superheat, $T_w - T_{\mathrm{sat}}$ (K)
ΔT_{sub}	liquid subcooling, $T_{\mathrm{sat}} - T_b$ (K)

For enhancing boiling heat transfer on chip surfaces, an effective method is to fabricate microstructures on the chip surfaces to generate so-called treated surfaces that have been found to have great potential in enhancement of boiling heat transfer from electronics, significantly reducing the chip surface temperature and increasing critical heat flux (CHF). Usually, treated surfaces are used for nucleate boiling enhancement by applying some microstructures on the chip surface to make the surface capable of trapping vapor and keeping the nucleation sites active or increasing effective heat transfer area. Until now, many kinds of microstructures have been observed, such as dendritic heat sink (Oktay and Schmeckenbecher, 1972), laser drilled holes (Hwang and Moran, 1981), microstructures including fins, studs, grooves, and vapor-trapping cavities (Anderson and Mudawar, 1989), reentrant cavities (Phadke et al., 1992), porous surfaces (O'Connor et al., 1995; Rainey et al., 2003), diamond particle (O'Connor et al., 1996), micro-reentrant cavities (Kubo et al., 1999), and carbon nanotubes coated on silicon and copper surfaces (Ujereh et al., 2007). On these surfaces boiling heat transfer can actually be enhanced by increasing nucleate site number and effective boiling heat transfer surface area. Compared with the smooth chip, the boiling curve of the treated surfaces shifts toward a smaller wall superheat, with a lower onset temperature of nucleate boiling and a higher CHF. However, the boiling heat transfer is severely deteriorated at high heat flux region, and the wall temperature at the CHF point is much larger than the upper temperature limit for normal operation of LSI chips, 85°C. The reason is that the heater surface is covered with bubbles in the high heat flux region, which prevents the fresh liquid from reaching the heater surface for evaporation.

As described above, a good microstructured surface should have a boiling curve with much smaller wall superheat, steeper slope, and larger CHF. Thus, a new surface treatment has to be developed for application in solving the power dissipation problems. Honda, Wei, and co-workers (Honda and Wei, 2003, 2004; Honda et al., 2002; Wei and Honda, 2003; Wei et al., 2005) made noticeable progress in nucleate boiling enhancement by use of micro-pin-fins (10–50 μm in thickness and 60–270 μm in height) which were fabricated on silicon surface using the dry etching technique. It is expected that the regular interconnected channels formed by the micro-pin-fins can provide a route for fresh liquid supply even at high heat fluxes. The liquid can be driven by capillary force caused by the bubbles staying on the top of the micro-pin-fins. Figure 1 shows the boiling performance of micro-pin-finned surfaces in the pool boiling case. It can be concluded that the boiling curves are almost vertical even in the high heat flux region, and the wall temperature at the CHF point is less than 85°C showing a large heat transfer enhancement compared with the smooth surface and the other treated surfaces. In the high heat flux region, although the micro-pin-finned surfaces are covered with large bubbles as microporous surfaces, the capillary force generated by the bubbles drives plenty of fresh liquid into contact with the superheated wall for vaporization through the regular interconnected structures, but also improves the micro-convective heat transfer by the motion of liquid around the micro-pin-fins. These produce high heat transfer efficiency until the capillary force arrives at its maximum value but it cannot overcome the hydraulic resistance of the wet liquid to access everywhere in the micro-pin-fins' interconnected channel with further increase of heat flux; then the liquid near some micro-pin-fins is used up due to a shortage of fresh liquid supply. A vapor patch is formed and

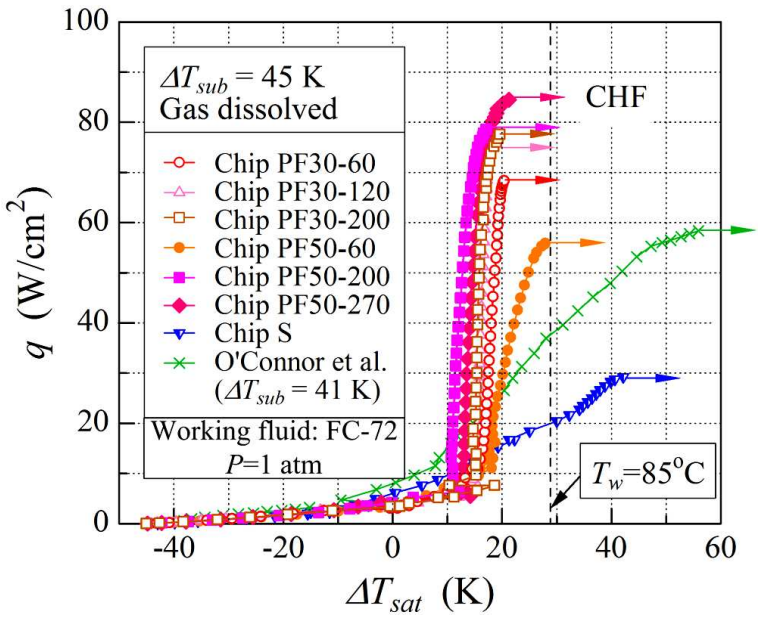

FIG. 1: Comparison of boiling curve between different treated surfaces (Honda and Wei, 2003).

soon extends to the whole surface, which finally leads to the CHF. The capillary force increases with decreasing fin pitch with a penalty that causes the hydraulic resistance of the wet liquid supply to increase. Therefore, there exists an optimum fin pitch for a compromise. A series of experiments conducted to study the size effects of micro-pin-fin have indicated that the fin spacing ranging from 30 to 50 μm and fin height ranging from 60 to 200 μm are preferable alternatives for the design of micro-pin-finned surfaces in the enhancement of nucleate boiling heat transfer. Wei (2002) also compared the pool boiling curves of smooth chip and micro-pin-finned surface at $\Delta T_{\rm sub} = 0$ K. The results indicated that micro-pin-finned surface still showed a sharp increase in q in the nucleate boiling region, but CHF was smaller than that of subcooled boiling. Heat transfer enhancement of micro-pin-finned surface increased with increasing liquid subcooling.

Although pool boiling possesses the attractive attribute of passive fluid circulation without the need of mechanical pumps, less complex and easier sealing, it needs a pool of working fluids and vapor space or submerged condenser, resulting in a large volume occupation. This is not convenient for implementation of the cooling system in a computer. In addition, the capability of pool boiling for removing the heat dissipation from chips is not strong enough. On the other hand, for flow boiling, the flow can be driven by a pump, and the heat can be easily transported to a radiator from the chip, so it is convenient to arrange this cooling system. Mudawar and Maddox (1989), and Rainey et al. (2001) found that flow velocity had a great positive impact on enhancing boiling heat transfer. Therefore, boiling heat transfer from micro-pin-finned chips in a forced flow loop system was also investigated for further enhancements. The experiments performed by Ma et al. (2009), Yuan et al. (2009), and Wei et al. (2009) were to study the combined effects of fluid velocity and subcooling on the flow boiling heat transfer of FC-72 over micro-pin-finned surfaces. Meanwhile, four preferable kinds of micro-pin-finned chips were fabricated. The dimension of the silicon chips was 10 mm × 10 mm × 0.5 mm (length × width × thickness) on which four kinds of micro-pin-fins with the dimensions of 30 × 30 × 60 μm^3, 50 × 50 × 60 μm^3, 30 × 30 × 120 μm^3, 50 × 50 × 120 μm^3 (width × thickness × height, denoted as chips PF30-60, PF50-60, PF30-120, PF50-120) were fabricated with the dry etching technique. The fin pitch is twice the fin thickness. A smooth surface was also tested for comparison. The scanning-electron-micrograph (SEM) images of chips are shown in Figs. 2(a)–2(d). In addition, the details of experimental apparatus and procedure of pool boiling and flow boiling were illustrated in a previous work (Xue et al., 2011).

The comparison of flow boiling curves for all micro-pin-finned surfaces with $\Delta T_{\rm sub} = 35$ K was made by Wei et al. (2009). The results showed that the wall superheat was reduced greatly for all micro-pin-finned surfaces and

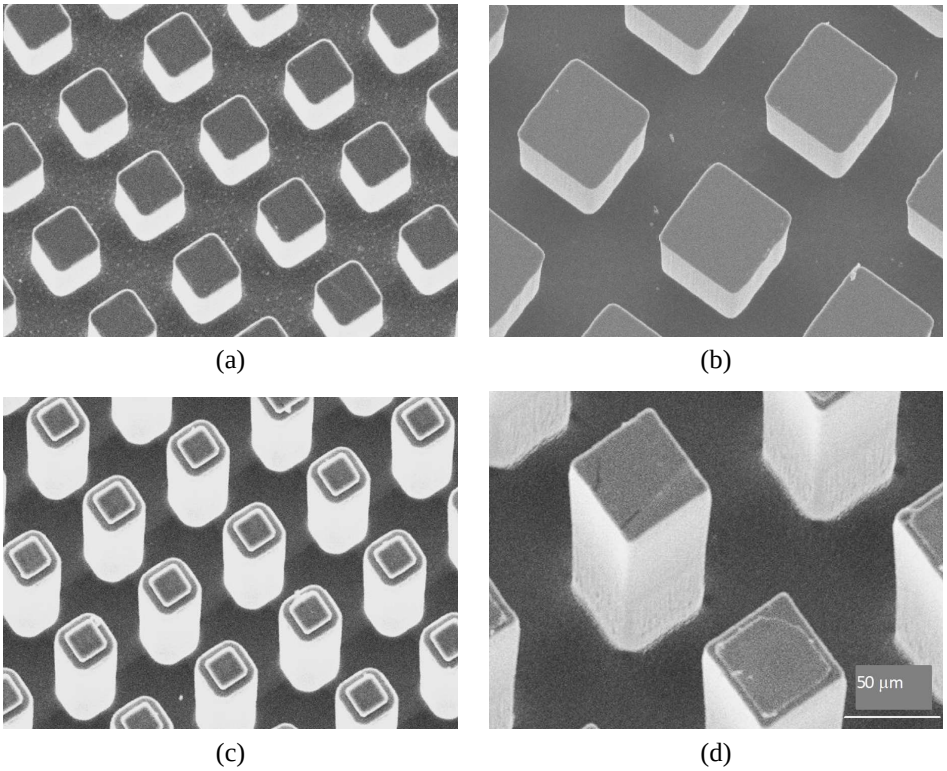

FIG. 2: The SEM images of micro-pin-fins (Guo et al., 2011); (**a**) chip PF30-60, (**b**) chip PF50-60, (**c**) chip PF30-120, (**d**) chip PF50-120.

the values of the CHF increased considerably. Usually, the boiling performance increases with an increase in the total surface area of micro-pin-fins. The high boiling heat transfer performance for the micro-pin-finned surfaces is considered to be relevant to the evaporation of superheated liquid within the confined gaps between fins and micro-convection caused by thermocapillary force due to the suction of a bubble hovering on the top of the micro-pin-fins. The highest value of CHF is 148 W/cm^2, about 1.5 times as large as that for the smooth surface, and it was obtained by chips PF30-120 and PF50-120 at $\Delta T_{\mathrm{sub}} = 35$ K and $V_c = 2$ m/s. Although the flow boiling can make CHF increase greatly by raising flow velocity, the flow velocity is usually limited to below 2 m/s in practical applications. Besides, at a high heat flux, the heater surface is covered by a large amount of vapor which blocks the access of fresh liquid (Yuan et al., 2009) and leads to a boiling crisis. Thus, it is a challenge to further enhance boiling heat transfer by increasing CHF.

Jet impingement, as a local cooling technique, is considered as a very efficient way to enhance heat transfer due to the decrease of boundary layer by high velocity impact. Andrew et al. (2010) found that the critical heat flux (q_{CHF}) increases as jet velocity (V_j) or/and fluid subcooling (ΔT_{sub}) increases. However, this intensification is affected by crossflow. When crossflow velocity (V_c) is large enough, the flow boiling dominates and thus enhances the heat transfer again. Compared with air impingement, some fluids with low boiling point such as FC-40 (Fabbri et al., 2003), FC-72 (Fabbri et al., 2006), liquid nitrogen, water (Ibuki et al., 2009), etc., can achieve much higher q_{CHF} for electronic components. As is mentioned above, flow boiling combined with jet impingement may be a promising way to improve heat transfer performance at high heat flux. On one hand, we can take advantage of the high heat transfer performance of jet flow; on the other hand, it is expected that the jet can penetrate the coalesced bubbles covering the heater surface at high heat fluxes for fresh liquid supply, and thus further improve CHF. The present study aims at further increasing boiling heat transfer enhancement of FC-72 over micro-pin-finned surfaces by using crossflow–jet combined boiling mode.

2. EXPERIMENTAL APPARATUS AND PROCEDURE

The test facility used for the crossflow–jet combined boiling heat transfer is shown schematically in Fig. 3. It is a closed-loop circuit consisting of a tank, a scroll pump, a test section, a jet, two heat exchangers, and two flowmeters. The tank is not full of working fluid FC-72, and there is a valve on the top of the tank to maintain the atmosphere pressure in the system after reaching high subcooling conditions. As shown in Fig. 3, the fluid is pumped from the tank to the heat exchanger. After reaching the required liquid temperature, one branch goes into the test section and the other one impinges on the test chip. Once heat exchange is finished, the fluid goes back to the tank and begins the next circulation. The pump frequency is adjusted to control the mass flow rate and two valves are regulated to realize different crossflows or jet velocities. When the loop reaches a steady state, a direct current is initiated to heat the test chip. A short-lived delay is imposed before data acquisition to ensure steady-state conditions are initiated. The power input to the test chip is increased in small steps up to the high heat flux region of nucleate boiling. The heat flux q is obtained from the voltage drop of the test chip and the electric current. If the wall temperature increases sharply by more than 20 K in a short time, the data acquisition algorithm assumes the occurrence of CHF condition and the power supply is immediately shut down. The CHF value is computed as the steady-state heat flux value just prior to the shutdown of the power supply. The increment of heat flux near CHF is increased in very small steps by controlling the heating voltage. Usually, the absolute error in the CHF is less than 5 W/cm^2.

Schematic diagrams of the test section and heater assembly are shown in Fig. 4. As shown in Fig. 4(a), the test chip is a P-doped N-type square silicon chip with a side length of 10 mm and a thickness of 0.5 mm, which is located 300 mm away from the inlet and is bonded to a substrate made by Pyrex glass. The Pyrex glass is fixed on the bottom of a 5mmhigh and 30mmwide channel. An O-ring is used to prevent liquid leakage. The crossflow velocity is defined as follows:

$$V_c = \frac{M_c}{A}, \tag{1}$$

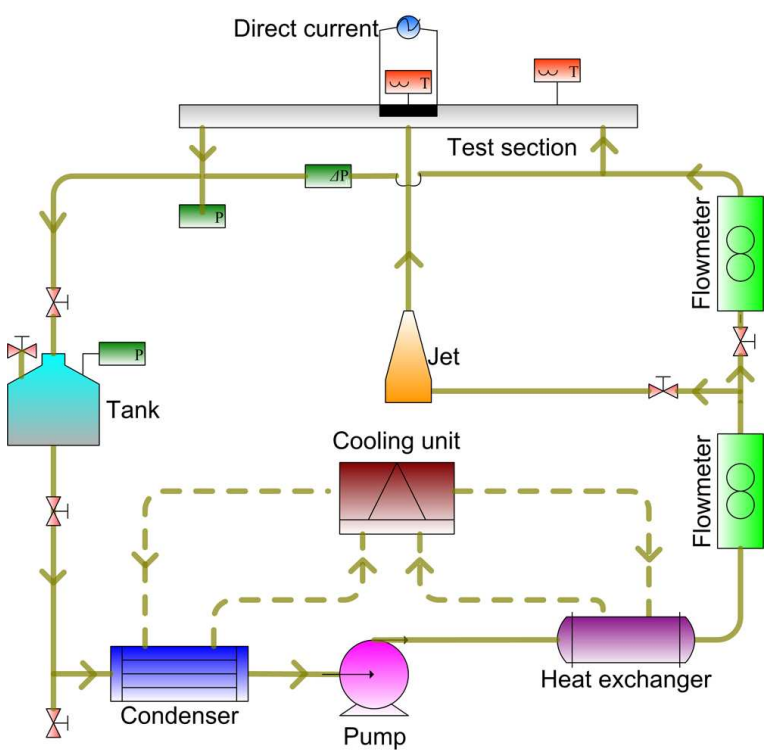

FIG. 3: Boiling heat transfer test loop.

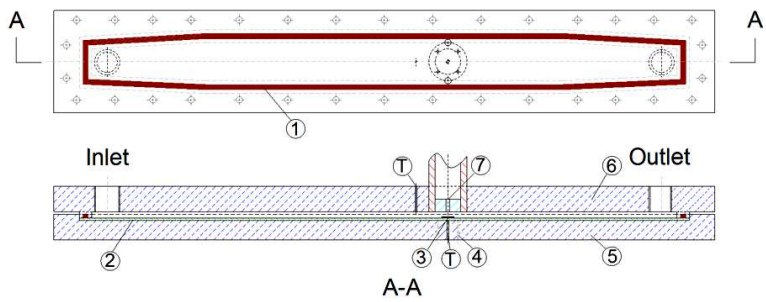

(a)

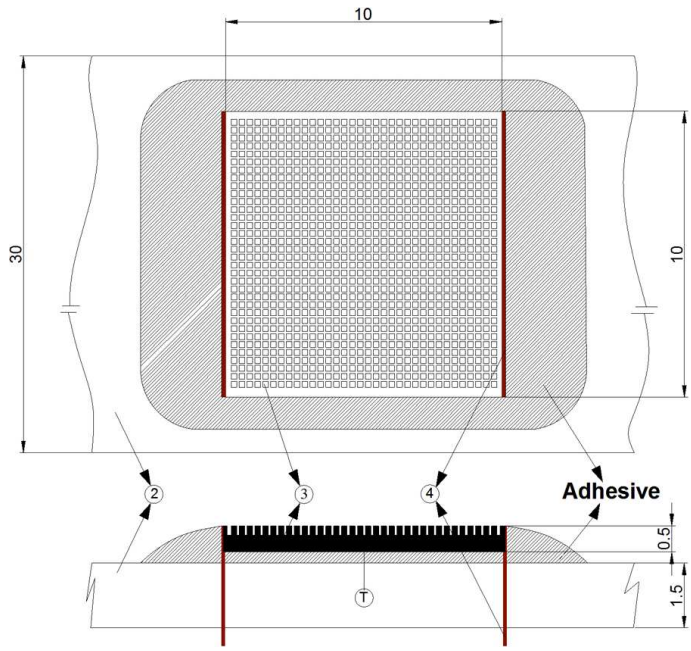

(b)

FIG. 4: Schematic diagrams of test section and heater assembly; (**a**) test section, (**b**) details of heater assembly: (1) O-rings, (2) polycarbonate plate, (3) test chip, (4) copper lead wire, (5) lower cover, (6) upper cover, (7) jet.

where V_c, M_c, and A are crossflow velocity, mass flow rate of crossflow, and cross section area of flow channel (5 mm $\times$ 30 mm), respectively. The flow velocity at the heater assembly is only about 3.4% lower than that at other areas due to the protrusion of the chip. In addition, adiabatic adhesive is used on the side surfaces of the heater to guarantee a smooth transition of fluid flow from flow channel to the heater assembly, as shown in Fig. 4(b). Thus, the effect of the protrusion of the chip on the flow is not great, and can be neglected here. The jet diameter and nozzle–surface distance are 3 and 5 mm, respectively. The jet velocity is defined as follows:

$$V_j = \frac{M_j}{A}, \tag{2}$$

where V_j, M_j, and A are jet velocity, mass flow rate of jet, and area of nozzle, respectively. The side surfaces of the chip are covered by adhesive as shown in Fig. 4(b), and thus only the upper surface is effective for heat transfer. Two copper wires (0.25 mm diameter) are soldered on the opposite side surface of the chip for a power supply. Two T-type thermocouples with a diameter of 0.12 mm for local wall temperature, T_w, and liquid temperature, T_b, are adhered to the bottom surface at the center of the chip and located on a vertical line 25 mm away from the edge of the chip,

respectively. A data acquisition unit is connected to a computer which converts the standard signal (current 4–20 mA) from the flowmeter and thermocouples into flow rate and temperature, respectively. Experiments were conducted at an atmospheric pressure with three different crossflow velocities (0.5 m/s, 1.0 m/s, 1.5 m/s), different jet velocities (0–2 m/s) under two different liquids subcooling (25 and 35 K). The coolant of FC-72 is used as the working fluid with a saturation temperature of 56 K.

Experimental uncertainties are estimated using the method proposed by Kline and McClintock (1953). The uncertainties in the chip and bulk liquid temperature measurements by the thermocouples are less than 0.3 K. Wall temperature uncertainty can be attributed to the errors caused by thermocouple calibration by a platinum resistance thermometer (0.03 K), temperature correction for obtaining surface temperature from the measured value at the bottom of the chip (0.2 K), the temperature unsteadiness (0.1 K), and the thermocouple resolution (less than 0.1 K). The uncertainty of the bulk temperature is due to errors caused by thermocouple calibration by a platinum resistance thermometer (0.03 K), the temperature unsteadiness (0.2 K), and the thermocouple resolution (less than 0.1 K). So the uncertainties in wall superheat, ΔT_b, are 2.1% for the forced convection and 0.85% for the nucleate boiling region. O'Connor and You (1995), O'Connor et al. (1996), and Rainey and You (2000) gained the same heat flux uncertainties as ours with similar construction for their experiments, and the heat losses in their pool boiling are 15.5% and 5.5% for the forced convection and the nucleate boiling region, respectively. In our experiment, heat flux uncertainty includes the error of electric power supplied to the chip (0.11%), which is calculated from the errors of the current (0.014%) and voltage (0.1%) across the chip and heat loss by substrate heat conduction. The heat loss is estimated by solving three-dimensional conduction problems through the substrate using the commercial software FLUENT with the measured wall temperature as a given condition, which is less than 16% and 6% for the forced convection and the nucleate boiling regions, respectively. It should be mentioned that q includes the heat transferred to the bulk liquid by conduction through the polycarbonate substrate. However, the heat flux is very small in the forced convection region, so the absolute error in the forced convection is not strong (usually less than 8 W/cm^2). For the nucleate boiling region, the error absolute is also not large (usually less than 8 W/cm^2) with a small heat loss uncertainty, 6%, although the heat flux is large.

3. RESULTS AND DISCUSSION

3.1 Boiling Curves and Effect of Velocities

Figure 5(a) shows the effect of jet and crossflow velocity on boiling heat transfer on a smooth surface at $\Delta T_{\rm sub} = 35$ K. Both cases show boiling heat transfer enhancement compared with the pool boiling case. For a given crossflow velocity, the boiling heat transfer performance improves with increase in jet velocity. The boiling curve with jet velocity of 2.9 m/s at $\Delta T_{\rm sub} = 21.5$ K (Andrew et al., 2002) showed nearly the same enhanced heat transfer performance as the present chip S at $V_c = 1.5$ m/s, $V_j = 2$ m/s, $\Delta T_{\rm sub} = 35$ K. The open star symbol represents the data obtained by Andrew and co-workers, as shown in Fig. 5.

The ONB (onset of nucleate boiling) points have been marked on the boiling curves by arrows. Minimizing the degree of wall temperature overshoot before ONB is an important issue for electronics cooling. A step change in heat flux is used in our experiment, and a short-lived delay is imposed before initiating data acquisition to ensure steady-state conditions. The duration between the two test points is about 1 min. We have found that the duration of wall temperature overshoot before ONB is quite short, especially in flow boiling and crossflow–jet combined boiling heat transfer. For wall temperature T_w in Fig. 5, it is the mean value of the data during a period of 30 s after heat transfer reached its steady state. Usually, in our pool boiling heat transfer experiment, the degree of wall temperature overshoots before ONB is about 1°C–2°C for micro-pin-finned surfaces. In flow boiling and crossflow–jet combined boiling heat transfer, overshoots are quite small and we could not record them precisely.

Figures 5(b) and 5(c) show the effect of jet and crossflow velocity on boiling heat transfer on chips PF30-60 and PF50-60 at $\Delta T_{\rm sub} = 35$ K, respectively. Both cases suggest boiling heat transfer enhancement compared with the pool boiling case. For a given crossflow velocity, the boiling heat transfer performance improves with increase in jet velocity. It is noticed that for the same largest jet velocity of 2 m/s, small crossflow velocity of 0.5 m/s shows slightly better heat transfer performance than that of 1.5 m/s crossflow velocity at low heat fluxes. However, the latter shows

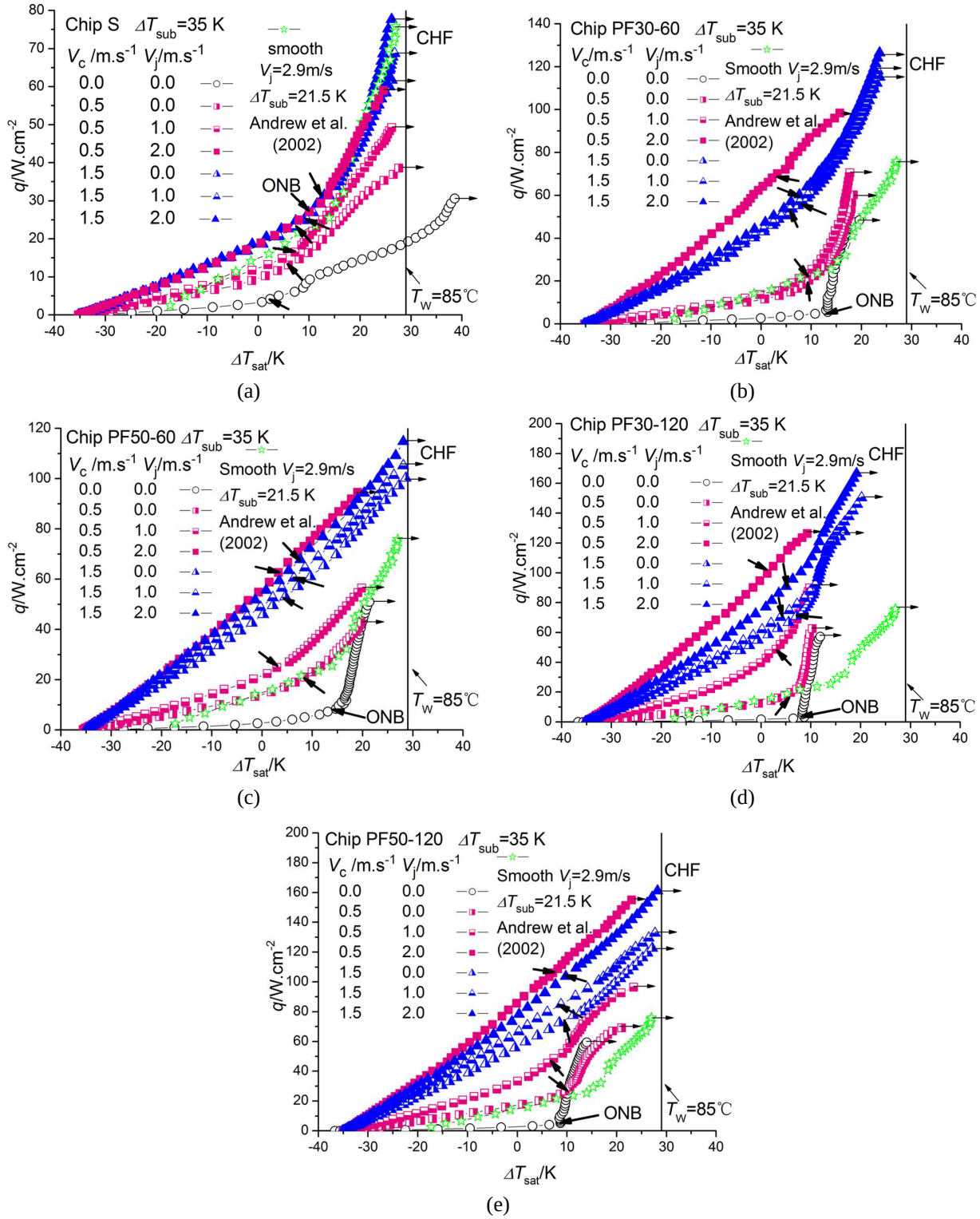

FIG. 5: Boiling curves for various chip surfaces with different velocities at $\Delta T_{\rm sub} = 35$ K; (**a**) chip S, (**b**) chip PF30-60, (**c**) chip PF50-60, (**d**) chip PF30-120, (**e**) chip PF50-120.

a much higher CHF than the former, which means that jet impingement and crossflow impose different effects on heat transfer enhancement for the micro-pin-fins. In the low heat flux region, there are only a few bubbles, and the heat transfer is dominated by the forced convection. Since jet flow usually shows better heat transfer performance than crossflow due to the significant reduction of thermal boundary layer by jet impingement on the heater surface, jet impingement at $V_c = 0.5$ m/s, $V_j = 2$ m/s has a larger heat flux q and smaller wall superheat than that under other conditions for a given surface. For the small crossflow velocity, the jet can penetrate the crossflow and hit on the heater surface directly, while jet flow with large crossflow velocity bends due to the higher crossflow velocity, and thus cannot hit on the heater surface directly to reduce the thermal boundary layer for a great increase in heat transfer. So at low heat fluxes, small crossflow velocity shows better heat transfer performance. However, in the high heat flux region, bubbles tend to be merged and then block the channel. Jet flow with small cross velocity cannot take away the large bubbles due to small total flow rate. Therefore, an early burnout occurs for the case of small crossflow velocity, whereas for large crossflow velocity, jet flow can destroy the bubble layer, and large crossflow velocity can sweep the bubbles in time and further improve the heat transfer in high heat flux. Hence, a large crossflow velocity may provide a better heat transfer performance at high heat fluxes, especially combined with a large jet velocity. Andrew's boiling curve with jet velocity of 2.9 m/s for a smooth surface shows a much lower heat transfer performance than the micro-pin-finned surface, and thus we can see that micro-pin-finned surfaces are very useful for enhancing boiling heat transfer in the jet–crossflow combined boiling mode.

Figures 5(d) and 5(e) show the effect of jet and crossflow velocity on boiling heat transfer over chip PF30-120 and PF50-120 at $\Delta T_{\rm sub} = 35$ K. The two chips exhibit larger surface area enhancement compared with the other two micro-pin-finned chips. The trend of the boiling curves is the same as that of chips PF30-60 and PF50-60, but the heat transfer performance is further enhanced greatly. The maximum CHF can reach more than 160 W/cm^2. Compared with the cases of chips PF30-60 and PF50-60, we can find that the difference between the two boiling curves is very large and obvious. The large difference at low heat fluxes is due to the total surface area difference. But for the large difference at high heat fluxes, it is mainly caused by the aspect ratio of pinfin height to thickness which is 2.0, 1.2, 4.0 and 2.4, for chips PF30-60, PF50-60, PF30-120 and PF50-120, respectively. The micro-pin-fins with small h/t aspect ratio are easily affected by the outer flow condition on the entire side surfaces, and the slopes of the boiling curves are close to those of the convective heat transfer curves, indicating that convective heat transfer dominates the boiling heat transfer process. For large h/t, the outer flow cannot affect the whole side surfaces due to large fin height, so nucleate boiling heat transfer can play an important role on the fin side surfaces at large heat fluxes, resulting in steeper boiling curves. From the present results, it can be obtained that combination of low cross velocity and high jet velocity may be a more effective and economical method duo to reduction of total flow rate, especially at low heat fluxes.

3.2 Effects of Micro-pin-fins

The heat transfer characteristics of micro-pin-fins at $V_c = 0.5$, 1.5 m/s, $V_j = 0$, 2 m/s and $\Delta T_{\rm sub} = 25$ K are shown in Fig. 6 for comparison of the pin-fin size effect. For a given working condition, the micro-pin-finned surfaces perform better heat transfer than the smooth surface, and the heat transfer performance improves in the increasing order of the surface area. This trend of heat transfer enhancement for micro-pin-finned surfaces becomes very clear as the crossflow velocity or jet velocity increases. All micro-pin-finned surfaces have a large heat transfer enhancement compared with the smooth surface due to the increase of surface area, and the surface area enhancement is further increased by changing the fin height. The ratios of micro-pin-finned surface area to smooth surface area are 2.2, 3.0, 3.4 and 5.0 for chips PF50-60, PF30-60, PF50-120 and PF30-120, respectively. For all chips, the maximum $q_{\rm CHF}$ increases in the order of chips S, PF50-60, PF30-60, PF50-120, PF30-120 under crossflow–jet combined boiling heat transfer mode. The increase in the total area is an important reason for enhanced boiling heat transfer over micro-pin-finned surface, but not the only reason. Jet impingement and flow boiling still have different effects on the heat transfer enhancement for the micro-pin-fins. In the low heat flux region, there are only a few bubbles, and the heat transfer is dominated by the forced convection. With increase in velocity, the larger bubbles are taken away by fresh fluid immediately. If the bubble detachment velocity is large enough, a local low pressure condition will be formed in the regular interconnected channels formed by the micro-pin-fins, and thus large velocity may activate more side surfaces of fins and form more nucleation sites. Jet impingement at $V_c = 0.5$ m/s, $V_j = 2$ m/s has a larger heat

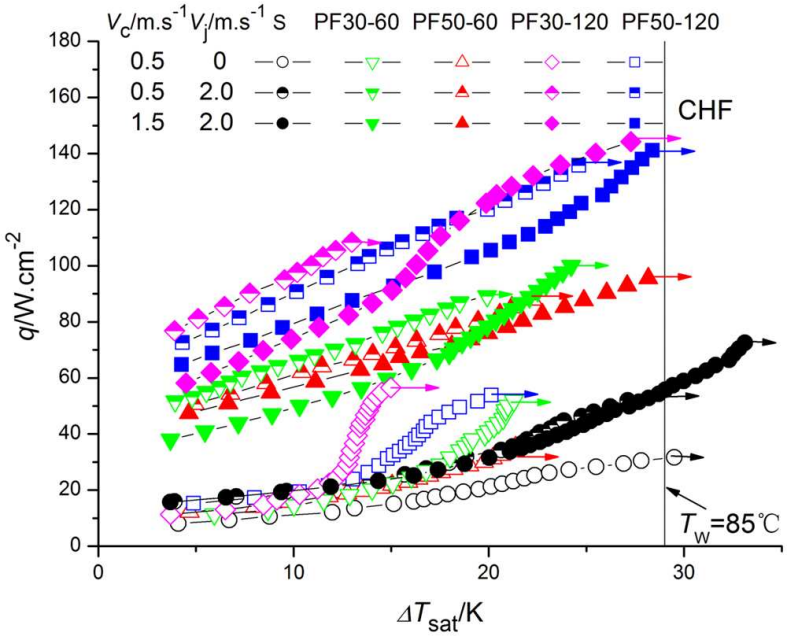

FIG. 6: Effects of micro-pin-fins, $\Delta T_{\rm sub} = 25$ K.

flux q and smaller wall superheat than that under other conditions for a given surface. However, in the high heat flux region, bubbles tend to merge and block the channel. Jet flow can destroy the bubble layer but cannot take it away immediately. Large crossflow velocity can sweep the bubbles in time and further improve the heat transfer in high heat flux. So a large crossflow velocity may provide a better heat transfer performance at high heat fluxes. As for larger liquid subcooling $\Delta T_{\rm sub} = 35$ K, the similar bubble behaviors can be observed, but the boiling curves shift to the left with the temperature of the ONB and the critical wall superheat decreases compared with $\Delta T_{\rm sub} = 25$ K. Besides, the CHF increases with subcooling increase.

3.3 Influence Factors of Maximum Allowable Heat Flux

As is well known, the critical heat flux plays a very important role not only in boiling heat transfer but also in industrial applications. Further study on influence factors of critical heat flux includes subcooling, surface structure and boiling heat transfer mode in the present experiment. In addition, the upper limit of temperature for a reliable operation of electronic chips is given at 85°C. Thus the maximum allowable heat flux $q_{\rm max}$ is given by the $q_{\rm CHF}$ if $T_{w,\rm CHF} < 85$°C and by q at $T_w = 85$°C, if $T_{w,\rm CHF} > 85$°C. Usually, for micro-pin-finned surface at high liquid subcooling $\Delta T_{\rm sub} = 35$ K, $T_{w,\rm CHF}$ is always lower than 85°C, as shown in Fig. 5. With increase in subcooling, the boiling curves shift to the left. However, at low liquid subcooling $\Delta T_{\rm sub} = 25$ K, $T_{w,\rm CHF}$ is related to crossflow velocity and jet velocity, and is more sensitive to crossflow velocity. At large crossflow velocity and jet velocity condition, $T_{w,\rm CHF}$ may be higher than 85°C, such as $V_c = 1.5$ m/s, $V_j = 2$ m/s. This is attributed to the possibility that large velocities may decrease the thickness of the boundary layer and supply the fins' gap with cooled liquid, and then delay the burnout. The detailed results of $\Delta T_{\rm sub} = 25$ K were reported by Guo et al. (2011). Besides, we only choose three types of chips here including chips S, PF30-120 and PF50-120 to research the influence factors of maximum allowable heat flux.

Firstly, to reveal the effect of liquid subcooling on maximum allowable heat flux, the experimental conditions are set to cover two different liquid subcoolings (25, 35 K). In order to show the enhancement for different surfaces of maximum allowable heat flux, a parameter E_1 named enhancement factor is introduced, and it is defined as

$$E_1 = \frac{\Delta q}{q_{\Delta T_{\rm sub}=25{\rm K}}}, \tag{3}$$

where Δq is the difference between maximum allowable heat flux at $\Delta T_{\rm sub} = 25$ K and 35 K, and $q_{\Delta T_{\rm sub}=25{\rm K}}$ is the maximum allowable heat flux for all chips at $\Delta T_{\rm sub} = 25$ K. The values of E_1 for different chips are presented in Table 1. As a result, liquid subcooling has different influences on $q_{\rm max}$ of different sized micro-pin-fins. The values of $\Delta q/q_{\Delta T_{\rm sub}=25{\rm K}}$ of both micro-pin-finned chips and smooth chips are in a range from about 5% to 39%. Arithmetic average of the values of $\Delta q/q_{\Delta T_{\rm sub}=25{\rm K}}$ of chips S, PF30-120 and PF50-120 are 26%, 10% and 13%, respectively. Due to the lower $q_{\rm max}$ of chip S at $\Delta T_{\rm sub} = 25$ K, the values of E_1 are higher than those of micro-pin-finned chips. Besides, Δq of all chips are almost within the same range, which indicates that in our experiment the $q_{\rm max}$ can be increased by at least 10% with liquid subcooling increase by 10°C. The largest increment is 39% for chip S at $V_c = 1.5$ m/s, $V_j = 2.0$ m/s, $\Delta T_{\rm sub} = 35$ K. The bubble departure size becomes smaller and the departure frequency becomes higher for the larger liquid subcooling. The characteristics of small bubbles make the accumulation and mergence more difficult. The fresh liquid can still go into the heater surface and make the convection heat transfer possible, making the nucleate boiling affected by liquid subcooling.

Secondly, after conducting the experiment of crossflow–jet combined boiling heat transfer on micro-pin-finned chips in FC-72, the results of three kinds of boiling heat transfer modes including pool boiling, flow boiling and crossflow–jet combined boiling heat transfer show that the enhancement degrees for different surface structures are different. The maximum allowable heat fluxes of all kinds of chips are shown in Table 2. The effect of surface structure on maximum allowable heat flux is studied, and the results are also presented in Table 2. An enhancement parameter E_2 is defined as follows:

$$E_2 = \frac{q_{\rm max-PF} - q_{\rm max-S}}{q_{\rm max-S}}, \tag{4}$$

where $q_{\rm max-PF}$ is the maximum allowable heat flux of micro-pin-fins, and $q_{\rm max-S}$ is the maximum allowable heat flux of chip S under the same experiment conditions. The results show that the average increment of $q_{\rm max}$ is 137% for both PF30-120 and PF50-120 at $\Delta T_{\rm sub} = 25$ K compared with smooth chips due to an increase in total heat transfer surface area. However, at $\Delta T_{\rm sub} = 35$ K the average increments are 107% and 114%, respectively, which is a little smaller than that at $\Delta T_{\rm sub} = 25$ K. The reason is that increment of heat flux is almost in the same range at different subcoolings, but the $q_{\rm max}$ of chip S at $\Delta T_{\rm sub} = 25$ K is lower than that at $\Delta T_{\rm sub} = 35$ K.

Thirdly, compared with pool boiling heat transfer, flow boiling heat transfer is an enhancement technique, and the enhancement degrees of all chips by flow boiling are shown in Table 3. An enhancement parameter E_3 is defined as follows:

TABLE 1: Heat transfer enhancement factor, E_1 (effect of subcooling)

V_c /**m** · **s**$^{-1}$	V_j /**m** · **s**$^{-1}$	Δq/**W** · **cm**$^{-2}$			E_1/**%**		
		Chip S	**PF50-120**	**PF30-120**	**Chip S**	**PF50-120**	**PF30-120**
0	0	3.9	7.4	5.9	26	14	12
0.5	0	7.3	7.2	5.9	23	12	10
	0.5	8	13.4	5	24	19	7
	1	8.4	14.8	9.1	21	18	11
	2	7	19.2	18	13	14	17
1.0	0	12.3	9.4	5.6	32	11	6
	0.5	10.8	13.1	6.4	26	14	6
	1	12.6	7.8	8.1	29	7	8
	2	13.8	14.4	13.3	26	10	12
1.5	0	10.7	13.2	5.9	21	12	5
	0.5	11.1	12.3	9.3	22	11	7
	1	16.9	12.7	11.7	33	11	8
	2	21.9	20	22.3	39	14	15

TABLE 2: Heat transfer enhancement factor, E_2 (effect of micro-pin-fins)

V_c V_j		$q_{\max}$ /**W · cm**$^{-2}$			E_2/%		$q_{\max}$ /**W · cm**$^{-2}$			E_2/%	
(m · s^{-1}**)**		**S**	**PF50-120**	**PF30-120**	**PF50-120**	**PF30-120**	**S**	**PF50-120**	**PF30-120**	**PF50-120**	**PF30-120**
		$\Delta T_{\rm sub}$ **= 25 K**					$\Delta T_{\rm sub}$ **= 35 K**				
0	0	15.1	52	51.3	244	240	19	59.4	57.2	213	201
0.5	0	31.3	62.1	56.6	98	81	38.6	69.3	62.5	80	62
	0.5	33.7	71.2	69.3	111	106	41.7	84.6	74.3	103	78
	1	40.9	81.6	80.7	100	97	49.3	96.4	89.8	96	82
	2	52	135.8	108.4	161	108	59	155	126.4	163	114
1.0	0	38.3	83.8	92.7	119	142	50.6	93.2	98.3	84	94
	0.5	40.9	94.2	98.8	130	142	51.7	107.3	105.2	108	103
	1	43.3	105	105	142	142	55.9	112.8	113.1	102	102
	2	53.4	137.2	115	157	115	67.2	151.6	128.3	126	91
1.5	0	51	109.3	121.6	114	138	61.7	122.5	127.5	99	107
	0.5	51.4	115	128.1	124	149	62.5	127.3	137.4	104	120
	1	51.8	120	138.6	132	168	68.7	132.7	150.3	93	119
	2	55.7	141	144.3	153	159	77.6	161	166.6	107	115

TABLE 3: Heat transfer enhancement factor, E_3 (effect of crossflow)

V_c V_j		$q_{\max}$ /**W · cm**$^{-2}$			E_3/%			$q_{\max}$ /**W · cm**$^{-2}$			E_3/%		
(m · s^{-1}**)**		**S**	**PF50-120**	**PF30-120**	**S**	**PF50-120**	**PF30-120**	**S**	**PF50-120**	**PF30-120**	**S**	**PF50-120**	**PF30-120**
		$\Delta T_{\rm sub}$ **= 25 K**						$\Delta T_{\rm sub}$ **= 35 K**					
0	0	15.1	52	51.3	0	0	0	19	59.4	57.2	0	0	0
0.5	0	31.3	62.1	56.6	107	19	10	38.6	69.3	62.5	103	17	9
1.0	0	38.3	83.8	92.7	154	61	81	50.6	93.2	98.3	166	57	72
1.5	0	51	109.3	121.6	238	110	137	61.7	122.5	127.5	245	106	123

$$E_3 = \frac{q_{\max-\rm flow} - q_{\max-\rm pool}}{q_{\max-\rm pool}}, \tag{5}$$

where $q_{\max-\rm pool}$ is the maximum allowable heat flux of chips in pool boiling, and $q_{\max-\rm flow}$ is the maximum allowable heat flux of all chips in flow boiling heat transfer under the same experiment conditions. Consequently, E_3 increases linearly as V_c increases. With increase in crossflow velocities, E_3 becomes larger indicating that large crossflow velocity would make much more obvious enhancement compared with pool boiling. The increment percentage of chip S is much larger than that of micro-pin-fins duo to much lower $q_{\max}$ of chip S at $\Delta T_{\rm sub} = 25$ K. The largest increment is 245% for chip S at $V_c = 1.5$ m/s, $\Delta T_{\rm sub} = 35$ K It can be found that in high heat flux region, the heater surface is covered by a large amount of vapor which blocks the access of fresh liquid for pool boiling, whereas the $q_{\max}$ of micro-pin-finned surfaces is still higher than that of the smooth surface. At the critical state, a much larger bubble will cover the whole heater surface. For micro-pin-finned surface, it is considered to be relevant to the evaporation of superheated liquid within the confined gaps between fins and micro-convection caused by capillary force due to the suction of a bubble hovering on the top of the micro-pin-fins. Compared with pool boiling, flow boiling can enhance the heat transfer by increasing velocity. This is attributed to the fact that fluid flow can increase the flow turbulence and decrease the heat transfer resistance and thus increase the heat transfer flux. For smooth surface, the large bubbles can be destroyed when fluid flow velocity increases to a large value. As a result, single-phase forced convective heat transfer dominates the heat transfer process, and thus $q_{\max}$ is much larger than that of pool boiling.

Finally, we turn our attention to the crossflow–jet combined boiling heat transfer which displays a considerable enhancement of maximum allowable heat flux and is presented in Table 4. An enhancement parameter E_4 is defined as follows:

TABLE 4: Heat transfer enhancement factor, E_4 (effect of crossflow–jet combination)

V_c V_j		$q_{\max}$ /W · cm^{-2}			E_4/%			$q_{\max}$ /W · cm^{-2}			E_4/%		
(m · s^{-1})		S	PF50-120	PF30-120	S	PF50-120	PF30-120	S	PF50-120	PF30-120	S	PF50-120	PF30-120
		$\Delta T_{\rm sub}$ = 25 K						$\Delta T_{\rm sub}$ = 35 K					
0	0	15.1	52	51.3	0	0	0	19	59.4	57.2	0	0	0
0.5	0.5	33.7	71.2	69.3	123	37	35	41.7	84.6	74.3	119	42	30
	1	40.9	81.6	80.7	171	57	57	49.3	96.4	89.8	159	62	57
	2	52	135.8	108.4	244	161	111	59	155	126.4	211	161	121
1.0	0.5	40.9	94.2	98.8	171	81	93	51.7	107.3	105.2	172	81	84
	1	43.3	105	105	187	102	105	55.9	112.8	113.1	194	90	98
	2	53.4	137.2	115	254	164	124	67.2	151.6	128.3	254	155	124
1.5	0.5	51.4	115	128.1	240	121	150	62.5	127.3	137.4	229	114	140
	1	51.8	120	138.6	243	131	170	68.7	132.7	150.3	262	123	163
	2	55.7	141	144.3	269	171	181	77.6	161	166.6	308	171	191

$$E_4 = \frac{q_{\max-\text{crossflow-jet}} - q_{\max-\text{pool}}}{q_{\max-\text{pool}}}, \tag{6}$$

where $q_{\max-\text{pool}}$ is the maximum allowable heat flux of chips in pool boiling, and $q_{\max-\text{crossflow-jet}}$ is the maximum allowable heat flux of all chips in crossflow–jet combined boiling heat transfer under the same experiment conditions. There is, however, an obvious enhancement of $q_{\max}$ for crossflow–jet combined boiling. The $q_{\max}$ of both smooth surface and micro-pin-finned surface increases as V_c or V_j increases. The data given in Table 4 also manifest that the largest increment is 308% for chip S at $V_c = 1.5$ m/s, $V_j = 2.0$ m/s, $\Delta T_{\rm sub} = 35$ K. We have observed that the maximum allowable heat fluxes are 77.6 W/cm^2, 167 W/cm^2 and 161 W/cm^2 for chips S, PF30-120 and PF50-120 at $V_c = 1.5$ m/s, $V_c = 2.0$ m/s, $\Delta T_{\rm sub} = 35$ K, respectively. The $q_{\max}$ of chip S is 15.1 W/cm^2 at $\Delta T_{\rm sub} = 25$ K by pool boiling, and the $q_{\max}$ of micro-pin-fins by crossflow–jet combined boiling in the experiment is 167 W/cm^2, which is 11.06 times as large as that for the smooth surface. It is defined that the enhancement parameter E_5 indicates the enhancement degree of $q_{\max}$ after a combination of influence factors is made

$$E_5 = \frac{q_{\max-\Delta T_{\rm sub}=35\text{K}-\text{crossflow-jet}} - q_{\max-\Delta T_{\rm sub}=25\text{K}-\text{S-pool}}}{q_{\max-\Delta T_{\rm sub}=25\text{K}-\text{S-pool}}}, \tag{7}$$

where $q_{\max-\Delta T_{\rm sub}=35\text{K}-\text{PF-crossflow-jet}}$ is the maximum allowable heat flux of micro-pin-finned chips in crossflow–jet combined boiling at $\Delta T_{\rm sub} = 35$ K, and $q_{\max-\Delta T_{\rm sub}=25\text{K}-\text{S-pool}}$ is the maximum allowable heat flux of chip S in pool boiling heat transfer at $\Delta T_{\rm sub} = 25$ K. Figure 7 presents the enhancement parameter of $q_{\max}$ with different influence factors compared with chip S by pool boiling at $\Delta T_{\rm sub} = 25$ K. The enhancement degree increases in the order of liquid subcooling, surface structure, flow boiling and crossflow–jet combined boiling, whereas enhancement parameter E_5 is higher than the sum of values of E_1, E_2, E_3, and E_4. Thus, influence factors have synergistic effects with a complicated positive interaction with each other, and the mechanism is to be studied in future studies.

4. CONCLUSIONS

The enhancement in flow boiling heat transfer with jet impingement of FC-72 on micro-pin-finned surface was studied. A smooth surface was tested for comparison. The enhanced pool boiling and flow boiling heat transfer over micro-pin-finned surfaces were also researched in our previous study. After in-depth analysis of three modes of boiling heat transfer, some conclusions have been drawn as follows:

– Firstly, all chips in crossflow–jet combined boiling mode almost show a better heat transfer performance than pool boiling or boiling in crossflow heat transfer. Besides, all micro-pin-fins show an obvious heat transfer enhancement compared with smooth surface under all three boiling heat transfer modes, which is related to the surface area increase.

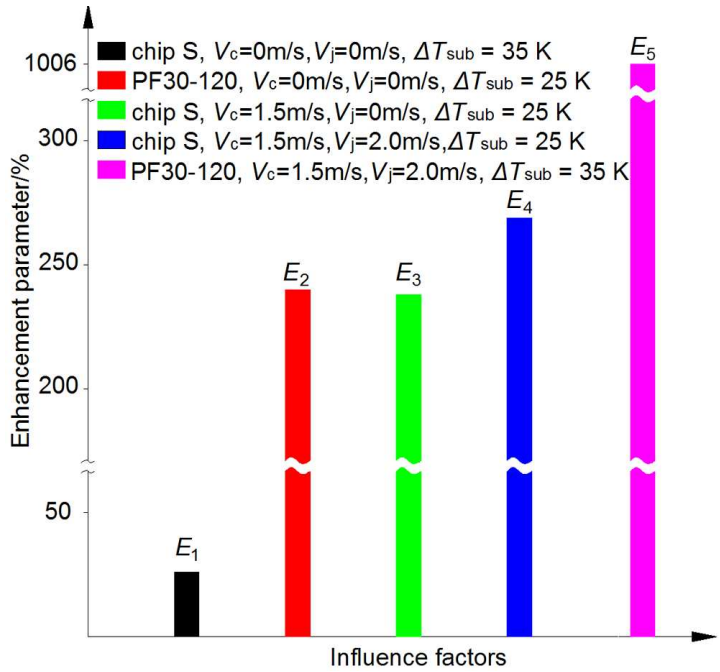

FIG. 7: Enhancement parameter values of $q_{\max}$ compared with chip S in pool boiling at $\Delta T_{\text{sub}} = 25$ K.

– Secondly, the maximum q_{CHF} increases in the order of pool boiling, flow boiling, and crossflow–jet combined boiling heat transfer. For all chips, the maximum q_{CHF} increases in the order of chips S, PF50-60, PF30-60, PF50-120, PF30-120 under all three boiling heat transfer modes, and q_{CHF} increases with crossflow or jet velocities. For crossflow–jet combined boiling heat transfer, crossflow is better for increasing CHF, while a combination of low cross velocity and high jet velocity is more effective and economical at low heat fluxes.

– Finally, influence factors of maximum allowable heat flux include subcooling, surface structure and boiling modes in the present experiment, the combination of which has a synergistic effect to enhance maximum allowable heat flux greatly. The upper limit of temperature for a reliable operation of electronic chips is given at 85°C. Thus the maximum allowable heat flux $q_{\max}$ is given by the q_{CHF} if $T_{w,\text{CHF}} < 85$°C and by q at $T_w = 85$°C, if $T_{w,\text{CHF}} > 85$°C The largest maximum allowable heat flux of micro-pin-fins by crossflow–jet combined boiling is 167 W/cm^2 for PF30-120 at $V_c = 1.5$ m/s, $V_j = 2.0$ m/s, $\Delta T_{\text{sub}} = 35$ K, which is 11.06 times as large as that for the smooth surface in pool boiling at $\Delta T_{\text{sub}} = 25$ K.

ACKNOWLEDGMENT

This work is supported by the project of National Natural Science Foundation of China (grants no. 51225601 and no. 51121092).

REFERENCES

Andrew, C. C., David, R. H. G., and Peter, T. I., Enhancement of impingement cooling in a high cross flow channel using shaped impingement cooling holes, *ASME J. Turbomachinery*, vol. **132**, pp. 1–8, 2010.

Andrew, A. T., Hong, X., and Cheng, Y., Cooling of electronics components with free jet impingement boiling, In *Proc. of Eighth Intersociety Conference on Thermal Phenomena*, vol. **6**, pp. 387–394, 2002.

Anderson, T. M. and Mudawar, I., Microelectronic cooling by enhanced pool boiling of a dielectric fluorocarbon liquid, *ASME J. Heat Transfer*, vol. **111**, pp. 752–759, 1989.

Fabbri, M., Jiang, S., and Dhir, V. K., Experimental investigation of single-phase micro-jets impingement cooling for electronic applications, In *Proc. of 2003 ASME Summer Heat Transfer Conference*, LasVegas, NV, pp. 461–468, 2003.

Fabbri, M., Wetter, A., Mayer, B., Brunschwiler, T., Michel, B., Rothuizen, H., Linderman, R., and Kloter, U., Microchip cooling module based on FC-72 slot jet arrays without cross-flow, In *Proc. of Twenty-Second Annual IEEE Semiconductor Thermal Measurement and Measurement Symposium*, Dallas, TX, pp. 54–58, 2006.

Guo, D., Wei, J. J., and Zhang, Y. H., Enhanced flow boiling heat transfer with jet impingement on micro-pin-finned surfaces, *Appl. Therm. Eng.*, vol. **31**, nos. 11–12, pp. 2044–2053, 2011.

Hwang, U. P. and Moran, K. F., Boiling heat transfer of silicon integrated circuits chip mounted on a substrate, *ASME HTD*, vol. **20**, pp. 53–59, 1981.

Honda, H., Takamastu, H., and Wei, J. J., Enhanced boiling of FC-72 on silicon chips with micro-pin-fins and submicron-scale roughness, *J. Heat Transfer*, vol. **124**, pp. 383–390, 2002.

Honda, H. and Wei, J. J., Advances in enhanced boiling heat transfer from electronic components, In *Proc. of The 6th ASME-JSME Thermal Engineering Joint Conference*, March 16–20, 2003.

Honda, H. and Wei, J. J., Enhanced boiling heat transfer from electronic components by use of surface microstructures, *Exp Therm Fluid Sci*, vol. **28**, pp. 159–169, 2004.

Ibuki, K., Umeda, T., Fujimoto, H., and Takuda, H., Heat transfer characteristics of a planar water jet impinging normally or obliquely on a flat surface at relatively low Reynolds numbers, *Exp Therm Fluid Sci.*, vol. **33**, pp. 1226–1234, 2009.

Kline, S. J. and McClintock, F. A., Describing uncertainties in single-sample experiments, *Mech Eng*, vol. **75**, pp. 3–8, 1953.

Kubo, H., Takamatsu, H., and Honda, H., Effects of size and number density of micro-reentrant cavities on boiling heat transfer from a silicon chip immersed in degassed and gas dissolved FC-72, *J. Enhanced Heat Transfer*, vol. **6**, pp. 151–160, 1999.

Mudawar, I. and Maddox, D. E., Critical heat flux in subcooled flow boiling of fluorocarbon liquid on a simulated electronic chip in a vertical rectangular channel, *Int. J. Heat and Mass Transfer*, vol. **32**, pp. 379–394, 1989.

Ma, A. X., Wei, J. J., Yuan, M. Z., and Fang, J. B., Enhanced flow boiling heat transfer of FC-72 on micro-pin-finned surfaces, *Int. J. Heat Mass Transfer*, vol. **52**, pp. 2925–2931, 2009.

Nelson, L. A., Sekhon, K. S., and Fritz, J. E., Direct heat pipe cooling of semiconductor devices, In *Proc of the 3rd International Heat Pipe Conference*, Palo Alto, CA, pp. 373–376, 1978.

Oktay, S. and Schmeckenbecher, A., *A method for forming heat sinks on semiconductor device chips*, US Patent no. 3706127, 1972.

O'Connor, J. P., You, S. M., and Price, D. C., A dielectric surface coating technique to enhance boiling heat transfer from high power microelectronics, *IEEE Trans. Compon., Packag., Manuf. Technol.*, vol. **18**, pp. 656–663, 1995.

O'Connor, J. P. and You, S. M., A painting technique to enhance pool boiling heat transfer in FC-72, *ASME J. Heat Transfer*, vol. **117**, no. 2, pp. 387–393, 1995.

O'Connor, J. P., You, S. M. and Chang, J. Y., Gas saturated pool boiling heat transfer from smooth and microporous surfaces in FC-72, *ASME J. Heat Transfer*, vol. **118**, pp. 662–667, 1996.

Phadke, N. K., Bhavnani, S. H., Goyal, A., Jaeger, R. C., and Goodling, J. S., Re-entrant cavity surface enhancements for immersion cooling of silicon multichip packages, *IEEE Trans. Compon., Hybrids, Manuf. Technol.*, vol. **15**, pp. 815–822, 1992.

Rainey, K. N., Li, G., and You, S. M., Flow boiling heat transfer from plain and microporous coated surfaces in subcooled FC-72, *ASME J. Heat Transfer*, vol. **123**, pp. 918–925, 2001.

Rainey, K. N. and You, S. M., Pool boiling heat transfer from plain and micro-porous, square pin-finned surfaces in saturated FC-72, *ASME J. Heat Transfer*, vol. **122**, no. 3, pp. 509–516, 2000.

Rainey, K. N., You, S. M., and Lee, S., Effect of pressure, subcooling, and dissolved gas on pool boiling heat transfer from microporous, square pin-finned surfaces in FC-72, *Int. J. Heat Mass Transfer*, vol. **46**, pp. 23–25, 2003.

Ujereh, S., Fisher, T., and Mudawar, I., Effects of carbon nanotube arrays on nucleate pool boiling, *Int. J. Heat Mass Transfer*, vol. **50**, pp. 4023–4038, 2007.

Wei, J. J., *Experimental study on enhanced boiling heat transfer from silicon chips with micro-pin-fins and submicro-scale roughness* PhD Thesis, Kyushu University, 2002.

Wei, J. J., Guo, L. J., and Honda, H., Experimental study of boiling phenomena and heat transfer performances of FC-72 over micro-pin-finned silicon chips, *Heat Mass Transfer*, vol. **41**, pp. 744–755, 2005.

Wei, J. J. and Honda, H., Effects of fin geometry on boiling heat transfer from silicon chips with micro- pin-fins immersed in FC-72, *Int. J. Heat Mass Transfer*, vol. **46**, pp. 4059–4070, 2003.

Wei, J. J., Zhao, J. F., Yuan, M. Z., and Xue, Y. F., Boiling heat transfer enhancement by using micro-pin-finned surface for electronics cooling, *Microgravity Sci Technol*, vol. **21**, pp. 159–173, 2009.

Xue, Y. F., Yuan, M. Z., Ma, A. X., and Wei, J. J., Enhanced boiling heat transfer by using micro-pin-finned surface in three different test systems, *Heat Transfer Eng*, vol. **32**, nos. 11–12, pp. 1062–1068, 2011.

Yuan, M. Z., Wei J. J., Xue, Y. F., and Fang, J. B., Subcooled flow boiling heat transfer of FC-72 from silicon chips fabricated with micro-pin-fins, *Int. J. Therm Sci*, vol. **48**, pp. 1416–1422, 2009.

Interfacial Phenomena and Heat Transfer, 1 (1): 29–49 (2013)

DETERMINATION OF APPARENT CONTACT ANGLE AND SHAPE OF A STATIC PENDANT DROP ON A PHYSICALLY TEXTURED INCLINED SURFACE

Gaurav Bhutani, K. Muralidhar, & Sameer Khandekar*

Department of Mechanical Engineering, Indian Institute of Technology Kanpur, Kanpur 208016, India

*Address all correspondence to Sameer Khandekar, E-mail: samkhan@iitk.ac.in

Estimating the apparent contact angle under equilibrium conditions is critical for the understanding of several engineering processes. Some examples are dropwise condensation, digital microfluidics, and material deposition schemes. Often, there is considerable uncertainty in the experimental estimation of the contact angle. In this work, we discuss the contact angles and shapes of pendant drops on physically textured inclined surfaces. Two methodologies to determine the apparent contact angles have been employed. In one approach these are obtained from drawing tangents at contact points of micro-droplets in optical images using digital image processing. In the second method, the three-dimensional (3D) Young–Laplace equation is numerically solved using the open-source software, Surface Evolver, by minimizing the sum of the potential and surface energies of the pendant droplet. A section of the numerically obtained 3D droplet shape is then fitted to the experimentally obtained two-dimensional profile using an inverse method. Advancing and receding angles of the imaged drop are calculated by minimizing the error between the numerical and experimental drop shapes, providing good estimates of these angles. In addition, the complete 3D droplet shape is also obtained. The overall methodology presented herein is generic, although the experiments have been conducted with glycerin as the working fluid. The role of surface roughness, plate inclination, and drop volume on the advancing and receding angles of a pendant drop are discussed. On inclined surfaces, the three-phase contact line does not remain pinned and its shape is not circular. The receding angle progressively diminishes with inclination while the advancing angle remains nearly constant.

KEY WORDS: *pendant drop, apparent contact angle, drop profile, advancing and receding angles, Surface Evolver, inverse technique, surface roughness, surface inclination*

1. INTRODUCTION

Surface energy–induced drop movement in microfluidic systems is of importance in microscale thermophysical devices, biological microelectromechanical systems (bio-MEMS), and lab-on-chip applications. Texturing and patterning are physical methods of altering contact angles locally and can be utilized in the design of surface energy gradients. Physical texturing is preferred over chemical techniques because chemical coatings tend to wear off by viscous stresses. In the search for better surfaces, data on contact angles of pendant drops and their sensitivity to substrate inclination and texture are often required. The present study is concerned with developing a formal approach that extracts contact angles from photographic images of drops. Knowledge of the apparent contact angle (referred to as the contact angle in subsequent discussions) and the shape of a pendant drop formed on a substrate are also important in understanding processes such as dropwise condensation, drug delivery, microscale thermophysical engineering, and adhesive technology, to name a few. Equilibrium contact angles, in turn, carry information on surface properties, including wettability and surface energy. An important application requiring detailed knowledge of contact angles as well as the three-dimensional (3D) shapes is the process of vapor condensation as a collection of drops (Sikarwar et al., 2011), particularly of low-conductivity liquids. Dropwise condensation is preferred over the filmwise mode owing to its high heat transfer coefficient and control of the condensation rate, particularly on inclined surfaces (Carey, 1992).

2169–2785/13/$35.00 © 2013 by Begell House, Inc.

NOMENCLATURE

B	ratio of excess pressure inside the drop to surface tension at liquid-gas interface (m^{-1})
Bo	Bond number ($= \rho g D^2 \sin\alpha/\gamma$)
D	base diameter of a horizontal drop (m)
D'	base diameter of a drop on an inclined plate (m)
d	maximum drop height in the z direction (m)
g	acceleration due to gravity (m/s^2)
R	radial distance measured from the center of a drop cap (m)
r	root-mean-square roughness of a surface (m)
r'	Wenzel's roughness parameter (= actual surface area/projected surface area)
V_D	volume of the drop (m^3)
z	vertical coordinate taken as positive in the downward direction

Greek Symbols

α	substrate inclination angle (°)
β	polar angle (°)
γ	surface tension (N/m)
Δp	excess pressure inside the drop (Pa)
ζ	coordinate along the symmetry axis in an axisymmetric drop
θ	contact angle (°)
θ_{adv}	advancing angle (°)
θ_E	Young's contact angle (°)
θ_{rec}	receding angle (°)
θ_{min}	minimum contact angle of a three-dimensional drop (°)
θ_{max}	maximum contact angle of a three-dimensional drop (°)
θ_o	horizontal drop contact angle (°)
θ^*	Wenzel's contact angle (°)
κ_m	mean curvature of the liquid–air interface (m^{-1})
μ	liquid viscosity (Pa-s)
ρ_f	density of the liquid (kg/m^3)
σ	axis perpendicular to the symmetry axis in an axisymmetric drop
ϕ	azimuthal angle measured along the three-phase contact line (°)
ψ	angle made by the tangent on the surface of an axisymmetric drop (°)

Here, knowledge of the three-phase contact angle distribution going around the circumference of the condensed liquid droplet is essential to accurately determine the transport rates. Contact angles also govern the interaction of interfacial and body forces acting on sessile and pendant drops. The molecular forces at the three-phase contact line manifest at the macroscopic level as the contact angle and affect steady as well as unsteady transport phenomena.

The physicochemical interaction of liquids on solid surfaces is an active subject of research and has been extensively pursued (Fox and Zisman, 1950; Tuteja et al., 2008; Ajaev et al., 2010; Style and Dyfresne, 2012). Contact angles of various solid–liquid combinations have been reported in the literature. Much of these data are applicable to sessile drops owing to the ease of experimentation. In contrast, pendant drops are difficult to deal with in experiments, especially when the droplet volumes are of the order of microliters. In addition, when the surface on which the pendant drop is deposited is inclined with respect to the horizontal, the advancing angle will be greater than the receding angle. These angles are a function of plate inclination. Overall, the drop is deformed and becomes non-axisymmetric. Although there is an abundance of data on contact angles, there exists a clear gap in the knowledge of contact angles of pendant drops on inclined surfaces. Brown et al. (1980), El Sherbini and Jacobi (2004), and Annapragada et al. (2012) have discussed the effect of plate inclination on the advancing and receding angles of sessile drops. Receding contact angles of sliding drops have also been discussed by Winkels et al. (2011). Cheng et al. (1990) performed experiments on pendant axisymmetric glycerin and water drops to measure the contact angles. On inclined surfaces, the advancing contact angle is different from the receding contact angle and the difference is termed the contact angle hysteresis (CAH).

Factors such as the physical morphology, surface roughness, chemical texture, presence of impurities, nonhomogeneity, anisotropic surface characteristics, substrate inclination, and presence of external body and surface forces affect the equilibrium contact angles of liquid droplets on solid surfaces. Temperature is an important parameter because thermophysical properties depend on it.

One method of altering the wettability of a substrate is to treat it chemically by grafting or adsorbing special promoter molecules with wetting characteristics of their own. This effect of chemical texturing has been previously studied (Wolfram and Faust, 1978; Lee, 1999; Berthier, 2008; Bhushan and Jung, 2011). Chemically textured surfaces have been synthesized to control surface energy gradients and obtain very large contact angles and low CAH (Bico et al., 1999). Such super-hydrophobic surfaces have a contact angle greater than 150° and CAH less than 10°. Furthermore, substrates with designed surface energy gradients can also be formed, which are useful in controlling the flow of drops at low or no plate inclination, and this is an area of extensive research (Chaudhury and Whitesides, 1992; Shastry et al., 2006). In applications where the liquid forming the droplets is highly corrosive—for example, in metal vapor condensation processes—the chemically textured surface usually has a short lifespan. The promoter layer gets leeched away by the condensing liquid droplets, thereby deteriorating the substrate and altering the contact angle. This shortcoming has created a need to alter the surface properties by introducing roughness or through alteration of the physical morphology of the substrate, which can be specifically micro- or nano-patterned or statistically rough (Barthlott and Neinhuis, 1997; Quéré, 2002; Abdelsalam et al., 2005; Bhushan and Jung, 2011). The lotus leaf is a naturally rough surface with a hierarchical physical morphology and has been characterized by many authors, including Barthlott and Neinhuis (1997), Bico et al. (1999), and Bhushan and Jung (2011). Depending on the morphology and the resulting surface energy distribution, a droplet can sit on a solid surface in two distinct configurations. It is said to be in a Wenzel state when it is conformal with the topography, and Wenzel's equation can be used to compute the contact angle (Wenzel, 1936; Berthier, 2008). The other is the Fakir state (Cassie and Baxter, 1944) where the drop only touches the peaks of the physical protrusions present on the surface.

Besides measuring the contact angle at the base of a drop, it is also important to obtain the shape of the three-phase contact line; i.e., the footprint of the drop on the substrate. The contact line is actually in quasi-static equilibrium and its shape changes with the plate inclination (Berejnov and Thorne, 2007). In earlier studies, Wolfram and Faust (1978) and Brown et al. (1980) assumed the contact line was circular for a static drop and pinned everywhere for horizontal and inclined plate configurations. Extrand and Kumagai (1995) measured the aspect ratios of the base contours in water and ethylene glycol drops on polymers. Kalinin et al. (2008) forced the contact line of sessile drops to remain pinned with the inclination by placing them inside photolithographic micro-patterned rings. El Sherbini and Jacobi (2004) showed that the three-phase contact line for a static drop does change with the plate inclination and they fitted the base contour by two ellipses sharing the minor axis. Much of the work reported on the contact line shape involves sessile drops. The present study examines the contact lines of pendant drops on horizontal and inclined surfaces.

Analytical and numerical techniques have been used to predict the drop shapes in two and three dimensions. Brown et al. (1980) used the finite-element method (FEM) to determine the 3D shapes of static drops on inclined plates with an assumption of a circular wetted area. Rio and Neumann (1997) fitted numerical shapes to experimental drop profiles to compute the contact angles and interfacial tensions. The Young–Laplace equation was solved for axisymmetric sessile and pendant drops and the entire drop shape fitted to the experimental measurement. Dingle et al. (2005) used a similar fitting technique to determine the interfacial tension values of axisymmetric drops. Iliev (1995) and Liao et al. (2009) used an iterative method to minimize the overall energy of the system to predict the shapes of sessile drops on horizontal and inclined surfaces. Adamiak (2006) obtained the axisymmetric shape of a conducting liquid drop placed on a hydrophobic dielectric surface with an external electric field. A finite-difference method was used to simultaneously solve the Poisson equation for the electric field and the Young–Laplace equation for the drop shape. The wettability of the system was increased by applying an electric potential difference between the droplet and the counter-electrode. The contact angle was seen to follow the Lippman–Young equation (Mugele and Barrett, 2005; Adamiak, 2006; Berthier, 2008). Pozrikidis (2009) developed a parametric route to numerically solve the Young–Laplace equation and obtained the shapes of axisymmetric sessile and pendant drops. This method has been used to validate the simulations of the present study of a horizontal surface. Santos and White (2011) used the open-source software, *Surface Evolver* (http://www.susqu.edu/brakke/evolver/evolver.html), to simulate the shapes of non-axisymmetric sessile drops. Annapragada et al. (2012) developed a volume-of-fluid (VOF) continuous-surface-force (CSF) model to predict the shapes of sessile droplets under gravity for various substrate inclinations.

In the present study, pendant drops have been imaged for various plate inclinations, substrate roughness, and drop volumes to obtain their equilibrium advancing and receding angles. Glycerin was chosen as the working fluid due to its low vapor pressure and high viscosity. Aluminum and copper surfaces of varying average roughness have been

used as the substrate materials. The apparent contact angles have been estimated using two methods. In Method 1, digital image processing of experimentally obtained images by the tangent method was used. In Method 2, an inverse method was employed that numerically solves the Young–Laplace equation using a variational approach with *Surface Evolver*. Method 2 also yields 3D drop shapes on inclined surfaces. In Method 2, the 3D shape determined numerically is selectively fitted to the experimental drop shape to obtain the contact angles. This approach is similar to that of Rio and Neumann (1997), except that the advancing and receding angles of non-axisymmetric pendant drops obtained by an inverse technique as well as their base shapes are reported in the present study.

2. EXPERIMENTAL APPARATUS AND PROCEDURE

The randomly distributed isotropic roughness of a surface is characterized by its root-mean-square (RMS) value. Three such surfaces with RMS roughness values of around 0.5, 1.5, and 4.0 μm were obtained on aluminum and copper substrates by the wet lapping process. A contact angle measurement goniometric apparatus, developed as part of this work, was used to image the pendant drops on these inclined, randomly textured surfaces. The apparatus [see Fig. 1(a)] can precisely tilt the substrate plate in steps of 1° image the pendant drop from a direction normal to the vertical plane of the tilt; namely, the plane of symmetry of the drop over a range of inclinations (0–45°). Microliter syringes (100 ± 2 and 50 ± 1 μL) were used to deposit liquid pendant drops on the underside of the substrates, with sizes ranging from 5 to 30 μL. The working fluid was glycerin; with density ρ = 1260 kg/m^3, surface tension γ = 63.4 mN/m, and dynamic viscosity μ = 1.069 Pa-s. Glycerin has low volatility and high viscosity, which helps the drop stabilize in a short time period. In addition, results are presented in terms of the Bond number, which enables generalization of the measured data for other liquids. During the experiments, the room temperature was maintained at 20 ± 1°C. A high-resolution progressive scan charge-coupled device camera (Basler A202k: pixel resolution: 1024 × 1024), fitted with a macro-lens, was used to image drops without any wide-angle distortion, with each pixel representing about 6 μm. A dual-channel frame grabber card was used to grab frames from the camera to be stored in a computer hard drive. Post-processing of the droplet images was performed by programs written in *WiT Platform* (Teledyne-Dalsa). *MATLAB* programs extracted the contact angles and drop profiles from the raw images. A pixel-wise scanning algorithm extracted the overall drop profile. The corner pixel was joined to a neighboring pixel to form a tangent. The contact angles have been reported for the eighth neighbor in this study. The angle between this tangent and the horizontal form the basis of the tangent method. To overcome subjectivity in the tangent measurement, an improved inverse technique has been used and is discussed in Sec. 3.2. The drop volume, surface inclination, substrate roughness, and substrate material are the four parameters that were varied in the experiments. Figure 1(b) shows a collection of pendant drop images of a 30 μL glycerin drop on an aluminum surface of 1.46 μm roughness. Changes in the drop shape and contact angles with increasing plate inclination can be clearly seen in Fig. 1(b).

3. NUMERICAL DETERMINATION OF DROPLET SHAPES

The shape of a static drop supported on a solid surface is governed by the Young–Laplace equation, which balances the weight, surface tension, and internal pressure. For two-dimensional (2D) drops, the Young–Laplace equation can be solved using the approach suggested by Pozrikidis (2009). The Young–Laplace equation for 3D axisymmetric drops can be represented using two coordinates, and the solution methodology is presented in Appendix 1. In three dimensions, the equation is rather difficult to solve for non-symmetric cases and alternative approaches are preferred (see Appendix 2). A variational approach was used in the present work to compute the 3D drop shape, wherein the overall energy of the drop (the sum of the potential and interfacial energies) was successively minimized to attain the final equilibrium shape of the static droplet on the substrate. This step was achieved using *Surface Evolver* (Brakke, 1992). Complete information on the 3D shape can be extracted from the minimum energy drop configuration.

3.1 Numerical Solution

This section outlines the numerical method used to obtain the shapes of the pendant drops. To initiate the solution, an imaginary cube of liquid of a given volume is taken and its overall energy is minimized to derive the drop shape under

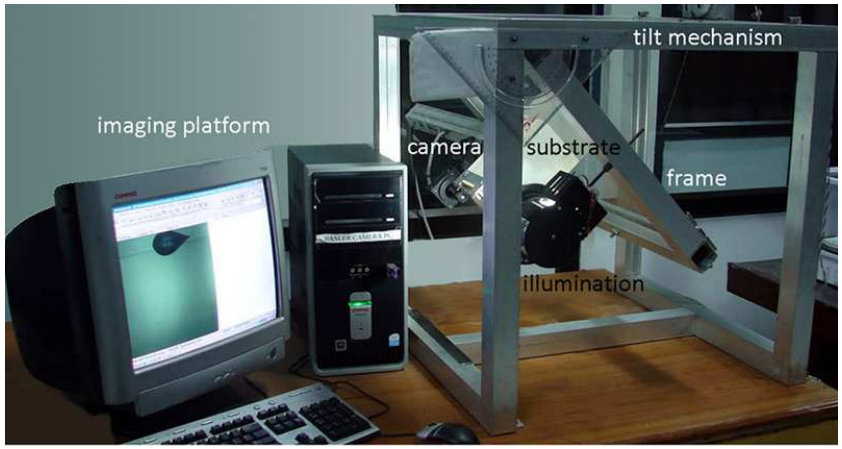

(a)

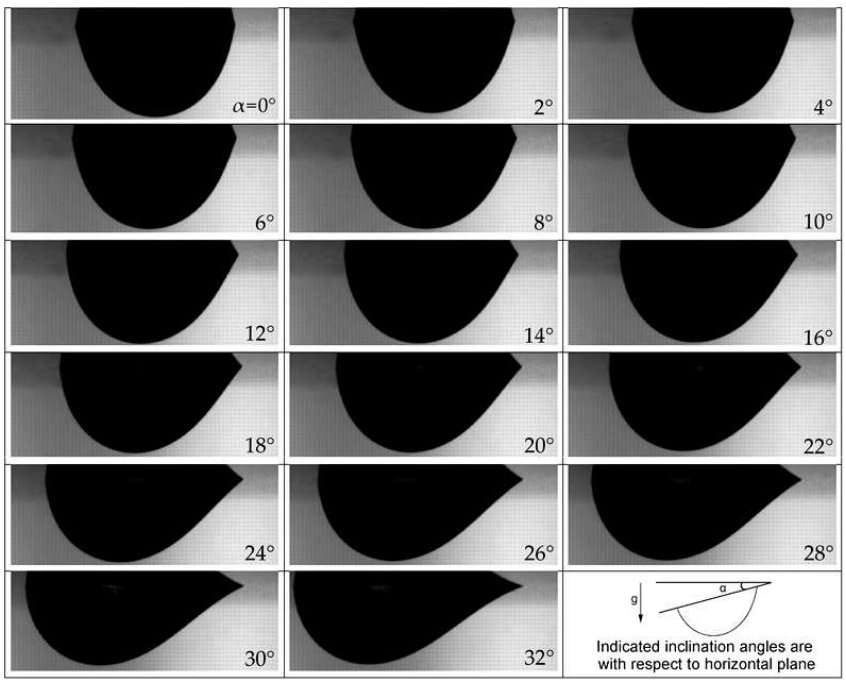

(b)

FIG. 1: (**a**) Photograph of the experimental apparatus and (**b**) images of pendant glycerin drops for various plate inclinations (α): the substrate material is aluminum, plate roughness = 1.46 μm (RMS), and drop volume = 30 μL; the camera turns with the substrate (a slight reflection of the droplet in the metal substrate can be seen at the top of each image; this helps in locating the contact points and measurement of contact angles).

equilibrium conditions. In order to provide the surface energy at the solid–liquid interface, the variation of contact angle as a function of azimuthal angle ϕ needs to be specified. Several studies have been performed in the literature to obtain suitable functions. Functions describing this variation have been suggested by El Sherbini and Jacobi (2004), Dimitrakopoulos and Higdon (1999), Milinazzo and Shinbrot (1988), and Brown et al. (1980). These are shown in Fig. 2(a). El Sherbini and Jacobi (2004) derived the following contact angle variation as a cubic polynomial for sessile drops:

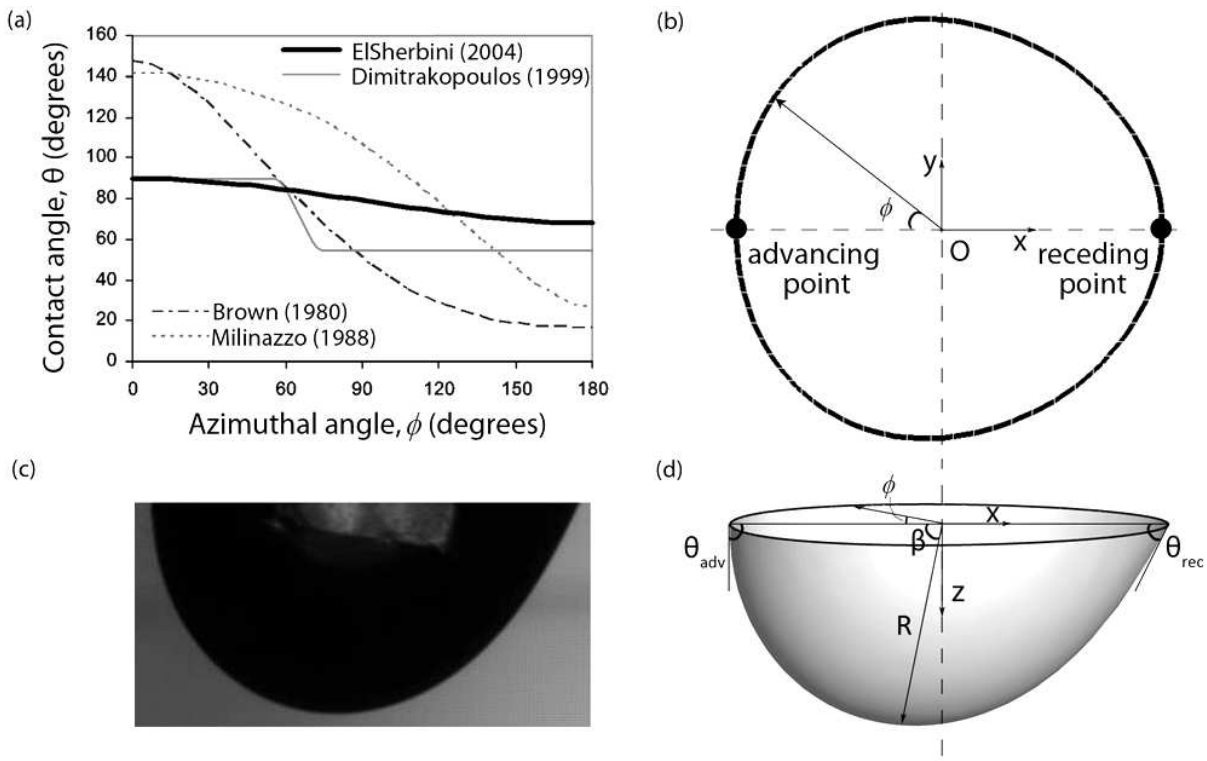

FIG. 2: (**a**) Contact angle as a function of the azimuthal angle as proposed by Brown et al. (1980), Milinazzo and Shinbrot (1988), Dimitrakopoulos and Higdon (1999), and El Sherbini and Jacobi (2004); (**b**) base contour of a 3D drop; (**c**) experimentally recorded image of a pendant drop; and (**d**) numerical simulation of a 3D pendant drop showing the azimuthal angle, which varies from 0 to 360° [advancing angle θ_{adv}, receding angle θ_{rec}, Cartesian coordinates and polar coordinates (angle β and radial distance R)].

$$\theta = 2\frac{\theta_{\max} - \theta_{\min}}{\pi^3}\phi^3 - 3\frac{\theta_{\max} - \theta_{\min}}{\pi^2}\phi^2 + \theta_{\max} \tag{1}$$

Here, $\theta_{\max}$ is the advancing angle, $\theta_{\min}$ is the receding angle, and ϕ is the azimuthal angle, as shown in Fig. 2(b). Liao et al. (2009) assumed the contact angle to vary linearly around the circumference of the drop. Equation (1), also used by Annapragada et al. (2012), was adopted in the present study. The coefficients of the terms of the cubic polynomial in Eq. (1) were obtained using boundary and symmetry conditions.

The algorithmic steps used to obtain the shape of the 3D drop on an inclined surface with the *Surface Evolver* software are the following:

1. Define a cube of liquid with an initial volume equal to the required drop volume V_D.
2. Specify the substrate surface inclination, volume constraint, and physical parameters.
3. Specify the interfacial energy on the solid–liquid contact plane $z = 0$ using the contact angle variation of Eq. (1), with $\theta_{\max}$ and $\theta_{\min}$, as inputs.
4. Specify the gravitational potential energy of the liquid as a function of the plate inclination.
5. Use the gradient descent method in *Surface Evolver* to approach the new 3D drop shape.

6. Correct for the center of the base contour (after each iteration) to calculate azimuthal angle ϕ within *Surface Evolver*.

7. Repeat Steps 3–6 until the drop shape converges to a minimum energy.

The *Surface Evolver* code used to compute pendant drop shapes was first validated for axisymmetric drops against results obtained from the axisymmetric Young–Laplace equation (Appendix 1). Figure 3 compares the shapes of a 30 μL axisymmetric pendant glycerin drop, with a uniform contact angle of 80°, predicted using *Surface Evolver* and the solution of Eqs. (A2) and (A3). The match is seen to be quite good. Figure 4 presents 3D drop images obtained from the numerical simulation of a 30 μL pendant glycerin drop for various plate inclinations. This simulation corresponds to the experimental images shown in Fig. 1(b) for an aluminum substrate of 1.46 μm roughness. The shape of a drop deposited on a rough surface is governed by the same physical equation that balances forces, although the surface roughness alters the contact angle (Bhushan and Jung, 2011). This is realized in the numerical simulation by appropriately setting $\theta_{\min}$ and $\theta_{\max}$ in Eq. (1). The correct values of $\theta_{\min}$ and $\theta_{\max}$ were obtained from the inverse method by comparison against the experiments and the method to obtain these angles is discussed in the next section. Figure 4(a) shows the shapes of the simulated drops from a direction normal to its mid-plane and these are comparable to Fig. 1(b). Figure 4(b) shows an isometric view of these 3D drops for three plate inclinations. A comparison between the experimental and numerical drop shapes can be seen in Fig. 5. The match between the two sets of data is seen to be good.

3.2 Inverse Technique for Estimating Contact Angles

As noted earlier, the contact angles reported in this study have been estimated using two methods: (1) a tangent method for experimental images using digital image processing and (2) an inverse method that minimizes the error between the experimental and numerical drop shapes; the latter being based on assumed contact angles. The inverse method minimizes the error with respect to $\theta_{\max}$ and $\theta_{\min}$ as parameters [Eq. (1)]. An algorithm for calculation of contact angles using the inverse method is presented as follows:

1. Guess $\theta_{\max}$ and $\theta_{\min}$. A good starting guess can be the respective contact angles measured using the tangent method.

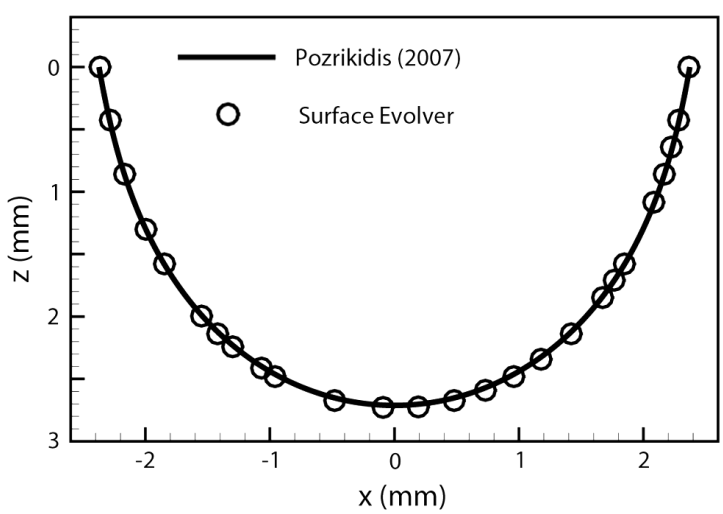

FIG. 3: Validation of the *Surface Evolver* code to predict the shape of a 3D pendant drop; the 3D shape of a 30 μL pendant glycerin drop with a contact angle of 80° is simulated using *Surface Evolver* and is compared with the solution of the axisymmetric Young–Laplace equation on the mid-plane using the parametric form suggested by Pozrikidis (2009).

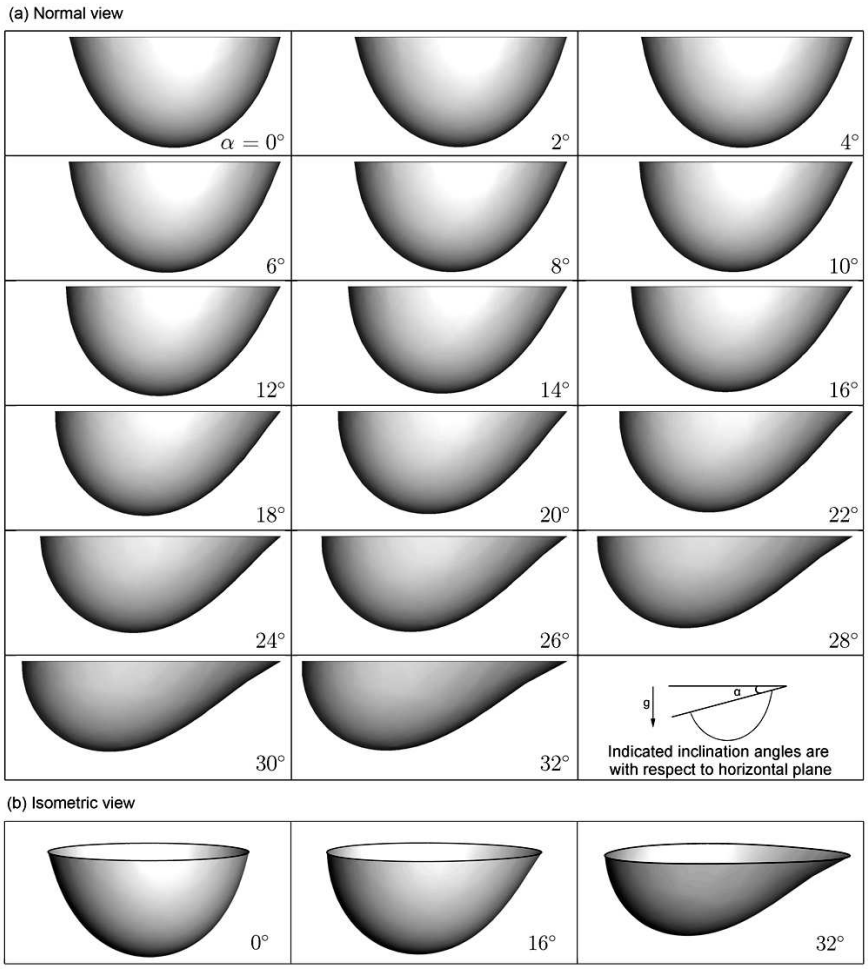

FIG. 4: (**a**) Numerical simulation of a 30 μL pendant glycerin drop on an aluminum substrate of 1.46 μm RMS roughness for various plate inclinations α and (**b**) isometric view of the simulated drops for three plate inclinations.

2. Obtain a 3D drop shape using *Surface Evolver*, as described in Sec. 3.1, for $\theta_{\max}$, $\theta_{\min}$, plate inclination, and fluid properties.
3. Interpolate the 3D triangulated surface and extract the 2D drop curve in the vertical mid-plane.
4. Calculate the RMS error between the 2D numerical and experimental drop shapes. Improve the guessed values of $\theta_{\max}$ and $\theta_{\min}$ using a suitable multivariable optimization method. An exhaustive search method has been used in the present study.
5. Repeat Steps 2–4 to minimize the RMS error obtained in Step 4 with respect to the variables $\theta_{\max}$ and $\theta_{\min}$.
6. The optimum $\theta_{\max}$ and $\theta_{\min}$, corresponding to the minimum RMS error, are reported as the advancing θ_{adv} and receding θ_{rec} angles.

Figure 6 is a contour plot of the error function with respect to $\theta_{\max}$ and $\theta_{\min}$. Error is plotted as a ratio of the RMS error between the experimental and numerical drop profiles and drop diameter D' for the corresponding plate inclination. Drop diameter D' is defined as the maximum drop span along the direction of plate inclination. In Fig. 6,

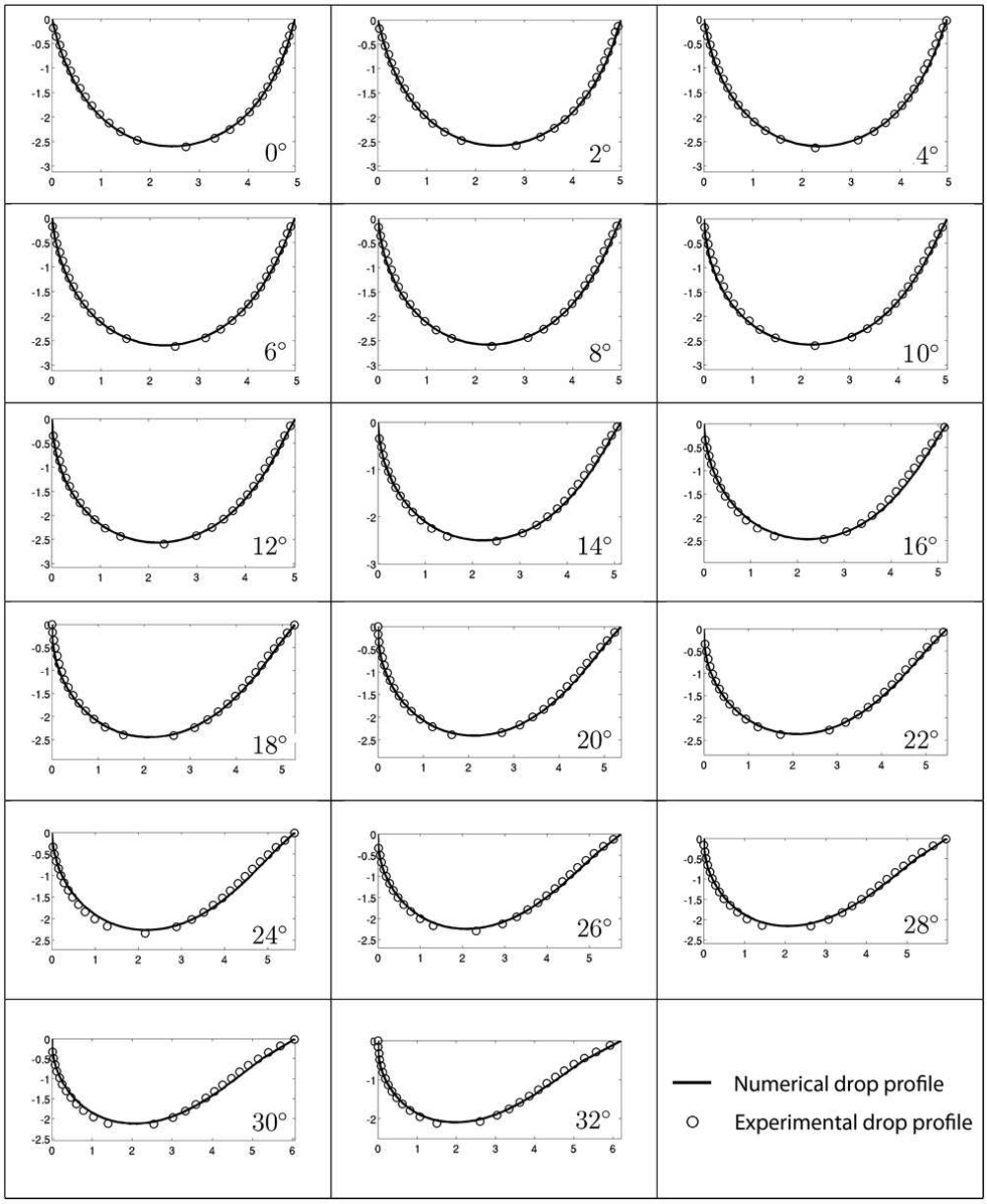

FIG. 5: Comparison of numerical and experimental drop profiles of a 30 μL pendant glycerin drop on an aluminum substrate for various plate inclinations α (RMS roughness = 1.46 μm).

it can be seen that a global minimum exists and forms the basis of the inverse method for measuring the contact angles. This error is most often below 1% and represents an acceptable match between experimental and numerical drop shapes.

A significant level of uncertainty is often involved in the contact angles measured from drop images using the tangent method. The inverse technique overcomes this uncertainty by creating 3D physical drop shapes from a numerical model and fitting 2D sections that are extracted from it to the experimental drop profile. The error associated with the fitting of the entire numerical drop curve to the experimental drop profile is small and has a very small contribution

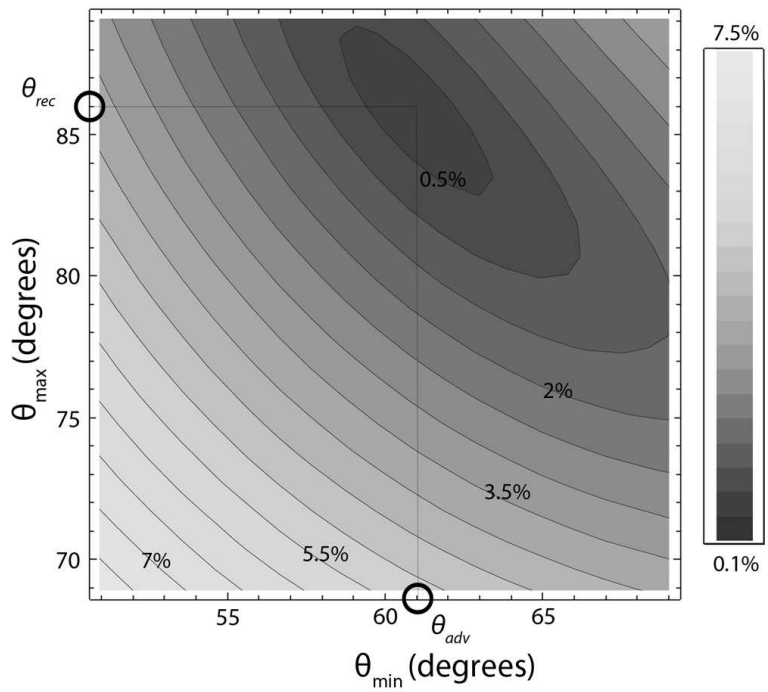

FIG. 6: Contours of error between numerical and experimental profiles for a 15 μL pendant glycerin drop on an aluminum substrate of 1.46 μm RMS roughness inclined at 16° with the horizontal; error has been presented as a ratio of the absolute difference in the drop shapes and its diameter (a clear error minimum is seen; the optimum advancing and receding angles being 86 and 61°, respectively).

from the solid–liquid–vapor interface. Therefore, the inverse contact angles reported in this study are robust for predicting not only the drop shapes but also in providing better estimates of the contact angles compared to the angles estimated from the tangent method.

3.3 Shape of the Three-Phase Contact Line

Besides the knowledge of contact angles, it is important to obtain the shape of the three-phase contact line. The droplet footprint changes with the plate inclination. From the 3D shapes of the non-axisymmetric pendant drops obtained using the variational method, the drop contours can be extracted in the $z = 0$ plane. The base contour starts with a circular shape for a horizontal drop and gets distorted as the substrate plate is inclined. Figure 7 presents the base contours of a 15 μL pendant glycerin drop on an aluminum substrate of 1.45 μm RMS roughness. Unlike the approximations of Wolfram and Faust (1978) and Brown et al. (1980), Fig. 7 shows that the contact line is not pinned everywhere but only at the receding point. With increasing inclination, the liquid mass starts shifting toward the advancing point and the resulting shapes reported in Fig. 7 are obtained. These base contours for inclined pendant drops are qualitatively similar to the experimental images of El Sherbini and Jacobi (2004), although the reference is for a sessile drop. In view of the experimental complexity involved in measuring the three-phase contact line for inclined pendant drops, numerical simulations are seen to offer a convenient alternative.

4. RESULTS AND DISCUSSIONS

Advancing and receding angles have been measured from images of pendant drops of glycerin for a range of plate inclination angles. The effect of volume and surface roughness are considered. Contact angles have been measured

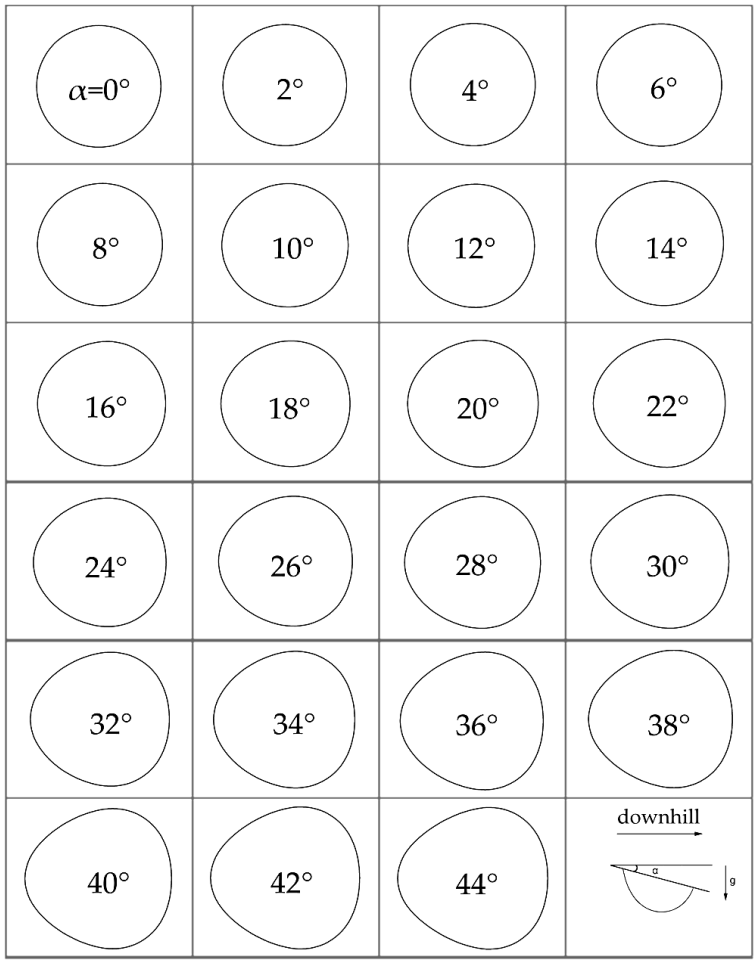

FIG. 7: Numerical simulation of the three-phase contact line for a 15 μL pendant glycerin drop on an aluminum substrate of 1.46 μm RMS roughness as a function of plate inclination α (these contact lines have been extracted from the 3D drop shapes with optimum advancing and receding angles; the diameter of the contact line for the drop over a horizontal surface was 4.1 mm.

using two methods, as noted; i.e. (1) a tangent method where the contact angles are measured from drop images using an image processing technique, and (2) an inverse method that minimizes the error between the experimental and numerical drop shapes. The contact angles corresponding to the minimum error are reported as those measured by the inverse method. Hence, for every experiment, two contact angle values have been reported. The pendant drop was taken to be stationary in this work, and instability and droplet slide-off motion form the scope of future work.

4.1 Physical Texturing

The use of contact angles provides an equivalent representation of the liquid–surface interaction at the three-phase contact line. There are no assumptions on the nature of this contact. At the same time, the force equilibrium relationship is also independent of the nature of the contact. When the proposed inverse method is employed, contact angles that reproduce experimental drop shapes and are consistent with the physical law are predicted as the model parameters.

On surfaces with isotropically distributed roughness, one can expect the Wenzel state to be realized at equilibrium. In general, a drop could be in a Cassie–Baxter state as well. With experimental images as input, the inverse algorithm would recover the contact angles of this configuration as well. In the experiments, it was expected that the drop was in the Wenzel state. This expectation was supported by the modified contact angles seen on the inclined surfaces.

Figures 8 and 9 show the contact angle variations with the surface inclination for pendant glycerin drops of 5 and 30 μL in volume, respectively. In Figs. 8 and 9, the advancing and receding angles are presented for three substrate roughness values; namely, 0.55, 1.46, and 3.98 μm for an aluminum plate. The contact angles plotted in Figs. 8(a) and 9(a) were measured using the tangent method. Figures 8(b) and 9(b) report the contact angles measured using the inverse method. The two sets of data show similar trends. It can be seen that increasing the roughness leads to a reduction in the contact angle. The entire band of advancing and receding angles shifts down by an amount proportional to the roughness, and the band lines remain nearly parallel.

The extent of reduction in the contact angle of the pendant drops with increasing roughness of a horizontal surface can be seen from the three images in Fig. 10(a). Following the Wenzel model (Berthier, 2008)

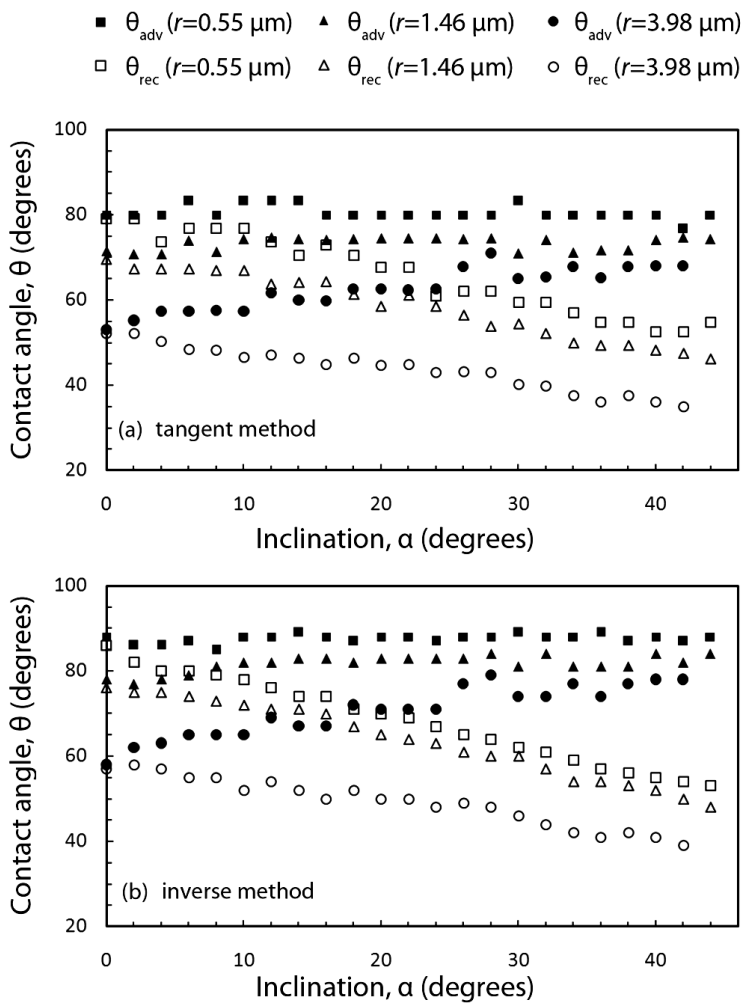

FIG. 8: Contact angle plots of 5 μL pendant glycerin drops on aluminum substrates: advancing and receding angles are plotted against the plate inclination angle for substrate roughness values of 0.55, 1.46, and 3.98 μm (see the legend description at the top); contact angles measured using the tangent method are shown in (**a**) and using the inverse method in (**b**).

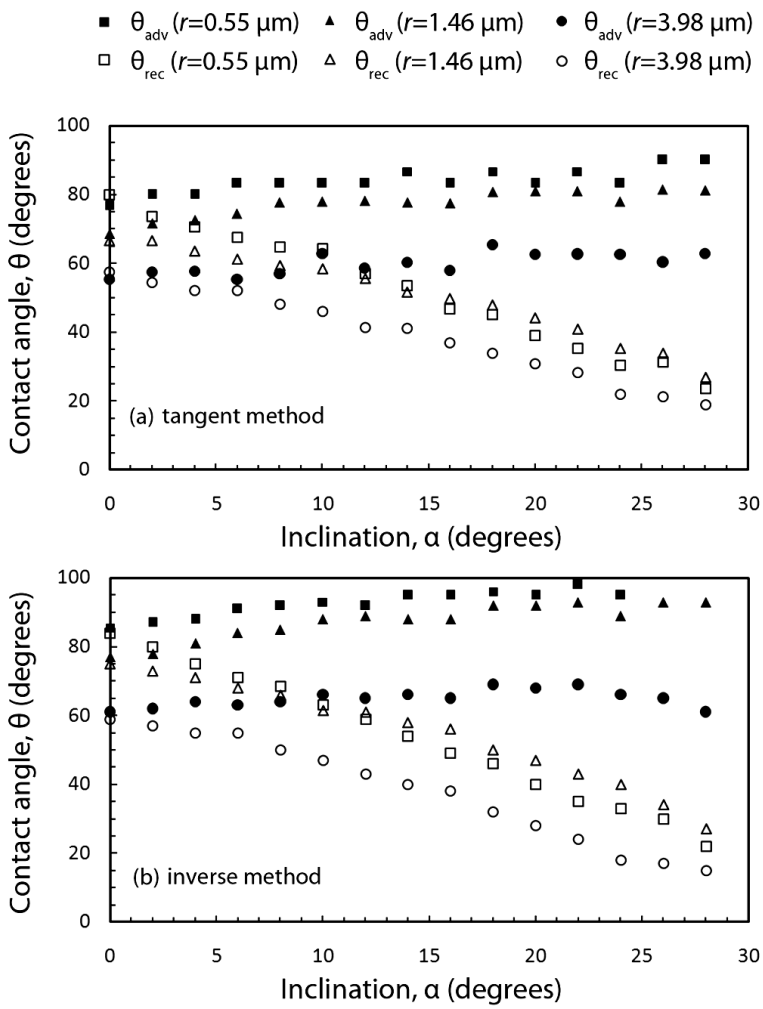

FIG. 9: Contact angle plots of 30 μL pendant glycerin drops on aluminum substrates: advancing and receding angles are plotted against the inclination angle for substrate roughness values of 0.55, 1.46, and 3.98 μm (see the legend description at the top); contact angles measured using the tangent method are shown in (**a**) and using the inverse method in (**b**).

$$\cos\theta^* = r' \cos\theta_E \tag{2}$$

where θ^* is Wenzel's contact angle and θ_E is Young's contact angle. For a horizontal plate, the contact angle for a perfectly smooth aluminum surface in Fig. 10(a) is less than 90° ($\theta_E < 90°$). Wenzel's equation predicts that if roughness $r' > 1$, then $\theta^* < \theta_E$; that is, the contact angle will be less than Young's contact angle. The same effect can be seen for the hydrophilic sessile drops shown in Fig. 10(b). The experimental data presented in Figs. 8 and 9 agree with this theory. On the other hand, for hydrophobic surfaces (i.e., $\theta_E > 90°$), an increase in the surface roughness will lead to an increase in the contact angle [see Fig. 10(b), images iii and iv].

4.2 Plate Inclination

The effect of plate inclination on advancing and receding angles is of major concern in several engineering applications. Figure 11(a) presents the variation of advancing and receding angles with plate inclination for a given surface

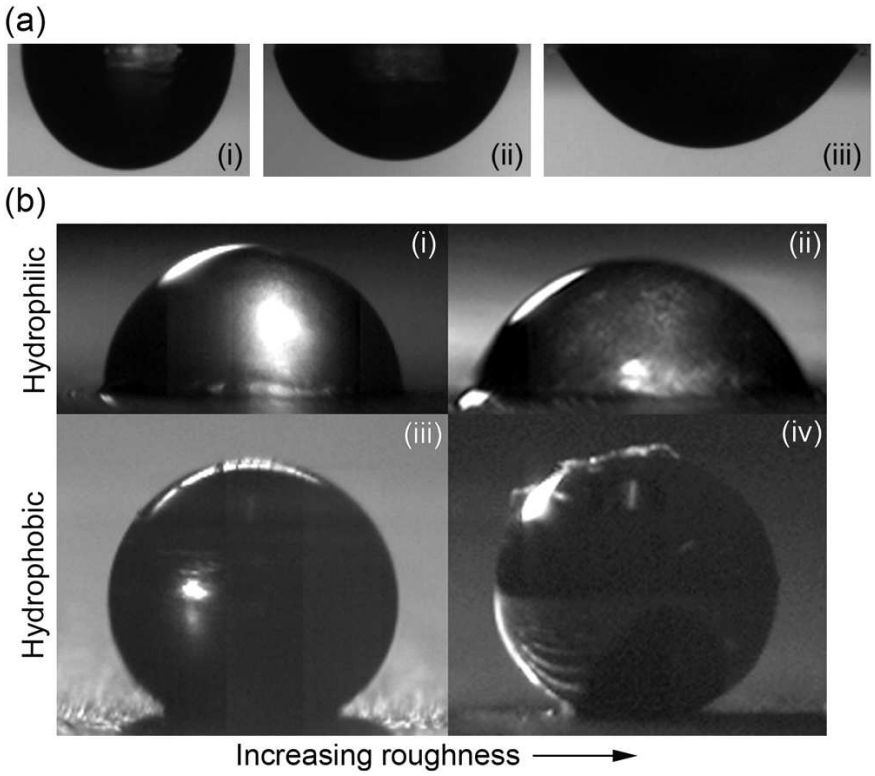

FIG. 10: (**a**) Photographs of 5 μL pendant glycerin drops on aluminum substrates of varying roughness: 0.5 μm (image i), 1.46 μm (image ii), and 3.98 μm (image iii) (the drops show an increase in wettability with increasing surface roughness); (**b**) hydrophilic and hydrophobic sessile drops on surfaces of varying roughness values: 1.4 μm (images i and iii) and 8 μm (images ii and iv) (the contact angle decreases with increase in surface roughness for hydrophilic drops, whereas it increases for hydrophobic drops).

roughness and drop volume. Figure 11(a) shows that inclining the surface causes a monotonic reduction in the receding angle. The advancing angle remains nearly constant for the range of plate inclinations (0–45°) considered in the experiments.

The receding angle normalized with the advancing angle can be considered as a function of the Bond number. Here, the Bond number is given as

$$\mathrm{Bo} = \frac{\rho g D^2 \sin\alpha}{\gamma} \tag{3}$$

with the usual nomenclature. Equation (3) represents the ratio of the component of gravity parallel to the surface that tends to slide the drop and the restoring force of the surface tension. Figure 11(b) shows the variation of $\theta_{\mathrm{rec}}/\theta_{\mathrm{adv}}$ with the Bond number for pendant drops on a textured aluminum surface of 1.46 μm RMS roughness. The functionality has a correlation coefficient of 0.97 for a linear fit, and the regression equation is obtained as

$$\frac{\theta_{\mathrm{rec}}}{\theta_{\mathrm{adv}}} = 1 - 0.303\mathrm{Bo} \tag{4}$$

The above relation is obtained for glycerin drops of volume ranging from 5 to 30 μL on a lapped aluminum substrate of 1.46 μm RMS roughness for plate inclinations between 0 and 45°. Similar empirical expressions were obtained for other surface roughness with an intercept of unity for each. Annapragada et al. (2012) performed a similar analysis for sessile drops and obtained

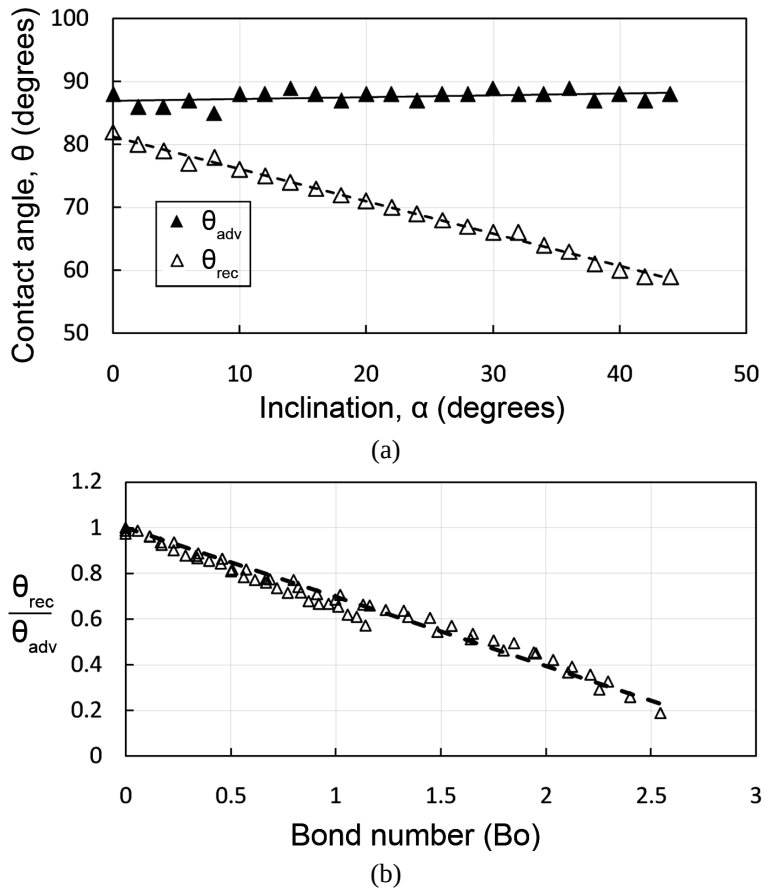

FIG. 11: (**a**) Advancing and receding angles plotted as a function of plate inclination angle for a 5 μL pendant glycerin drop on a lapped aluminum substrate (0.55 μm RMS roughness; the contact angles measured using the inverse method is reported here); (**b**) $\theta_{\rm rec}/\theta_{\rm adv}$ as a function of the Bond number for glycerin drops of volume ranging from 5 to 30 μL (plate inclination between 0 and 45° on a lapped aluminum surface of roughness 1.46 μm; the contact angles are measured using the inverse method).

$$\frac{\theta_{\rm rec}}{\theta_{\rm adv}} = 1 - 0.298{\rm Bo} \tag{5}$$

The advancing angle in the present study does not change significantly with the plate inclination, and hence

$$\frac{\theta_{\rm adv}}{\theta_o} \approx 1 \tag{6}$$

for the plate inclinations studied. Here, θ_o is the horizontal plate contact angle. Berejnov and Thorne (2007) performed inclination experiments with sessile drops. The advancing angles remained nearly constant with changing plate inclination, whereas the receding angles showed a linear reduction. The present set of results for pendant drops are broadly in agreement with the literature.

At small plate inclinations, the receding point remained pinned, whereas the advancing point started moving. Although the pendant drop was stable, it was in a state of quasi-static equilibrium with its contact line changing continuously with the plate inclination. This phenomenon can be explained by CAH. In the present experiments, pendant drops grew on the substrate from smaller to larger volumes while being deposited using a syringe. Therefore, the horizontal plate contact angles noted here corresponded to their maximum hysteresis values. As the plate was inclined, the

advancing contact angle tried to increase but could not because it had already attained the maximum possible value. The shift in drop mass due to inclination drove the contact line forward at the advancing point, maintaining the advancing angle constant. On the other hand, at the receding point, the contact angle decreased with the inclination. The hysteresis phenomena exhibited by the contact angles allowed this reduction in the receding angle from its extreme value and the receding point remained pinned to the substrate. There is a limit up to which the receding contact angle can decrease as determined by the drop volume, plate inclination, and surface roughness. The drop becomes unstable as soon as the receding contact angle goes below this limiting angle. Instabilities were not captured in our experiments because this study was only concerned with static drops.

Figure 2(b) shows the receding and advancing points on the drop contact line. Figure 12 shows the plot of drop diameter D' with the plate inclination angle for pendant glycerin drops of three volumes; namely, 5, 15, and 30 μL. The variation of drop diameter with plate inclination shows that the contact line is not pinned everywhere. The term drop diameter should be cautiously used because the drop base contour does not remain circular for non-zero plate inclinations. The drop span along the plate inclination is termed the drop diameter. A quadratic polynomial presents a good fit to the drop diameter variation with the plate inclination angle for the range of drop volumes and plate inclinations considered in this study. Figure 7 shows the variation of the shape of the three-phase contact line with the plate inclination.

4.3 Effect of Drop Volume

Figure 13 shows the contact angle plots for the three drop volumes of 5, 15, and 30 μL. As the drop volume increases, the data clearly show that the rate of change of the receding angle with the plate inclination increases. This observation can be interpreted in the following manner: higher volumes show greater sensitivity toward inclination in terms of a change in the receding angle. These results are similar to the sessile drop contact angles obtained by Berejnov and Thorne (2007). In Fig. 13, the horizontal plate contact angles are independent of the drop volume as long as the plate material and roughness are held fixed. The receding-to-advancing angle ratio as a function of the Bond number is shown in Fig. 11(b) and includes the effect of the drop volume. Keeping other factors constant, Fig. 11(b) provides information on the change of the receding contact angle with the drop size.

4.4 Pendant Drops on a Copper Surface

Discussions on the effects of physical texturing, plate inclination, and drop volume on pendant drop contact angles were presented in the previous sections for aluminum surfaces. Copper surfaces were hand lapped similar to aluminum

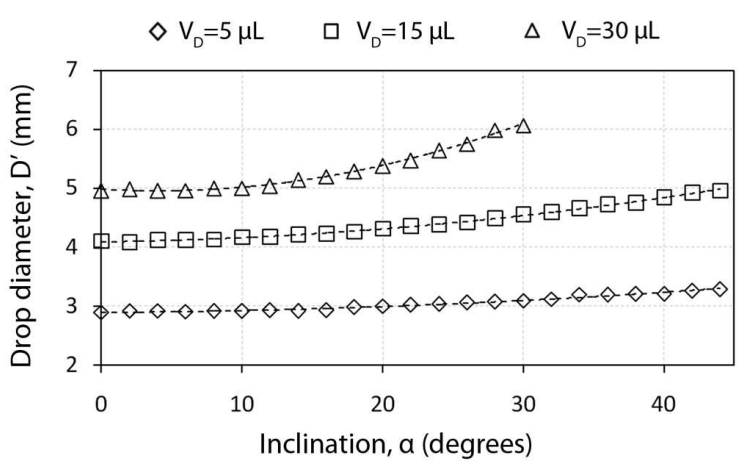

FIG. 12: Variation of pendant drop diameter with plate inclination for three drop volumes (V_D) of 5, 15, and 30 μL: a quadratic polynomial is passed through these data generated with a glycerin drop on an aluminum substrate of 1.46 μm RMS roughness; the drop diameter here is the maximum drop span along the plate inclination direction.

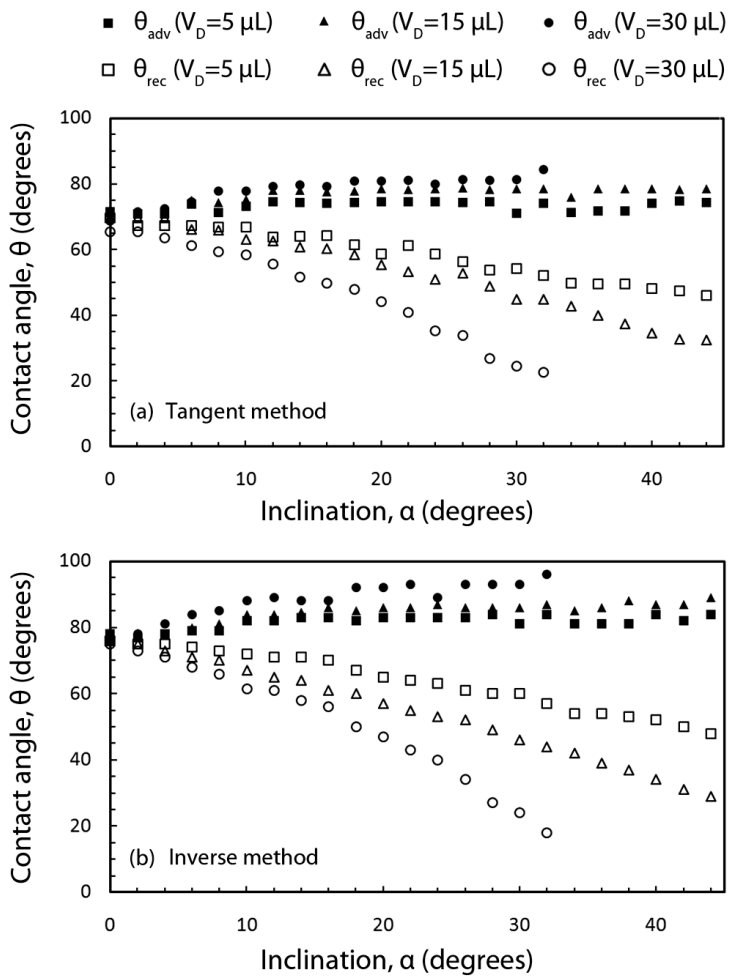

FIG. 13: Contact angle variation of pendant glycerin drops on an aluminum substrate: advancing and receding angles are plotted as a function of the plate inclination for three drop volumes (V_D) of 5, 15, and 30 μL and RMS surface roughness of 1.46 μm; the contact angles plotted in (**a**) are measured using the tangent method whereas (**b**) reports contact angles measured using the inverse method.

to obtain three roughness values; namely, 0.55, 1.46, and 2.7 μm, respectively. The results obtained for the copper surfaces were found to be similar to aluminum, and therefore were not repeated. Figure 14 illustrates the analysis performed on copper for one experimental data point. Figure 14(a) is the experimental image of a 30 μL glycerin drop on a copper substrate of 0.55 μm RMS roughness inclined at 16° with respect to the horizontal. Figure 14(d) is the 3D shape of the drop obtained by solving the mathematical model. Figure 14(b) is the base contour of this deformed drop obtained from the numerical model. Figures 14(c) and 14(e) show the comparison between the experimental and numerical drop shapes in the Cartesian and polar coordinates, respectively. Good agreement between the experimental and numerical drop shapes is clearly visible.

5. CONCLUSIONS

Glycerin drops deposited on the underside of textured aluminum and copper substrates were imaged and analyzed for contact angle data and drop profiles. The experiments were performed by varying the plate inclination, drop volume,

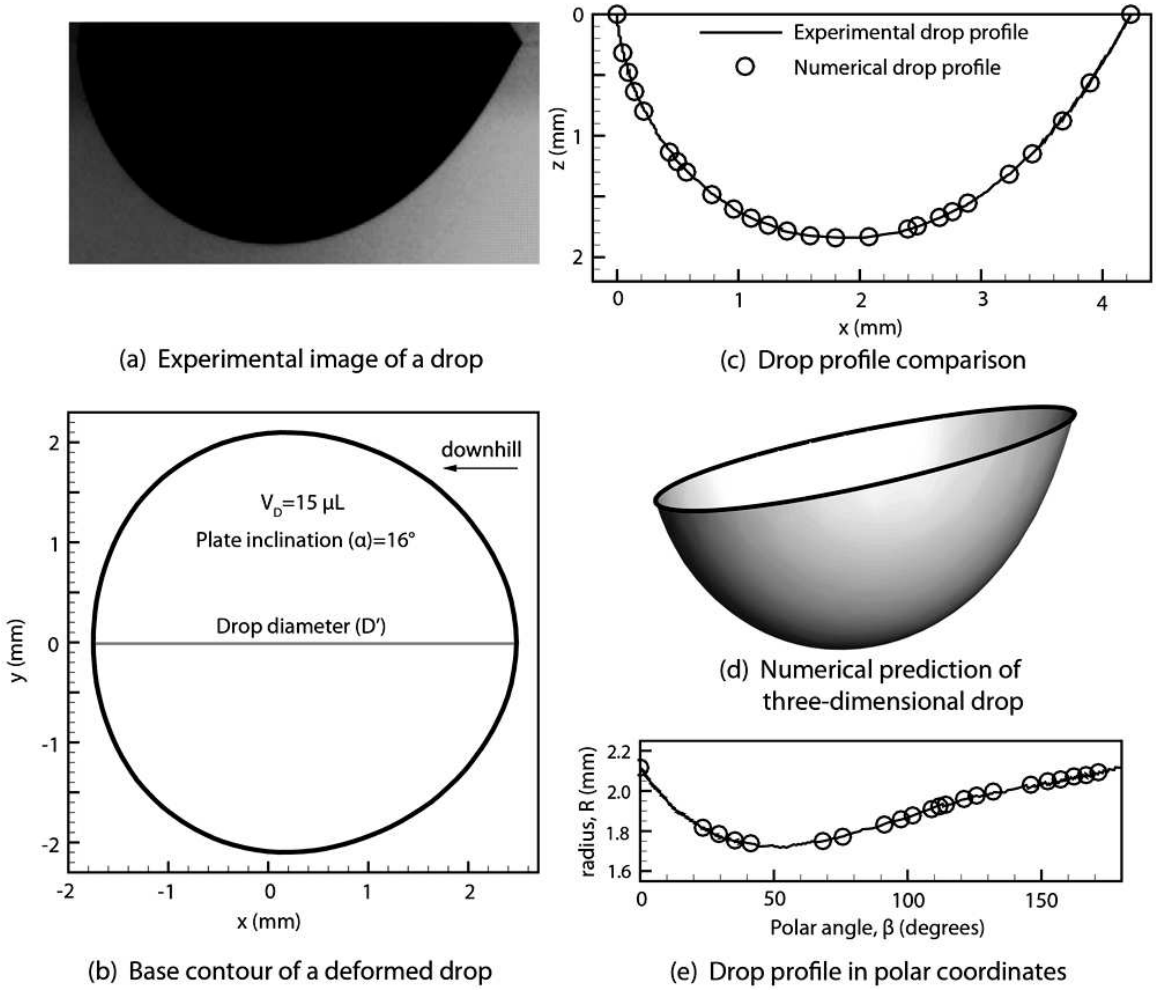

FIG. 14: (**a**) Image of a 30 μL pendant glycerin drop on a copper substrate of 0.55 μm RMS roughness; (**b**) base contour of a deformed drop; (**c**) comparison between experimental and numerical drop profiles in the Cartesian coordinates; (**d**) numerical simulation of the pendant drop considered; and (**e**) polar plot of the drop shape for experimental and numerical drops.

and surface roughness. Advancing and receding angle data as a function of plate inclination were collected on static pendant drops. A numerical model based on open domain software was used to obtain 3D shapes of non-symmetric drops. A novel method to measure the contact angles using an inverse technique was developed in this work. This method measures the contact angles of inclined pendant drops by first solving the 3D variational problem, followed by a comparison of the numerical profiles with the experimental. The error between the experimental and numerical drop shapes was minimized to obtain the best values of the receding and advancing angles. The following results have been obtained in the present work:

1. For static drops, the three-phase contact line of pendant drops has a tendency to move and spread even for small surface inclinations. The advancing point moves gradually, maintaining a nearly constant advancing angle. The receding point remains fixed, allowing the receding angle to decrease linearly with the plate inclination. The movement continues until the drop attains a new equilibrium shape.

2. Increasing surface roughness causes a reduction in the apparent contact angles. The result is in accordance with Wenzel's model, which predicts an increase in wettability for increased surface roughness values for hydrophilic surfaces.
3. The apparent contact angle of a pendant drop on a horizontal surface is not affected by volume. Receding angles fall with a greater slope for larger drop volumes, clearly showing the effect of body forces on deformation.
4. The base contour deforms from a circular shape as the plate is inclined. The numerical model predicts the base contour for inclined pendant drops, providing a convenient alternative to difficult experiments.

REFERENCES

Abdelsalam, M. E., Bartlett, P. N., Kelf, T., and Baumberg, J., Wetting of regularly structured gold surfaces, *Langmuir*, vol. **21**, pp. 1753–1757, 2005.

Adamiak, K., Capillary and electrostatic limitations to the contact angle in electrowetting-on-dielectric, *Microfluid. Nanofluid.*, vol. **2**, pp. 471–480, 2006.

Ajaev, V. S., Gambaryan-Roisman, T., and Stephan, P., Static and dynamic contact angles of evaporating liquids on heated surfaces, *J. Colloid Interface Sci.*, vol. **342**, no. 2 pp. 550–558, 2010.

Annapragada, S. R., Murthy, J. Y., and Garimella, S. V., Droplet retention on an incline, *Int. J. Heat Mass Transfer*, vol. **55**, pp. 1457–1465, 2012.

Barthlott, W. and Neinhuis, C., Purity of the sacred lotus, or escape from contamination in biological surfaces, *Planta*, vol. **202**, pp. 1–8, 1997.

Berejnov, V. and Thorne, R. E., Effect of transient pinning on stability of drops sitting on an inclined plane, *Phys. Rev. E*, vol. **75**, no. 6, p. 066308, 2007.

Berthier, J., *Microdrops and Digital Microfluidics*, 2nd ed., Waltham, MA: Hemisphere, 2008.

Bhushan, B. and Jung, Y. C., Natural and biomimetic artificial surfaces for superhydrophobicity, self-cleaning, low adhesion, and drag reduction, *Prog. Mater. Sci.*, vol. **56**, pp. 1–108, 2011.

Bico, J., Marzolin, C., and Quéré, D., Pearl drops, *Europhys. Lett.*, vol. **47**, no. 2, pp. 220–226, 1999.

Brakke, K., The *Surface Evolver, Exp. Math.*, vol. **1**, no. 2, pp. 141–165, 1992.

Brown, R. A., Orr, F. M., Jr., and Scriven, L. E., Static drop on an inclined plate: Analysis by the finite element method, *J. Colloid Interface Sci.*, vol. **73**, no. 1, pp. 76–87, 1980.

Carey, V. P., *Liquid–Vapor Phase-Change Phenomena*, pp. 342–351, New York: Hemisphere, 1992.

Cassie, A. B. D. and Baxter, S., Wettability of porous surfaces, *Trans. Faraday Soc.*, vol. **40**, pp. 546–551, 1944.

Chaudhury, M. K. and Whitesides, G. M., How to make water run uphill, *Science*, vol. **256**, no. 5063, pp. 1539–1541, 1992.

Cheng, P., Li, D., Boruvka, L., Rotenberg, Y., and Neumann, A. W., Automation of axisymmetric drop shape analysis for measurements of interfacial tensions and contact angles, *Colloids Surf.*, vol. **43**, pp. 151–167, 1990.

Dimitrakopoulos, P. and Higdon, J. J. L., On the gravitational displacement of three-dimensional fluid droplets from inclined solid surfaces, *J. Fluid Mech.*, vol. **395**, pp. 181–209, 1999.

Dingle, N. M., Tjiptowidjojo, K., Basaran, O. A., and Harris, M. T., A finite element based algorithm for determining interfacial tension from pendant drop profiles, *J. Colloid Interface Sci.*, vol. **286**, no. 2, pp. 647–660, 2005.

El Sherbini, A. I. and Jacobi, A. M., Liquid drops on vertical and inclined surfaces: I. An experimental study of drop geometry, *J. Colloid Interface Sci.*, vol. **273**, no. 2, pp. 556–565, 2004.

Extrand, C. W. and Kumagai, Y., Liquid drops on an inclined plane: The relation between contact angles, drop shape, and retentive force, *J. Colloid Interface Sci.*, vol. **170**, no. 2, pp. 515–521, 1995.

Fox, H. W. and Zisman, W. A., The spreading of liquids on low energy surfaces. I. polytetrafluoroethylene, *J. Colloid Sci.*, vol. **5**, no. 6, pp. 514–531, 1950.

Iliev, S. D., Iterative method for the shape of static drops, *Comput. Methods Appl. Mech. Eng.*, vol. **126**, no. 3, pp. 251–265, 1995.

Kalinin, Y., Berejnov, V., and Thorne, R. E., Controlling microdrop shape and position for biotechnology using micropatterned rings, *Microfluid. Nanofluid.*, vol. **5**, pp. 449–454, 2008.

Lee, Y. L., The wettability of solid surfaces modified by vacuum deposition of stearic acid, *Colloid Surf., A*, vol. **155**, nos. 2–3, pp. 221–229, 1999.

Liao, Q., Shi, Y., Fan, Y., Zhu, X., and Wang, H., Numerical simulations of the equilibrium shape of liquid droplets on gradient surfaces, *Appl. Therm. Eng.*, vol. **29**, no. 2, pp. 372–379, 2009.

Milinazzo, F. and Shinbrot, M., A numerical study of a drop on a vertical wall, *J. Colloid Interface Sci.*, vol. **121**, no. 1, pp. 254–264, 1988.

Mugele, F. and Baret, J. C., Electrowetting: From basics to applications, *J. Phys.: Condens. Matter*, vol. **17**, pp. R705–R774, 2005.

Pozrikidis, C., *Fluid Dynamics: Theory, Computation, and Numerical Simulation*, 2nd ed., New York: Springer, 2009.

Quéré, D., Rough ideas on wetting, *Physica A*, vol. **313**, nos. 1–2, pp. 32–46, 2002.

Rio, O. D. and Neumann, A. W., Axisymmetric drop shape analysis: Computational methods for the measurement of interfacial properties from the shape and dimensions of pendant and sessile drops, *J. Colloid Interface Sci.*, vol. **196**, no. 2, pp. 136–147, 1997.

Santos, M. J. and White, J. A., Theory and simulation of angular hysteresis on planar surfaces, *Langmuir*, vol. **27**, no. 24, pp. 14868–14875, 2011.

Shastry, A., Case, M. J., and Böhringer, K. F., Directing droplets using microstructured surfaces, *Langmuir*, vol. **22**, no. 14, pp. 6161–6167, 2006.

Sikarwar, B. S., Battoo, N. K., Khandekar, S., and Muralidhar, K., Dropwise condensation underneath chemically textured surfaces: Simulation and experiments, *ASME J Heat Transfer*, vol. **133**, no. 2, p. 021501, 2011.

Style, R. W. and Dufresne, E. R., Static wetting on deformable substrates, from liquids to soft solids, *Soft Matter*, vol. **8**, pp. 7177–7184, 2012.

Tuteja, A., Choi, W., McKinley, G. H., Cohen, R. E., and Rubner, M. F., Design parameters for superhydrophobicity and superoleophobicity, *MRS Bull.*, vol. **33**, pp. 752–758, 2008.

Wenzel, R. N., Resistance of solid surfaces to wetting by water, *Ind. Eng. Chem.*, vol. **28**, pp. 988–994, 1936.

Winkels, K. G., Peters, I. R., Evangelista, F., Riepen, M., Daerr, A., Limat, L., and Snoeijer, J. H., Receding contact lines: From sliding drops to immersion lithography, *Eur. Phys. J. Spec. Top.*, vol. **192**, no. 1, pp. 195–205, 2011.

Wolfram, E. and Faust, R., *Wetting, Spreading and Adhesion*, J. F. Padday, ed., pp. 213–222, London: Academic, 1978.

APPENDIX 1: PARAMETRIC FORM OF THE AXISYMMETRIC YOUNG–LAPLACE EQUATION

The Young–Laplace equation represents the force equilibrium for a static drop and takes the following form for an axisymmetric pendant drop (Pozrikidis, 2009):

$$2\kappa_m = \frac{\zeta}{l^2} + B \tag{A1}$$

Here, ζ is the symmetry axis; σ is the other axis perpendicular to ζ and $\sigma = f(\zeta)$ with the origin at the lowest point of the pendant drop; κ_m is the mean curvature given by $\kappa_m = (\kappa_1 + \kappa_2)/2$, where $\kappa_1 = -f''/(1 + f'^2)^{3/2}$ and $\kappa_2 = 1/f(1 + f'^2)^{1/2}$; $l = \sqrt{\gamma/\Delta\rho g}$ is the capillary length. One can introduce a parameter ψ, the angle made by the tangent on the drop at any point on its surface in Eq. (A1), to convert it into the following set of ordinary differential equations:

$$\frac{d\zeta}{d\psi} = \frac{\sin\psi}{Q} \tag{A2}$$

$$\frac{d\sigma}{d\psi} = -\frac{\cos\psi}{Q} \tag{A3}$$

Here, $Q = (\sin\psi/\sigma) - (\zeta/l^2) - B$ and ψ varies from 0 at the origin to θ (the contact angle) at the contact line. The boundary conditions are

$$\zeta(0) = 0 \quad \text{and} \quad \sigma(0) = 0 \tag{A4}$$

and the drop volume constraint is

$$\pi \int_{-d}^{0} \sigma^2 d\zeta = V_D \tag{A5}$$

with d as the maximum drop height in the z direction.

Equations (A2) and (A3) are solved with the boundary conditions [Eq. (A4)] using a fourth-order Runge–Kutta (RK4) method. Because the value of B is unknown to start with, the Newton–Raphson method is iteratively used with the volume constraint [Eq. (A5)] to get the correct value of parameter B.

APPENDIX 2: THREE-DIMENSIONAL YOUNG–LAPLACE EQUATION

The Young–Laplace equation for a 3D drop is given as (Pozrikidis, 2009)

$$2\kappa_m = \frac{\Delta\rho}{\gamma}\mathbf{g}\cdot\mathbf{z} + B \tag{B1}$$

Here, κ_m is the mean curvature of the liquid–air interface; $\Delta\rho = \rho_{\mathrm{liq}} - \rho_{\mathrm{air}}$; γ is the surface tension of the liquid; $B = \Delta p/\gamma$, where Δp is the excess pressure in the liquid contained within the drop. For a 3D drop surface $z = f(x, y)$, the curvature of the drop is given by

$$\kappa_m = \frac{1}{2}\frac{\left(1+f_x^2\right)f_{yy} - 2f_x f_y f_{xy} + \left(1+f_y^2\right)f_{xx}}{\left(1+f_x^2+f_y^2\right)^{3/2}} \tag{B2}$$

Here, x and y are the coordinates in the plane z = 0 of the three-phase drop contact line as shown in Fig. 2(b). Substituting Eq. (B2) into Eq. (B1) gives the governing equation for the shape of a non-symmetric drop in terms of the function $f(x, y)$. The governing equation is solved subject to the following boundary conditions:

$$f\left(S\right) = 0, \quad \text{where} \quad S\left(x, y\right) = 0 \text{ is the contact line of the drop} \tag{B3}$$

$$\nabla f \cdot \hat{n} = |\nabla f| \sin\theta \quad \text{on} \quad S\left(x, y\right) = 0 \tag{B4}$$

Here, $\hat{n}$ is a normal to the plane z = 0, and θ is the contact angle and a function of the azimuthal angle ϕ [Fig. 2(b)]. Since the excess pressure $\Delta p (= B \times \gamma)$ is an unknown, the governing equation is solved with a drop volume constraint

$$\int f\left(x, y\right) dxdy = V_D, \quad \text{given} \tag{B5}$$

Solving Eq. (B1) with boundary conditions (B3) and (B4) and constraint (B5) is a challenging problem. An alternative approach based on the variational principle has been used in the present study. It is implemented algorithmically using the open-source software, *Surface Evolver* (Brakke, 1992).

Interfacial Phenomena and Heat Transfer, 1 (1): 51–62 (2013)

COALESCENCE OF A DROPLET CLUSTER SUSPENDED OVER A LOCALLY HEATED LIQUID LAYER

A. A. Fedorets,[1] I. V. Marchuk,[2,3,*] & O. A. Kabov[2,4]

[1]*Tyumen State University, Semakova Street 10, Tyumen, 625003, Russia*

[2]*Institute of Thermophysics, Russian Academy of Sciences, prosp. Lavrentyev 1, Novosibirsk, 630090, Russia*

[3]*Novosibirsk State University, Pirogova 2, Novosibirsk, 630090, Russia*

[4]*Tomsk Polytechnic University, Lenin Avenue 30, Tomsk, 634050, Russia*

[*]Address all correspondence to I. V. Marchuk, E-mail: marchuk@itp.nsc.ru

Experimental results on the coalescence of a dissipative structure "droplet cluster" obtained by means of high-speed thermal imaging are presented. It is found out that coalescence of a single cluster droplet with a liquid layer can generate a capillary wave on the interphase, and propagation of this wave causes coalescence of the whole cluster during several thousandths of a second. Cluster coalescence is accompanied by a temperature jump on the interphase. With cluster restoration, the surface temperature of a liquid layer returns gradually to the initial level. The interphase temperature under the droplet cluster can be both lower and higher than the interphase temperature without this cluster, i.e., the cluster can not only initiate both heat and mass transfer between liquid and gas, but also deteriorate it.

KEY WORDS: *levitating drops, evaporation, thermocapillary convection, capillary wave, thermal imaging, temperature jump on the interphase*

1. INTRODUCTION

Many engineering processes and laboratory experiments include liquid layer heating by an intensive localized heat source on a substrate or by a powerful localized radiation beam. For instance, this situation occurs at cooling of microelectronic equipment, and locally the heat flux density can be 1 kW/cm^2 (Mahajan et al., 2006). Boiling, evaporation, thermocapillary convection, and break of liquid layers are studied at local heating [e.g., see Nepomnyaschy et al. (2002), Zaitsev and Kabov (2007), Andreev et al. (2008), Marchuk (2009)].

At intensive local heating and evaporation of water and some other liquids (glycerin, benzyl alcohol, ethylene glycol), the spatially ordered structure "droplet cluster" can be observed. This is a structure of dozens or hundreds microdroplets levitating parallel to the horizontal liquid-gas interphase at a distance comparable to the droplet diameter, Fig. 1. The droplet cluster was detected both at radiation of a thin liquid layer by a light beam (the area of 8×10 mm^2) (Fedorets, 2004) and at heating of a liquid layer from the substrate by a heater with diameter of 1 mm (Fedorets, 2005). The local character of interphase heating as well as the open character of the system (i.e., its ability to remove efficiently heat fluxes and vapor flows from the heated region of interphase) are principally important for generation and stable existence of the droplet cluster. Some analogy with this effect is observed with the Leidenfrost effect, when droplets are held up by a layer of vapor over a heated surface due to intense evaporation of the drops, but in our case the condensation of vapor is on the drops, because the drops grow in time.

There is the threshold liquid temperature in the zone of heating, below which the cluster can not be formed, i.e., the droplets precipitated on the liquid surface coalesce with the layer. Under atmospheric pressure and air temperature T_g of about 20–25°, water surface temperature T_S in the zone of local heating should not be lower than 50° (Fedorets,

 © 2013 by Begell House, Inc.

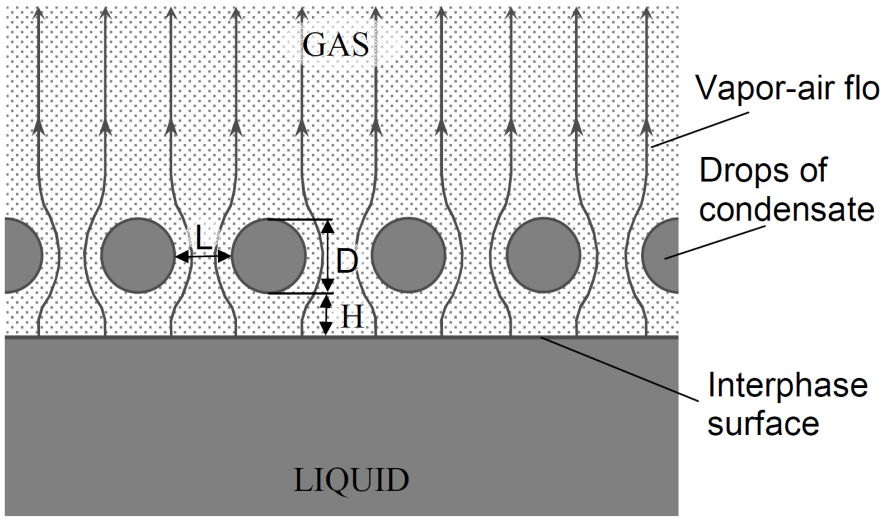

FIG. 1: Schematic drawing of spatially ordered structure — "droplet cluster."

2004). It is determined in Arinshtein and Fedorets (2010) that the vertical temperature gradient in the gas medium above the locally heated region can be ∼30 K/mm. If the temperature is relatively high, a pattern of precipitated condensate microdroplets with the size of ∼10 μm in the form of continuously changing light irregular polygons can be observed above the liquid surface in a cup of tea or coffee (Schaefer, 1971). Transformation from uniform to local heating leads to a qualitatively new phenomenon.

Droplets come to the cluster from the gas environment, where they nucleate and undergo the first stage of condensation growth. Initially these droplets are the fog droplets, generated at vapor condensation, which mix with cold air, while moving up from the heated surface. If the typical size of fog droplets for water is ∼10 μm (Raist, 1984), the size of cluster droplets is about 50–100 μm (Fedorets, 2005). The spatially ordered structure close to the structure of the plane hexagonal lattice is typical for the cluster, Fig. 2. The cluster has clearly defined boundaries, and its shape is determined by the geometry of the locally heated region of the liquid surface (Fedorets, 2004, 2005). The cluster droplets are subject to continuous condensation growth, the rate of which is proportional to heating power; at this, the linear dependence of area S of the spherical droplet surface on time is observed, Fig. 3. Usually, the droplets of cluster have almost the same diameter, Fig. 2(a), but the sizes of simultaneously levitating droplets can differ significantly because the moment of droplet penetration into the cluster is random, Fig. 2(b). At this, the height of levitation H

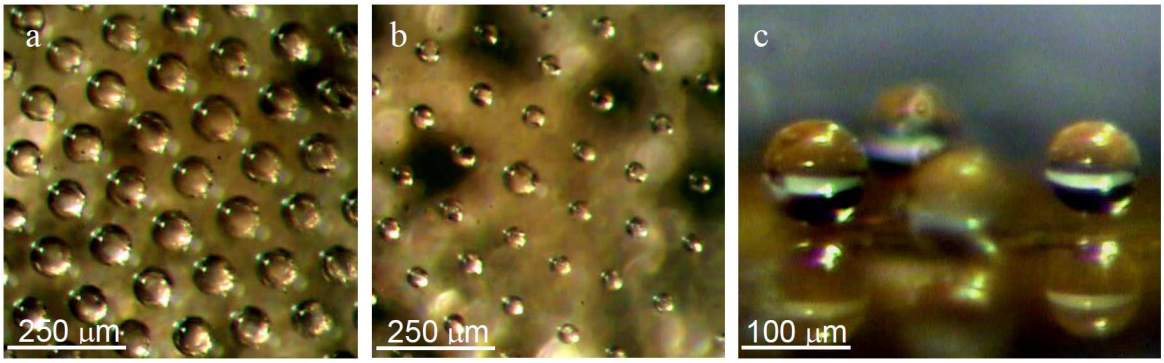

FIG. 2: Examples of clusters of water microdroplets: (**a, b**) top view; (**c**) side view (under the droplets we can see their specular reflections from the surface of liquid layer).

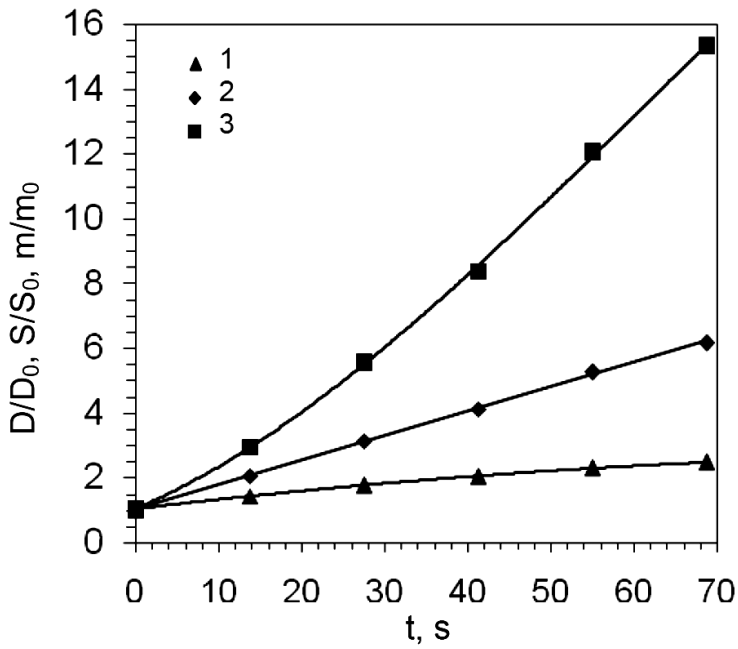

FIG. 3: Changes in diameter (1), spherical surface area (2), and mass (3) of cluster droplets in the process of their condensation growth. Values D_0 = 21.6 μm, S_0 = 1470 μm^2, and m_0 = 5.3 ng correspond to the moment of measurement beginning, t = 0. Water layer, cluster induced by the metal heater of 1 mm diameter built into the substrate [according to (Fedorets, 2011)].

and droplet diameter D are connected by inverse dependence, $H \approx 1/D$. Geometrical sizes of cluster droplets were measured in detail in Fedorets (2005, 2011), Shavlov et al. (2011), and Shavlov and Dzhumandzhi, (2012).

It is shown experimentally in Fedorets et al. (2011) that cluster droplets levitate above the liquid surface, Fig. 2(c), because of the influence of the vapor-air flow generated by intensive liquid evaporation (the Stokes mechanism of levitation). The question of the mechanism of droplets' interaction (mutual attraction at large distances and repulsion at small distances) is still unsolved. The similarity of the structure of dust plasma crystals, intensively studied in Thomas et al. (1994) and Fortov et al. (2004), and structure of the droplet cluster are discussed in Shavlov and Dzhumandzhi (2010). An assumption of similar interaction mechanisms in dust crystals and droplet clusters is considered. According to Shavlov and Dzhumandzhi (2010), the Coulomb forces, related to discharge accumulation in cluster droplets and on the interphase, are three orders less than the droplet weight.

According to investigations, this phenomenon is well reproduced in experiments of different authors, and it does not require expensive equipment for its implementation. The droplet cluster has some useful properties; for instance, the small size of droplets located close to the interphase, and cluster keeping after disconnection of heat load ($\sim$10 s). The above stated can soon lead to practical application of this phenomenon, e.g., for determination of the physical properties of liquid. In Fedotets (2008), cluster microdroplets have been already used as the natural tracers for flow visualization in the gas phase directly near the interphase. Understanding the mechanism of droplet cluster formation can allow the conclusion about possible formation of the ordered structures of microdroplets in thundercloud and fog, and these structures can achieve some specific properties such as surface tension and shear viscosity (Shavlov and Dzhumandzhi, 2010). Moreover, the cluster generates the droplets, naturally suspended in the atmosphere, with a significant temperature difference at the upper and lower boundaries (Arinshtein and Fedorets, 2010), which gives the unique possibility for investigation of evaporation and condensation as well as thermocapillary convection in the microscale.

Nevertheless, the possible role of the above-mentioned evaporation, condensation, and thermocapillary convection in the mechanism of droplet cluster formation is as yet unclear. An adequate mathematical model of this phenomenon

has not been developed until now. The mechanism and conditions of natural break of the cluster have not been studied in detail. In the current research, we present experimental results on coalescence of the droplet cluster with the layer; these data were obtained with application of high-speed thermal imaging. The effect of droplet cluster on the processes of heat and mass transfer between liquid and gas medium was studied.

2. EXPERIMENTAL METHODS

A cylindrical duralumin cuvette was used for generation of the droplet cluster, Fig. 4. A copper rod of round cross section (R_{heater} = 0.5 mm) with a length of 5 mm is glued in the center of the cuvette bottom; this rod serves as the heating element. The rod is heated by electric current passing through the nichrome wire wound around the lower part of the rod. The gap between the heater and the cuvette is filled by epoxy resin with relatively low heat conductivity, which allows us to have a localized heat source on the cuvette bottom.

Experiments were carried out with degassed distilled water containing natural microadmixtures of surfactants in the cuvette exposed to the air in the laboratory room. In all experiments, the layer thickness was h_0 = 380 $\pm$ 10 μm, and it was determined by the volume of liquid poured into the cuvette directly before the experiment (with the use of Lenpipet Stepper dispenser, tip of 5 ml, relative dosing error of $\pm$0.3%). Liquid at the layer periphery was in thermodynamic equilibrium with the ambient air, whose temperature T_{g0} was 22 $\pm$ 1°. The electric power of the heater was measured discretely; it took one of the following values: 0.31, 0.39, 0.49, 0.60, or 0.72 $\pm$ 0.005 W. At this, the temperature stabilized on the interphase above the heater center $T_{S\,\max}$ and took one of five following values: 78.1, 82.6, 86.6, 90.1, or 92.8 $\pm$ 0.2°, respectively.

3. METHOD OF TEMPERATURE MEASUREMENT ON THE INTERPHASE

To register temperature distribution on the interphase, the thermal imager itanium 570 M was used (spectral range of 3.7–4.8 μm, matrix of 640 $\times$ 512, measurement accuracy of $\pm$ 1%, NETD $<$ 25 mK). The accuracy of absolute temperature measurements is ∼0.5 K (1% of the scale range), the accuracy of measurements of temperature differences is defined by sensitivity, which is defined by a parameter called NETD (noise equivalent temperature difference). For IR camera Titanium 570M, NETD is less than 25 mK. The lens "L0120 – MW x1 2.0 Jade" for the scale of 1:1 was applied; at this, the pixel size was 15 $\times$ 15 μm. For this lens, the image field flatness is $\pm$ 0.3 mm. It is quite enough for simultaneous temperature measurements of droplets and liquid surface because the distance between the layer surface

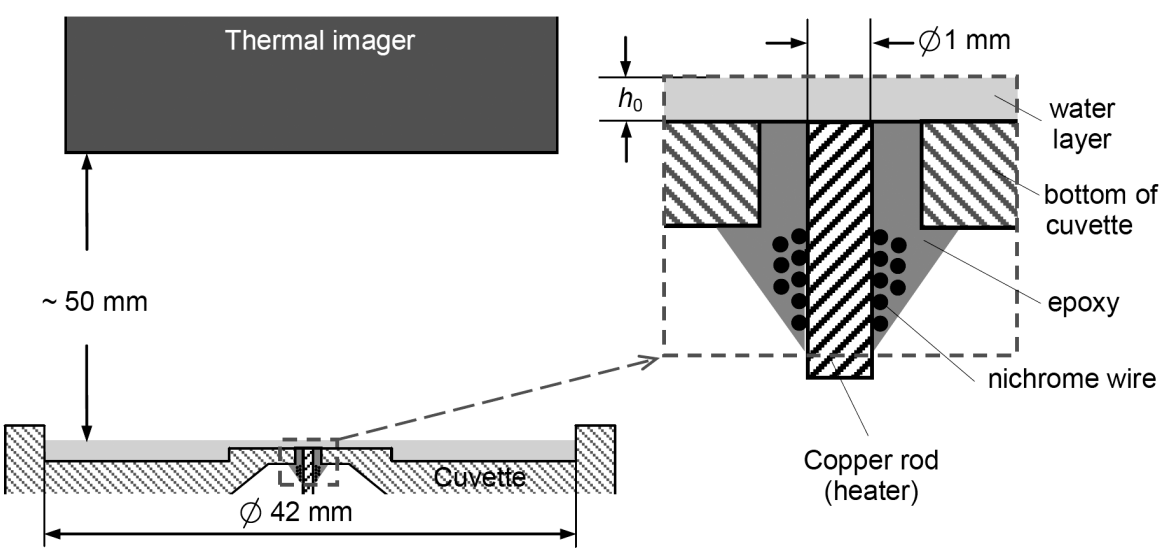

FIG. 4: Scheme of experiment.

and top of the droplet less than 0.3 mm. Measurement frequency varied from 25 to 1500 Hz. At high frame frequency (>115 Hz), not the whole matrix was scanned, but only the window with the size of 132 × 132 pixels. The method of temperature measurements on liquid surfaces with high temperature gradients is presented in Kabov et al. (1996). In particular, the questions related to radiation of the inner liquid layers and arising measurement errors, which can be significant for such semitransparent liquids as alcohols, were considered. The high absorption coefficient of water, α = 34.7 mm^{-1} within the spectral range, registered by the thermal imager, allows an assumption that the average temperature of a thin surface layer of liquid is measured (the layer thickness is <10 μm). The water emissivity in the spectral range, registered by the thermal imager, is within 9.75–9.85. Factory calibration of the setup was used for recalculation of the measured intensity of IR radiation to the values of temperature with taking into account the value of water emissivity coefficient equal to 0.98.

An example of temperature distribution over the interphase is shown in Fig. 5 for different heater powers. Here, the spatial coordinate is rated by heater radius R_{heater}, and the temperature is rated by $T_{S\,\max}$ in the region of interphase near the heater center, individual for every dependence,

$$T_{S\,\max} = \frac{1}{4}\left[T_{S\,\max(1)} + T_{S\,\max(2)} + T_{S\,\max(3)} + T_{S\,\max(4)}\right] \tag{1}$$

where $T_{S\,\max(1)}$, $T_{S\,\max(2)}$, $T_{S\,\max(3)}$, and $T_{S\,\max(4)}$ are the maximal temperatures on the interphase in each of four rectangular fragments of the image, located symmetrically relative to the heater center (two fragments are shown in Fig. 5, the size of each fragment is 9 × 9 pixels). Expression (1) allows proper determination of $T_{S\,\max}$ for every value of the heater power, even in the presence of cluster, whose droplets partially overlap the interphase and have the lower temperature.

As can be seen in Fig. 5, in the whole working range of the heater power, the heat field on the interphase is not undergone to qualitative reconstructions. The heat source is localized well, and a drastic drop of temperature occurs

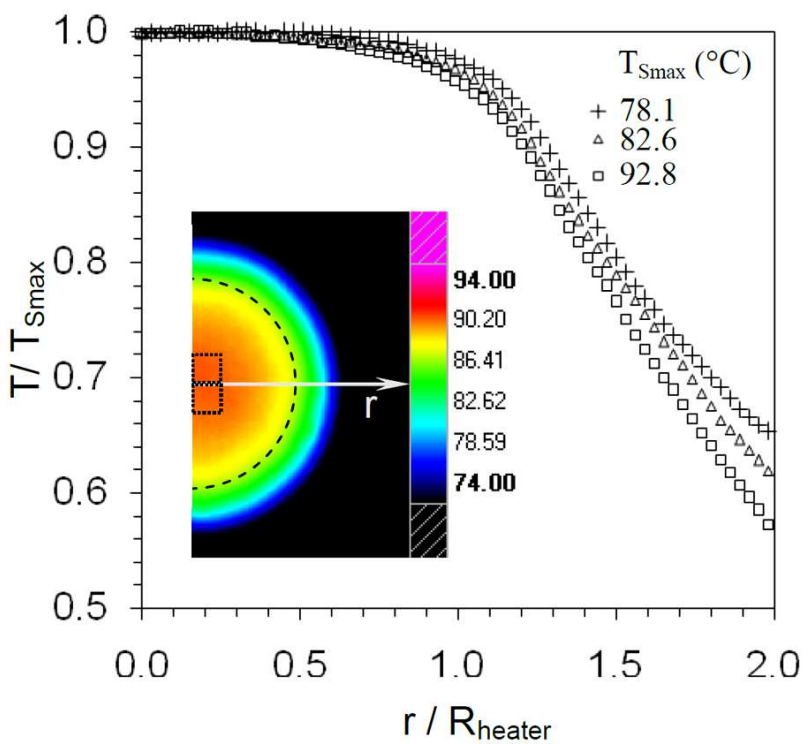

FIG. 5: Temperature on the layer interphase versus distance to the heater center. In the IR image, squares outline the fragments used for calculation of $T_{S\,\max}$, dashed circumference shows the boundary of the heater.

in the heat-insulating resin layer around the heater. In the area of cluster existence ($r/R_{\mathrm{heater}} < 1$), the temperature decreases gradually with distance from the heater center; at this, the temperature difference within this area does not exceed 5% of $T_{S\,\max}$.

4. RESULTS AND DISCUSSION

Spontaneous coalescence of the droplet cluster can be easily observed and traced by any continuous video record of this phenomenon. However, coalescence is so fast that on a video record with the standard frame frequency of 25 fps, this phenomenon is observed as "instantaneous" disappearance of the cluster. Details of the process can be observed only on a video with frequency of at least 1000 frames per second, Fig. 6. It was found out that the whole cluster "disappears" in 3 ms as a result of coalescence of a single droplet initiator (in the frame before coalescence beginning, it is outlined by a solid line).

Droplets coalesce with the layer leaving characteristic "cold" traces on the interphase, Fig. 6. The concentric symmetry and propagation velocity of the front of cluster destruction (∼70 cm/s) prove that coalescence is caused by the capillary wave on the interphase. In approximation of a thin layer, phase velocity υ of the capillary waves is determined by classical relationship (Landau, 1987),

$$\upsilon = \sqrt{\frac{2\pi\sigma}{\lambda\rho}} \tag{2}$$

where σ and ρ are surface tension and density of liquid, and λ is the wavelength.

The principle possibility for capillary wave formation, propagating with a velocity of ∼70 cm/s, exists in the whole range of values of surface tension of water with surfactant admixtures (σ = 30–74 mN/m). The detailed investigation of parameters of the wave process on the interphase, causing cluster coalescence, relates to application of specialized experimental equipment, and it is beyond the framework of the current research.

High-speed thermal imaging allowed registration of the effect of droplet cluster on the heat and mass transfer processes on the liquid-gas interphase, Fig. 7. Instantaneous cluster coalescence is accompanied by an expressed temperature jump on the interphase. With cluster restoration, the temperature of the surface layer returns gradually to the initial level. The nomenclature $T_{S\,\max(d)}$, used in the diagram, indicates average values of $T_{S\,\max}$ during the last four seconds before the moment of droplet cluster coalescence, i.e., it is the equilibrium temperature of interphase under the droplet cluster. Below, the main attention will be paid to such a parameter as temperature jump $\Delta T_{S\,\max}$ on the interphase at the moment of cluster coalescence,

$$\Delta T_{S\,\max} = T_{S\,\max 0} - T_{S\,\max(d)} \tag{3}$$

where $T_{S\,\max 0}$ is the average value of $T_{S\,\max}$ during the first two seconds after droplet cluster coalescence. Factors influencing the choice of the time length of averaging $T_{S\,\max}$ are different with or without a cluster. With droplet cluster, the process is quite steady state during measurement, and extended (4 s) interval averaging $T_{S\,\max(d)}$ increases

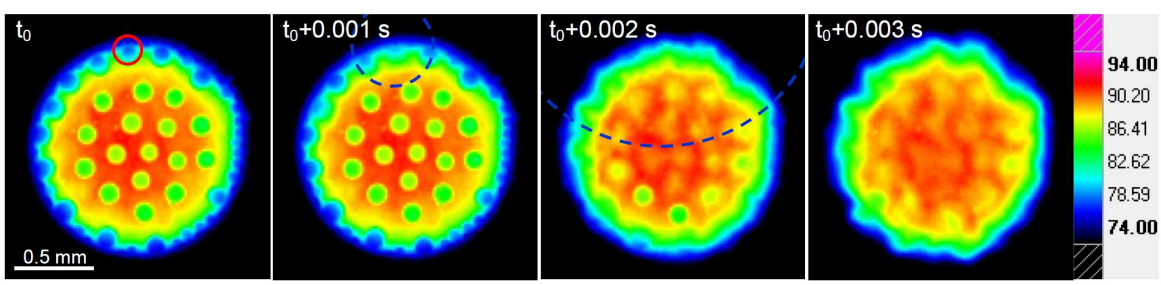

FIG. 6: Effect of "spontaneous" coalescence of the droplet cluster. The coalesced first drop is circled by the solid line. The dashed line shows an approximate position of the capillary wave front.

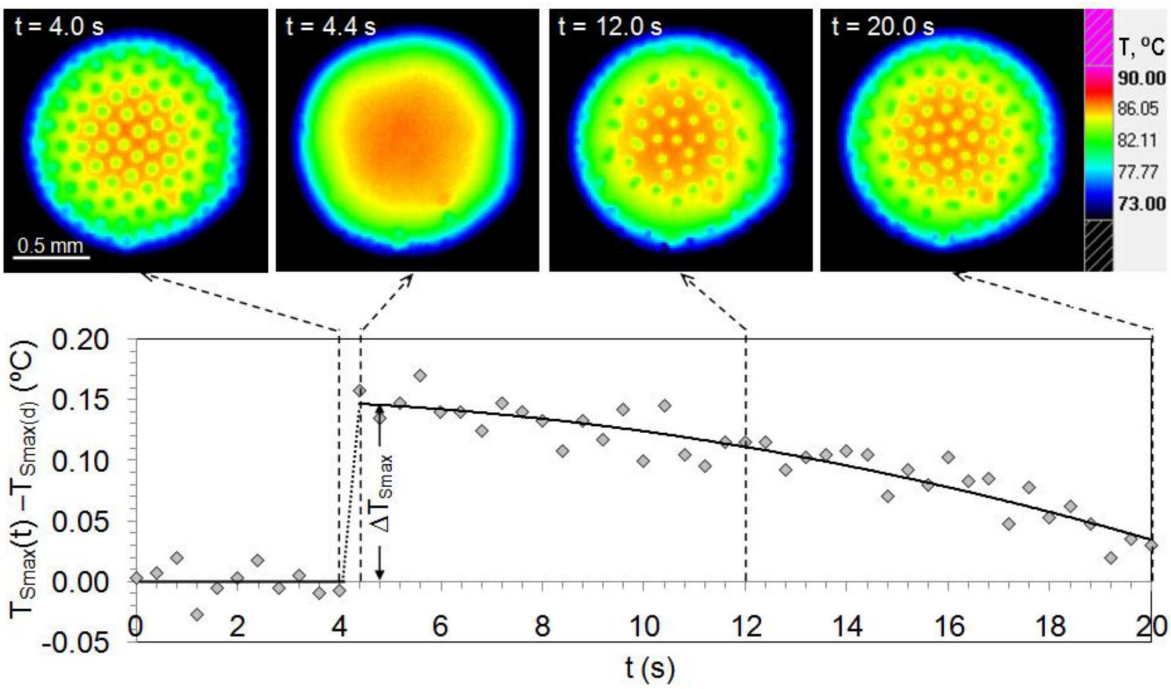

FIG. 7: Temperature jump of the interphase due to droplet cluster calescence. Temperature $T_{S\,\max 0}$ = 86.6°, separate video fragments used for diagram construction are shown additionally.

the accuracy of measurements. Restoration of the cluster begins immediately after the coalescence, according to the extent of increasing the area of the cluster increase and its effect on the temperature of the surface layer. By definition, $T_{S\,\max(0)}$ characterizes the surface layer in the absence of drops, which is rightly only the first 2–3 s after the coalescence. Hence, the averaging interval $T_{S\,\max(0)}$ is equal to 2 s.

The diagram of dependence between $\Delta T_{S\,\max}$ and temperature on the interphase under the central part of the heater (data correspond to five discrete levels of heater power with other things being equal) is shown in Fig. 8. IR cluster images in parts of a second before coalescence are shown additionally there. It is obvious that the droplet diameter increases significantly with a rise of heater power. The cluster effect on the surface layer temperature can be reproduced stably; at this, the amplitude of the registered temperature jumps exceeds significantly the error level of the used thermal imager. Every point in Fig. 8 corresponds to 150 measurements. In sum, we can distinguish following new experimental facts: (i) characteristic value $\Delta T_{S\,\max}$ makes up the tenths of a degree; (ii) duration of the period of temperature restoration on the interphase after cluster coalescence is measured by tens of seconds, Fig. 7; (iii) the interphase temperature under the droplet cluster can be both higher and lower than the interphase temperature without a cluster.

The possible physical mechanisms, explaining the above-mentioned facts, can be as follows: (i) the sequences of "instantaneous" injection of relatively cold cluster droplets into the heated liquid layer; (ii) the flows, mixing liquid in the layer, initiated by droplet coalescence; (iii) the processes of heat and mass transfer in cluster droplets, which actively effect the air-vapor jet above the locally heated region of the layer.

Actually, when coalescing with the layer, the cluster droplets generate the local areas on the interphase with the temperature, decreased by several tenths of a degree; these areas can be clearly seen in Fig. 6. The heat effect depends on the temperature and volume of injected liquid. With an increase in the temperature of the surface layer from 78 to 93°, the volume of a single droplet at the moment of cluster coalescence increases approximately by a factor of 22; however, on the contrary, the number of droplets, Fig. 8, decreases by 20 times. Dependence of the volume of injected liquid $V = nV_1$ on the temperature of the surface layer is shown in Fig. 9 (n is the number of coalescing droplets,

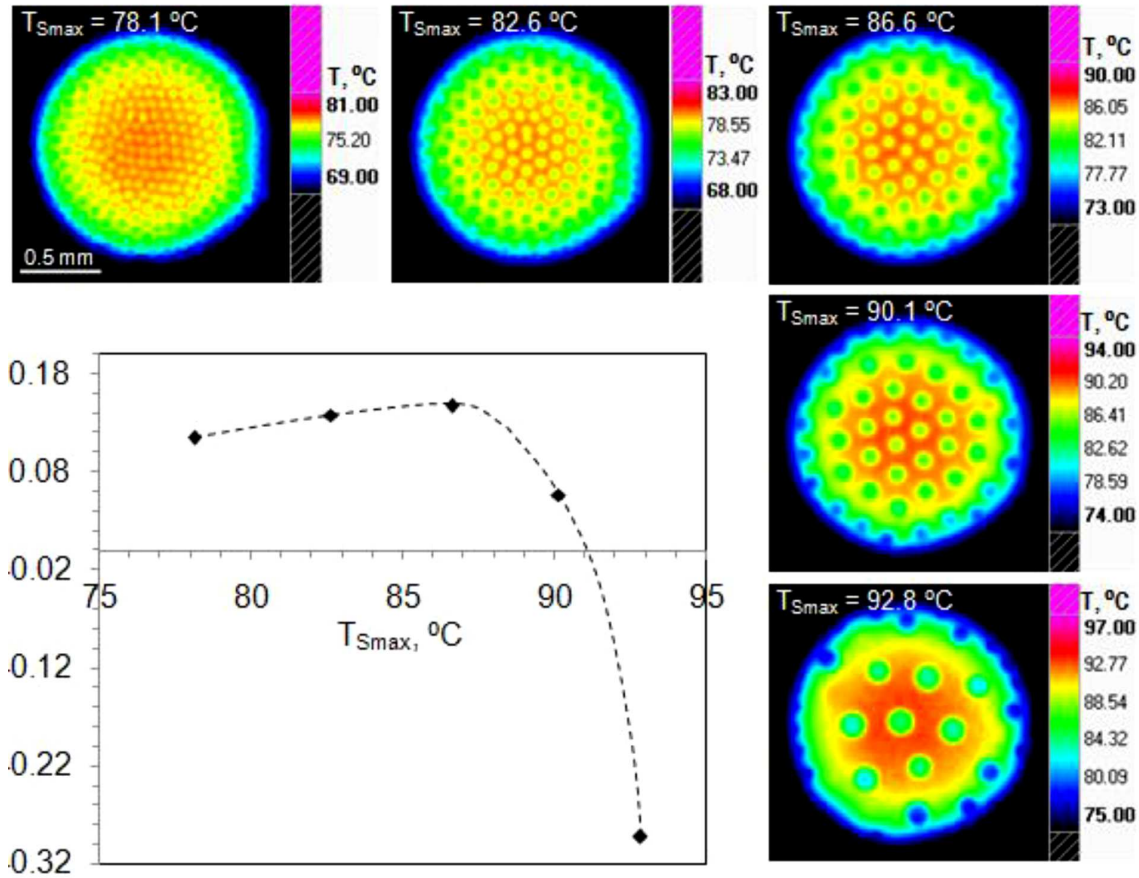

FIG. 8: Dependence of amplitude and sign of the temperature jump on the interphase on the liquid temperature in the zone of local heating of the layer.

V_1 is the volume of a single droplet). This dependence is not monotonous: the knee corresponds approximately to 90°, i.e., the temperature at which the temperature jump at coalescence changes its sign, Fig. 8. The volume of injected fluid is less than one order of magnitude of the layer volume and thermal footprint relaxes in a few milliseconds, Fig. 6. Moreover, the cluster droplets are always colder than the liquid layer [i.e., this mechanism cannot explain the experimental fact of $T_{S\,\max}$ increase after cluster destruction (Fig. 7)].

Local areas with the decreased temperature on the interphase can cause there thermocapillary convection, which can mix the liquid. Arising shear stress $\tau_{\rm sur}$,

$$\tau_{\rm sur} = \frac{\partial \sigma}{\partial T} \cdot \frac{\partial T}{\partial x} \tag{4}$$

removes liquid from more heated zones of liquid surface to less heated ones [e.g., see Nepomnyaschy et al. (2002) and Andreev et al. (2008)]. The assumption of the fact that coalescence of cluster droplets can initiate convective mixing of the layer was checked experimentally, Fig. 10. Liquid above the heater was mixed by a needle, briefly dipped into the layer. The intensity of this mechanical effect should exceed significantly the sequences of cluster coalescence. As a result of mechanical mixing of the layer, the temperature on the interphase decreases by $>6°$; however, the heat field restored during two seconds. It is important to note that temperature on the interphase restores after cluster destruction one order slower; this requires $\sim$20 s, Fig. 7.

Correlation between dependence $T_{S\,\max(t)}$ and formation of the droplet cluster, Fig. 7, proves a significant effect of the dissipative structure on liquid evaporation and heat and mass transfer in the gas medium near the interphase.

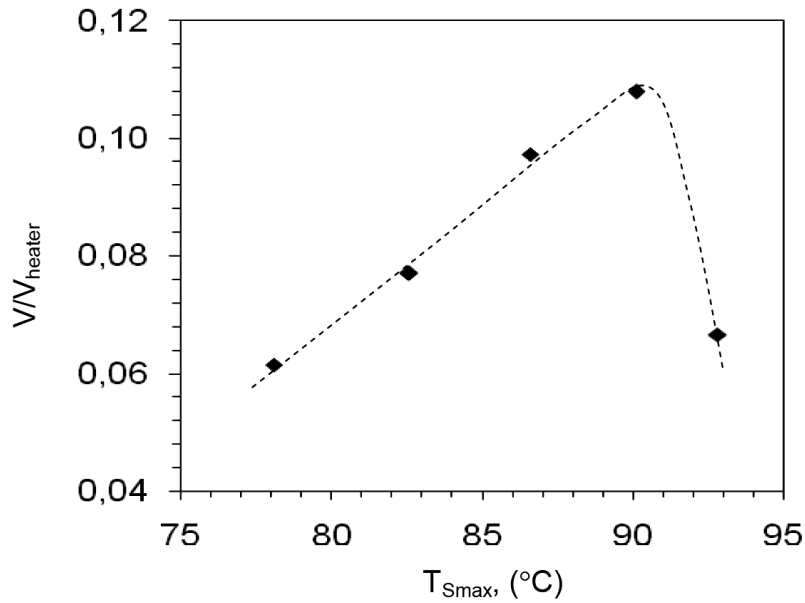

FIG. 9: Dependence of liquid volume injected into the layer at cluster coalescence on the interphase temperature, rated by the volume of liquid layer region with the area equal to the heater area ($V_{\mathrm{heater}} = \pi R^2_{\mathrm{heater}} h_0$).

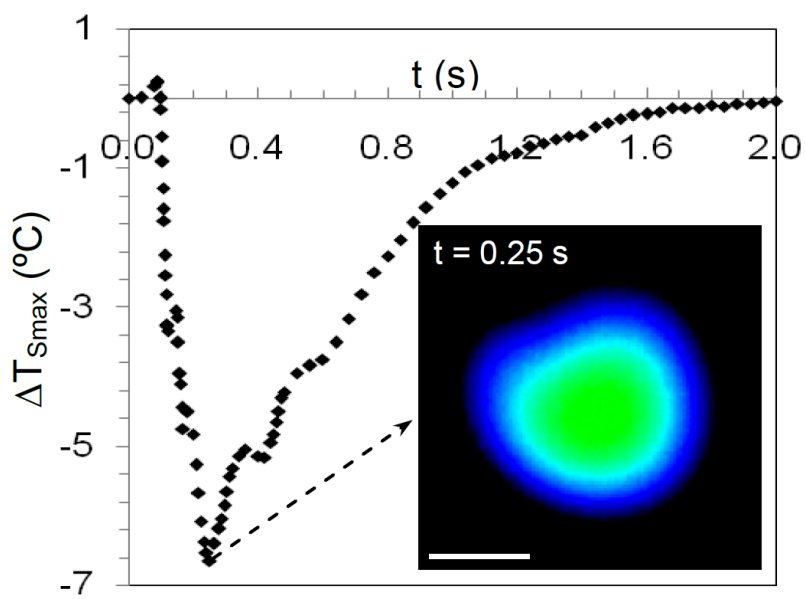

FIG. 10: Process of restoration of the heat field after mechanical mixing of the layer.

Perhaps a key role is played by the following features of the cluster: (i) active condensation growth of droplets increases the gradient of vapor concentration near the interphase, which intensifies layer evaporation; (ii) the evident temperature gradient on droplet surfaces makes probable development of thermocapillary flows in these droplets, which can effect the structure of the vapor-air jet above the heated region of the layer [see also Arinshtein and Fedorets (2010)]. Data obtained with the help of the thermal imager allow an estimate of the temperature gradient on the surface

of large droplets, Fig. 11. Points in distribution below the dashed line correspond to the regions of droplet surface (near its top), whose inclination toward the focal plane of the lens does not exceed 35 deg. The temperature in these regions is measured correctly, and it follows from distribution that the temperature gradient along the droplet surface is ∼30°/mm (1.4°/0.045 mm). The estimation of the temperature gradient in the gas phase over the heated zone of the liquid also gives very high values, up to 40 K/mm.

Under the conditions of experiment performed at $T_{S\,\max} \sim 90°$, the qualitative reconstruction of heat and mass transfer processes in the gas medium near the interphase occurs. The interdroplet distances increase significantly together with the mass of droplets, which can levitate above the interphase. With an increase in $T_{S\,\max}$ from 86.6° to 92.8°, a fourfold growth of droplet mass is observed at the moment of cluster coalescence, whereas the heater power increases by <1.5 times from 0.49 to 0.72 W. The effect of the droplet cluster on the layer temperature also changes principally. When $T_{S\,\max} < 90°$, cluster formation decrease the temperature on the interphase, which indicates intensification of evaporation or convective heat transfer between liquid and gas phase. This effect becomes more intensive with a rise of heater power, Fig. 8 (the positive temperature jump at coalescence of the droplet cluster). If $T_{S\,\max} > 90°$, we can observe the reverse tendency, and at $T_{S\,\max}$ = 92.8°, maximal within the studied range, the temperature on the interphase under the droplet cluster increases, which proves heat transfer deterioration. This issue requires further study, but the most likely cause of the slight deterioration of heat transfer is the conversion of steam-air flow around the drop cluster associated with the development of thermocapillary flow in large droplets (Arinshtein and Fedorets, 2010). These flows can generate around droplets' toroidal vortices that disimprove the outflow of hot gas from the surface layer.

5. CONCLUSION

Here, we present the results of experimental investigation of the mechanism of natural collapse of the spatially ordered structure, consisting of tens of microdroplets levitating parallel to the horizontal liquid-gas interphase at a distance comparable to the droplet diameter. These results were obtained via high-speed thermal imaging. It is found out that the reason for destruction of the whole "droplet cluster" can be coalescence of a single cluster droplet with the liquid

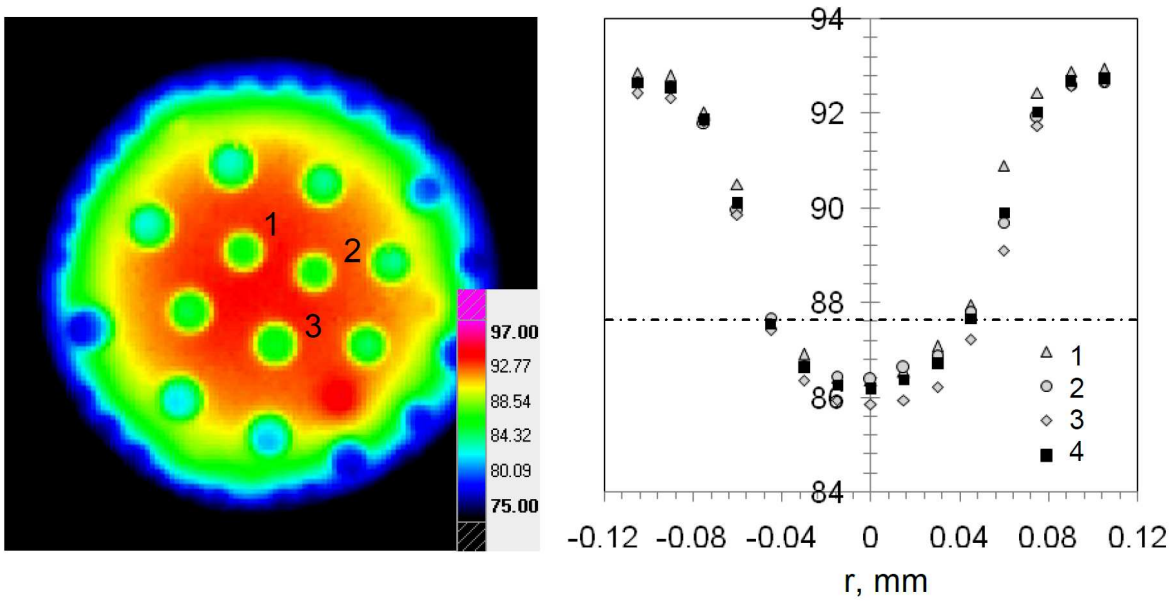

FIG. 11: Radial distribution of temperature over the surface of droplets with the diameter above 160 μm. Marker numbers 1–3 correspond to droplet numbers in the IR image of the cluster; marker 4 — distribution averaged by three droplets.

layer. Cluster coalescence occurs during 3 ms. Concentric symmetry of the wave of cluster destruction and velocity of destruction front of $\sim$70 cm/s prove that the process of cluster destruction relates to generation of the capillary wave on the interphase, caused by the fall of the first droplet. It is assumed that the amplitude of the capillary wave exceeds the height of droplet levitation H or is comparable to it.

It is determined that instantaneous coalescence of a cluster is accompanied by a temperature jump on the interphase; this jump equals tenths of a degree. With cluster restoration, the temperature of the layer surface returns gradually to the initial level. The period of temperature restoration is measured by tens of seconds. The interphase temperature under the droplet cluster can be both higher and lower than the interphase temperature without cluster, i.e., the cluster can both intensify and deteriorate heat and mass transfer between liquid and gas.

ACKNOWLEDGMENTS

The authors gratefully acknowledge support of this work by the Russian Ministry of Education Science (Contracts No. 14.740.11.0299 and No. 14.740.11.0641 and Agreement No 8511) and by the Russian Foundation for Basic Research (Project No. 12-08-01285-a).

REFERENCES

Andreev, V. K., Gaponenko, Yu. A., Goncharova, O. N., and Pukhnachov, V. V., *Modern Mathematical Models of Convection* (in Russian), Fizmatlit, Moscow, 2008.

Arinshtein, E. A. and Fedorets, A. A., Mechanism of energy dissipation in a droplet cluster, *JETP Lett.*, vol. **92**, no. 10, pp. 658–661, 2010.

Fedorets, A. A., Droplet cluster, *JETP Lett.*, vol. **79**, pp. 372–374, 2004.

Fedorets, A. A., On the mechanism of non-coalescence in a drop cluster, *JETP Lett.*, vol. **81**, no. 9, pp. 437–441, 2005.

Fedotets, A. A., Application of a droplet cluster to visualize microscale gas and liquid flows, *Fluid Dyn.*, vol. **43**, no. 6, pp. 923–926, 2008.

Fedorets, A. A., Marchuk, I. V., and Kabov, O. A., Role of vapor flow in the mechanism of levitation of a droplet cluster dissipative structure, *Tech. Phys. Lett.*, vol. **37**, no. 3, pp. 116–118, 2011.

Fedorets, . ., Heat and mass transfer effects under local heating of the gas-liquid interphase surface (in Russian), Doctoral thesis, Tyumen, 2011.

Fortov, V. E., Khrapak, A. G., Khrapak, S. A., Molotkov, V. I., and Petrov, O. F., Dusty plasmas, *Phys.-Uspekhi* (*Adv. Phys. Sci.*), vol. **47**, pp. 447–492, 2004.

Kabov O. A., Marchuk, I. V., and Chupin V. M., Thermal imaging study of the liquid film flowing on vertical surface with local heat source, *Russ. J Eng. Thermophys*, vol. **6**, no. 2, pp. 104–138, 1996.

Landau L. D. and Lifshitz E. M. *Fluid Mechanics, Course of Theoretical Physics*, vol. **6**, Pergamon Press, Oxford, 1987.

Mahajan, R., Chiu, C., and Chrysler, G., Cooling a microprocessor chip, *Proc. IEEE*, vol. **94**, no. 8, pp. 1476–1486, 2006.

Marchuk, I. V., Thermocapillary deformation of a thin locally heated horizontal liquid layer, *J. Eng. Thermophys.*, vol. **18**, no. 3, pp. 227—237, 2009.

Nepomnyaschy A. A., Velarde, M. G., and Colinet, P., *Interfacial Phenomena and Convection*, Chapman & Hall/CRC Press, London/Boca Raton, 2002.

Raist, P., *Introduction to Aerosol Science*, Macmillan, New York, 1984.

Thomas, H., Morfill, G. E., Demmel, V., Goree, J., Feuerbacher, B., and Möhlmann, D., Plasma crystal: Coulomb crystallization in a dusty plasma, *Phys. Rev. Lett.*, vol. **73**, 652–655, 1994.

Shavlov, A. V. and Dzhumandzhi, V. A., Spatially ordered structures in storm clouds and fogs, *Phys. Lett. A*, vol. **374**, pp. 2561–2565, 2010.

Shavlov, A. V., Dzhumandzhi, V. A., and Romanyuk, S. N., Electrical properties of water drops inside the dropwise cluster, *Phys. Lett. A*, vol. **376**, pp. 39–45, 2011.

Shavlov, A. V. and Dzhumandzhi, V. A., Geometrical parameters of water droplet cluster, *JETP Lett.*, vol. **141**, no. 2, pp. 288–291, 2012.

Schaefer, V. J., Observations of an early morning cup of coffee, *Am. Scientist)*, vol. **59**, pp. 534–535, 1971.

Zaitsev, D. V. and Kabov, O. A., An experimental modeling of gravity effect on rupture of a locally heated liquid film, *Microgravity Sci. Technol.*, vol. **XIX–3/4**, pp. 174–177, 2007.

Interfacial Phenomena and Heat Transfer, 1 (1): 63–80 (2013)

BOILING HEAT TRANSFER BY NUCLEATE BOILING OF IMMISCIBLE LIQUIDS

Shunsuke Onishi,* Haruhiko Ohta, Nobuo Ohtani, Yuta Fukuyama, & Hiroyuki Kobayashi

Department of Aeronautics and Astronautics, Kyushu University, 744 Motooka, Nishi-ku, Fukuoka, Japan, 819-0395

*Address all correspondence to Shunsuke Onishi, E-mail: shunsuke@aero.kyushu-u.ac.jp

Among the various methods to improve the heat transfer characteristics of nucleate boiling, the present research concentrates on the selection of coolant. Most of the existing research on nucleate boiling of binary mixtures clarified the heat transfer characteristics peculiar to the miscible mixtures, while the number of studies on immiscible mixtures is very limited. Pool boiling experiments on nucleate boiling of three immiscible mixtures, FC72/water, Novec649/water, and Novec7200/water, are performed in a closed vessel at 0.1 MPa. In the experiments, the thicknesses of stratified liquid layers for both component liquids on a horizontal heating surface before the heating are varied as one of the important parameters. When the layer thickness of the more volatile component with higher density is very small, e.g., 5 mm, a new phenomenon, "intermediate burnout," is observed. At heat flux higher than that of intermediate burnout, the surface temperature for the immiscible mixtures decreases from that for pure water, and simultaneously the critical heat flux (CHF) for the mixtures increases under the same pressure. The increase of CHF is mainly caused by the high subcooling of water, i.e., the less volatile component, resulting from the pressurization by the vapor of the more volatile component. The immiscible mixture has the potential to realize high performance heat exchange by the self-sustaining subcooling of component liquids even in closed systems.

KEY WORDS: *pool boiling, immiscible liquid, critical heat flux, subcooling, intermediate burnout*

1. INTRODUCTION

Because of the development of electronic technology, the heat generation density from semiconductors continues to increase. On the other hand, the electronic devices of Si semiconductors have a limitation of operating temperature. New semiconductors of SiC or GaN with higher thermal toughness are still under development, especially for those of large capacity. The cooling of large semiconductors such as power electronics with high heat generation density becomes an important subject to be investigated.

Liquid cooling utilizing the transportation of latent heat during nucleate boiling heat transfer has more advantages than the conventional cooling methods by air or by single-phase liquid. Because of the high heat transfer coefficient inherent in nucleate boiling, the cooling at high heat flux becomes possible minimizing the temperature difference between the surface and the coolant. Various methods have been attempted so far to increase critical heat flux (CHF). One of the present authors had developed a new structure of heating surface assembly to supply liquid to a large heating surface, where the heated length was substantially reduced (Shinmoto et al., 2009). The liquid is supplied from the transverse direction perpendicular to the main flow on the heating surface by the aid of auxiliary channels located at the side of or behind the main heated channel. This structure makes possible the liquid supply directly downstream of the heated channel without being interrupted by the accumulation of generated vapor. On the other hand, it is well known that CHF in subcool boiling assumes high values and the values can be further increased by microbubble emission boiling (MEB) under highly subcooled conditions (Suzuki et al., 2005). However, to keep the high subcooling of liquids practical, a flow boiling system is usually necessary to supply subcooled liquid steadily to

2169–2785/13/$35.00 © 2013 by Begell House, Inc.

NOMENCLATURE

c_p	isobaric specific heat (J/kg · K)
H	height (m)
h_{fg}	latent heat of vaporization (J/kg)
P	pressure (N/m^2)
q	heat flux (W/m^2)
q_{CHF}	critical heat flux (W/m^2)
R	gas constant (J/kg · K)
T	temperature (°C)
T_w	heating surface temperature (°C)
x	mole fraction of liquid (dimensionless)
y	mole fraction of vapor (dimensionless)

Greek Symbols

α	heat transfer coefficient (W/m^2 · K)
ΔT	temperature difference between the surface and liquid (K)
ρ	density (kg/m^3)

Subscripts

1	more volatile component
2	less volatile component
g	vapor
l	liquid
sat	saturation
sub	subcooled
b	boiling point or bulk liquid

the surface, and the two-phase flow loop requires many components. Another method is to use the miscible mixtures with a peculiar surface tension behavior. According to the experiments (Abe, 2005) using the mixture with the ”self-rewetting” action, the limit of heat transportation rate by heat pipes was drastically increased. This was expected to be caused by Marangoni force where the temperature gradient in addition to the concentration gradient along the liquid-vapor interface induced the liquid flowing towards the three-phase interline formed underneath boiling bubbles. Such a case is actually possible when the value of surface tension increases with temperature for the aqueous solutions of alcohol with higher carbon number in a certain concentration range (Vochten and Petre, 2005). For pool boiling, the increase in CHF was reported for heated wires (Van Stralen, 1956), while no marked increase was observed for a horizontal flat surface (Sakai et al., 2010). Sakai et al. tried to explain its reason by the difference of structure for the liquid supply between both configurations. There are other methods to increase CHF, e.g., the application of a finned surface to increase the substantial heat transfer area keeping the nominal area constant, and/or the change of surface nucleation characteristics. In the present paper, the possibility of immiscible liquid mixtures in nucleate boiling heat transfer is studied experimentally.

The cooling systems utilizing boiling heat transfer have an unavoidable disadvantage in addition to the advantage. Once incondensable gasses are mixed into the vapor, the condensation process is seriously interfered because the local vapor saturation temperature is decreased in the vicinity of condensation interface due to the local reduction of vapor partial pressure. To avoid the mixing of incondensable gases, it is desired to operate the cooling systems at higher than atmospheric pressure. However, at the same time, the elevation of operating pressure increases the saturation temperature, which implies the increase of the surface temperature to be cooled.

A large value of critical heat flux is expected for water compared to those for organic coolants. However, the saturation temperature for pure water is higher, in general, than the upper temperature limit for Si semiconductors, if the cooling system is operated at higher than atmospheric pressure. The application of immiscible liquid mixtures to the cooling systems can decrease the operating temperature of semiconductors, because the equilibrium liquid temperature is subcooled for both components under the total pressure given as the summation of partial pressures. By using immiscible mixtures in the systems, the volumetric ratio of the components accumulated on the heating surface plays an important role in the heat transfer. Under the gravitational conditions, immiscible liquids are separated to form the layers on the heating surface at least before the starting of heating, where the component with higher density directly contacts the heating surface. The thicknesses of the layers are related to the volumes of components enclosed in a vessel and the internal configuration of the vessel.

Transportation characteristics for two-phase flow of immiscible liquids are often discussed in the petroleum industry. Clark and Shapiro (1949) found the reduction of pressure gradient by the injection of water into an oil pipeline. Russell and Charles (1959) and Russel et al. (1959) clarified analytically the effects of volumetric flow rate and viscosity of immiscible liquids on the pressure gradient. Charles and Redberger (1962) found that the wave motion and the mixing at the oil-water interface promoted the reduction of pressure gradient and the predicted values were higher than the experimental ones. Yu and Sparrow (1969) clarified that the two-phase pressure drop for immiscible mixtures was insensitive to the shape of the interface. Tipman and Hodgson (1956) found that emulsions of oil and water had a higher pressure gradient than pure oils.

On the other hand, the flow of stratified immiscible liquids is an essential method for the production of a multilayer sheet or film by the coextrusion of different molten plastics, and for the production of bicomponent fibers by the spinning of solutions and melts. It is well known that the interface between immiscible liquids distorts in the flow. Southern and Ballman (1973, 1975) assumed that the interface behaviors were caused by the elasticity difference between the liquids, the preferential wetting of the tube wall by one of the liquids, and the viscosity difference between the liquids. They demonstrated the effects of elasticity and viscosity on the interface behaviors. Everage (1973) analytically simulated the viscosity effects and examined them experimentally. The extension of the analysis to the stratified liquid flow indicated that a low-viscosity liquid encapsulated a high-viscosity liquid and the distribution of liquids became annular in a tube (White and Lee, 1975). Minagawa and White (1975) verified the encapsulation throughexperiments using polyethylene and TiO_2-filled polyethylene. Hasson et al. (1970) and Hasson and Nir (1970) investigated the flow mechanisms of immiscible liquids with a small density difference, where the breakup of annular flow occured by either of two mechanisms — the collapse of the core liquid by strong Rayleigh waves, or the rupture of the liquid film contacting the top wall by the ascent of a lighter core liquid.

There is a very limited number of existing studies for the pool boiling of immiscible mixures. On the other hand, there exists a number of experimental and theoretical studies for nucleate boiling heat transfer using miscible binary mixtures, where the heat transfer coefficients are usually lower than those for the ”ideal” values evaluated by the interpolation directly of the heat transfer coefficients or of the surface superheats for the pure components at the same pressure. Or more precisely, the heat transfer coefficients are lower than the hypothetical single component with the same thermophysical properties as the relevant mixtures. Van Wijk et al. (1956) explained the mechanism for the lower heat transfer coefficient of binary mixtures. Stephan and Körner (1969) proposed a simple correlation to predict the heat transfer coefficient in nucleate boiling of miscible mixtures, which was followed by many modified predictive methods for the deteriorated heat transfer. The interfacial behaviors and heat transfer characteristics for immiscible liquid mixtures are, however, quite different from those for miscible mixtures, and the fundamental studies on the boiling phenomena peculiar to the immiscible liquids are needed.

Bragg and Westwater (1970) classified the boiling modes observed for different immiscible mixtures. Nucleate boiling of immiscible mixtures in a closed vessel was investigated also by Bonilla and Eisenberg (1948), where a jump of surface superheat was observed on the boiling curve of a water/styrene immiscible mixture at intermediate heat flux under a certain condition of volumetric ratio. The authors, however, did not pay attention to this trend. Sump and Westwater (1971) investigated the heat transfer due to film boiling, and clarified the enhanced heat transfer for an immiscible mixture of R113/water compared to that for pure R113. Mori (1978) observed bubble behaviors of six binary immiscible mixtures concentrating on the geometric shapes of the dispersed liquid around a single bubble rising in the continuous liquid phase, and classified them into four configurations by the relation of surface tensions for both liquids. Gorenflo et al. (2001) investigated nucleate boiling of water/1-butanol on a horizontal tube. The mixture becomes miscible or partially miscible depending on the concentration, temperature, and pressure. Based on the experiments varying concentration and pressure, they reported the weak dependence of miscibility on the nucleate boiling heat transfer.

Experiments were conducted also for the mixture of emulsions. Filipczak et al. (2011) studied nucleate boiling of water-oil mixtures. They showed in detail the distribution of oil, water, and vapor for different heat flux levels. The heat transfer coefficients for water-oil mixtures with high oil concentration were far smaller than those for nucleate boiling of pure water because of the contribution by free convection. They reported the transition of the heat transfer coefficient by the foaming at the initial stage of nucleate boiling and by the subsequent formation of emulsion. Roesle and Kulacki (2012) studied nucleate boiling of two dilute emulsions, FC72/water and pentane/water, where

the concentration of the more volatile dispersed component FC72 or pentane was varied by 0.2%–1.0% and 0.5%–2.0%, respectively. The heat transfer data were obtained by using a horizontal wire. They reported two boiling modes, i.e., boiling of the dispersed component and boiling of dispersed and continuous components, depending on the heat flux level. For the volume fraction of the dispersed component larger than 1%, the heat transfer enhancement due to the boiling of the dispersed component was reported. Bulanov and Gasanov (2006) investigated nucleate boiling of four emulsions, n-pentane/glycerine, diethyl ether/water, R113/water, and water/oil, where more volatile components were dispersed in the continuous less volatile components. They reported the reduction of surface superheat at the boiling incipience for the emulsions compared to those for the pure liquids of the continuous component. For water/oil emulsions, the surface superheat at the boiling incipience became smaller for smaller droplets of dispersed component.

The existing experimental data for boiling of immiscible mixtures are still fragmentary. Because of the limited number of studies, no coherent trend or conclusion is derived. The objective of the present investigation is to clarify the boiling heat transfer to immiscible liquids, and to discuss the unusual trends not clarified in the past.

2. EXPERIMENTAL APPARATUS AND PROCEDURE

The experimental apparatus is composed of a boiling vessel, condensers, and a heating block assembly as shown in Fig. 1. The boiling vessel is made from a stainless steel cylinder with an inner diameter of 200 mm and a height of 410 mm. Liquid and vapor temperatures are measured by four thermocouples located in the vessel. The condensers, hung from the top flange of the boiling vessel, regulate the liquid equilibrium temperature and then the total pressure. The upper edge of the cylindrical copper block is operated as the heating surface, and is heated by the cartridge heaters inserted in the bottom of the block. Eight thermocouples are inserted in the block at a depth of 1, 7, 13, and 19 mm from the surface along two axes at the center and at the 14 mm distance from the center. Sheathed thermocouples are employed. The outer diameters are 1 mm for the measurement of temperature distribution in the heating block, and 3 mm for the measurement of liquid and vapor temperatures.

The heating surface, a horizontal circular area with a diameter of 40 mm, is facing upwards, which is polished with sandpaper (No. 600) to keep the same nucleation characteristics for all experimental runs. The heating surface is

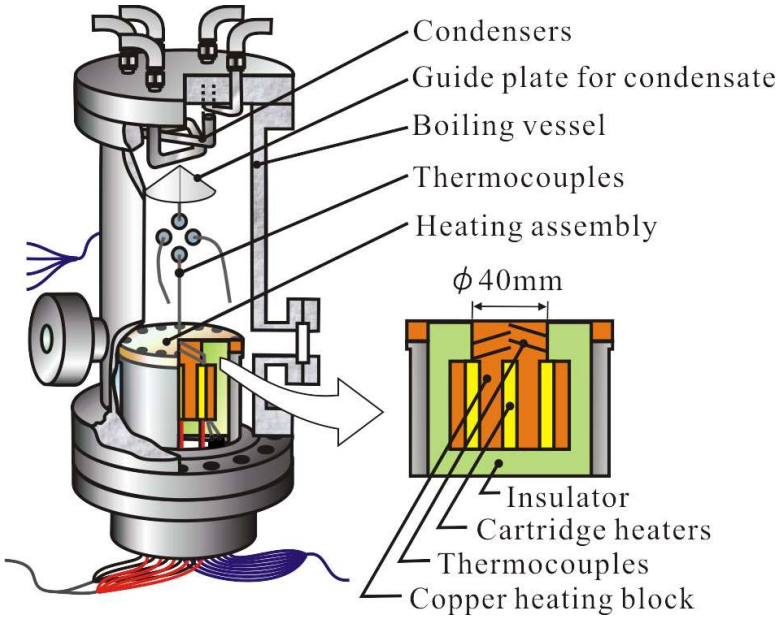

FIG. 1: Experimental apparatus.

surrounded by a circular thin fin cut out in one unit body to prevent the preferential bubble generation at the edge of the heating surface, and to minimize the heat loss from the periphery of the heating block.

Experiments are conducted under pool boiling conditions. After the enough time has elapsed to confirm the steady state of indicated temperatures by all thermocouples and of the total pressure, the data are acquired. The condition of critical heat flux is detected by the excursion of temperatures in the copper heating block. The heat flux, one step before the value of the resulting temperature excursion, is regarded as the critical heat flux in this experiment. The heat flux near CHF is increased in steps by an increment 10% of the previous value, which determines the resolution or the accuracy of the CHF measurement.

The uncertainties in surface temperature evaluated by the extrapolation of temperatures in the heating block are 0.075 and 0.525 K at heat fluxes 10^5 and 10^6 W/m^2, respectively, which resulted from the error of 0.025 K for the temperature measurement by thermocouples and the error of 0.2 mm for the thermocouple locations in the heating block. The corresponding uncertainties of temperature difference between the heating surface and bulk liquid are 0.10 and 0.55 K, which causes the error of 1.0% and 1.4% for the measured temperature differences of 10 and 40 K, respectively, for the relevant heat fluxes. The errors of heat flux evaluated by the gradient of thermocouples are 3360 and 23-500 W/m^2, reflecting the uncertainties for the temperature measurement and thermocouple locations, which results in 3.4% and 2.4% for the relevant heat fluxes. As a consequence, the errors of heat transfer coefficient are 4.4% and 3.8% at heat fluxes 10^5 and 10^6 W/m^2, respectively.

For a selected mixture, experiments are performed at 0.1 MPa and corresponding constant equilibrium temperature independent of the volume ratio of the components. Table 1 shows the selected components for the mixtures tested. Water is used for all mixtures as a less volatile component with lower density. Any one of three components, FC72, Novec649, and Novec7200, as a more volatile component with higher density, is combined with water. As a result, FC72/water, Novec649/water, and Novec7200/water are selected as the immiscible liquid mixtures. FC72, Novec649 and Novec7200 have zero values of ODP (ozone depletion potential) and both of the Novecs have a smaller GWP (global warming potential) than FC72.

Figure 2 shows an image for liquid layers of immiscible liquid mixtures before heating, where H_1 is the thickness of the more volatile component with higher density and H_2 is the thickness of the less volatile component with lower density. The combination of layer thicknesses is varied as one of the major parameters keeping the total thickness constant, where the value of H_1 plays an important role on the heat transfer characteristics. Once nucleate boiling is initiated, the liquid-liquid interface cannot be kept smooth but the complex physical mixing of immiscible liquids occurs. For all selected combinations of component liquids, the density of the more volatile component is higher than that of the less volatile component. If the situation is reversed, i.e., the density of the more volatile component is lower than that of the less volatile component, boiling is started in the layer of the less volatile component. Increase of the CHF value is expected by high subcooling of the less volatile liquid under the pressurization by the vapor of the more volatile component. If burnout occurs and the more volatile component can start to contact the heating surface under the conditions of the small layer of the less volatile component, the burnout cannot be suppressed. CHF values for

TABLE 1: Thermal properties of components at 0.1 MPa

Test fluid	**Normal boiling point** T_{sat} **(°C)**	**Liquid density** ρ_l **(kg/m^3)**	**Vapor density** ρ_g **(kg/m^3)**	**Latent heat of vaporization** h_{fg} **(kJ/kg)**	**Thermal conductivity** k_l **(mW/mK)**	**Liquid viscosity** μ_l **(mPa · s)**	**Isobaric specific heat** c_{pl} **(kJ/kg · K)**	**Surface tension** σ **(mN/m)**
Water[a]	100	958	0.60	2257	680	0.28	4.22	58.9
FC72[b]	55.9	1605	13.3	95.7	54.1	0.44	1.10	7.90
Novec649[b]	49.2	1531	12.7	88.6	54.2	0.45	1.12	9.20
Novec7200[b]	78.4	1307	9.47	113.4	58.2	0.33	1.33	9.18

[a]Incropera and DeWitt (2002)
[b]Sumitomo 3M Limited, personal communication

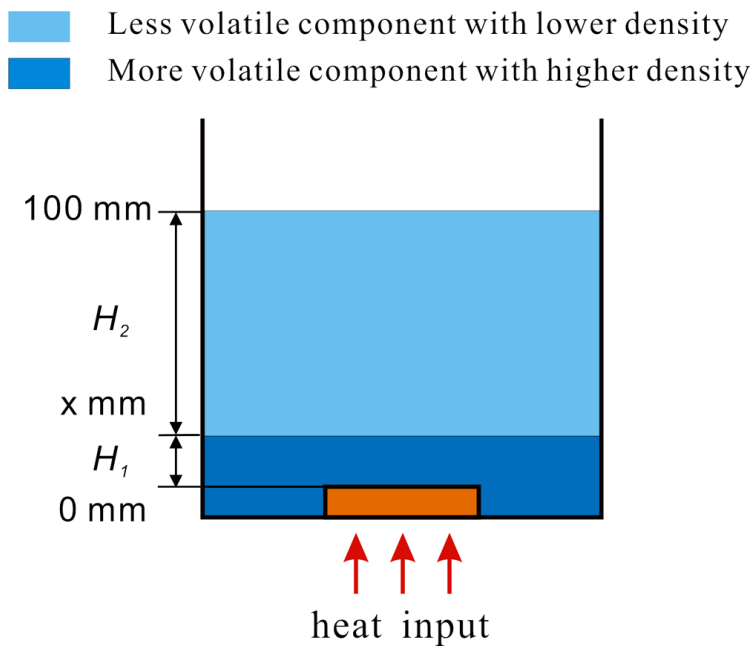

FIG. 2: Image of liquid-liquid interface with different thickness in nucleate boiling of immiscible mixtures on the horizontal heating surface.

more volatile components, in general, are smaller than that for the less volatile component, and this situation cannot be improved at all by the small subcooling of the more volatile component.

The stable transition of heating surface temperature at the boiling incipience is an altenative advantage to use a more volatile component with higher density. This is a very important requirement for the cooling of, e.g., inverters of the electric automobile, where the thermal load is varied drastically. Nucleate boiling starts at a small surface superheat in the layer of the more volatile liquid and only a small overshoot of surface temperature is observed under the conditions of small subcooling under the low partial vapor pressure of the less volatile component. If the less volatile component, e.g., water, has accumulated directly on the heating surface, boiling never initiated before the heating surface temperature exceeds 100°C at 0.1 MPa. A large hysteresis of surface temperature is expected for the large subcooling of water pressurized by a high vapor partial pressure of the more volatile component. A surface temperature larger than 100°C does not meet the requirement for the cooling of most of the existing small semiconductors. The more volatile component should be selected so that it has a higher density than that of the less volatile component, and it suppresses the overshoot of surface temperature at the boiling incipience. Actually, the equilibrium temperature of the mixture FC72/water is 51.6°C under the total pressure of 0.1 MPa, where only subcooled boiling is possible in the immiscible mixture system.

The boiling behavior for very small thickness H_1 of the more volatile component layer is expected to be quite different from that for a liquid pool of the relevant component because the liquid layer on the heating surface is easily consumed by the evaporation. In the experiment, the thicknesses of liquid layers H_1 and H_2 for more and less volatile components, respectively, are varied keeping the total thickness of 100 mm from the heating surface unchanged. The ratio H_1/H_2 is varied as 0 mm/100 mm, 5 mm/95 mm, and 10 mm/90 mm. In the upper part of the boiling vessel, a guide plate is installed for the condensate to return to the heating surface from the periphery.

3. PHASE EQUILIBRIUM DIAGRAM

Figure 3 shows the phase equilibrium diagram at the total preasure of 0.1 MPa for the immiscible liquid mixtures, FC72/water, Novec649/water, and Novec7200/water, respectively. The bubble point curve is represented by a solid

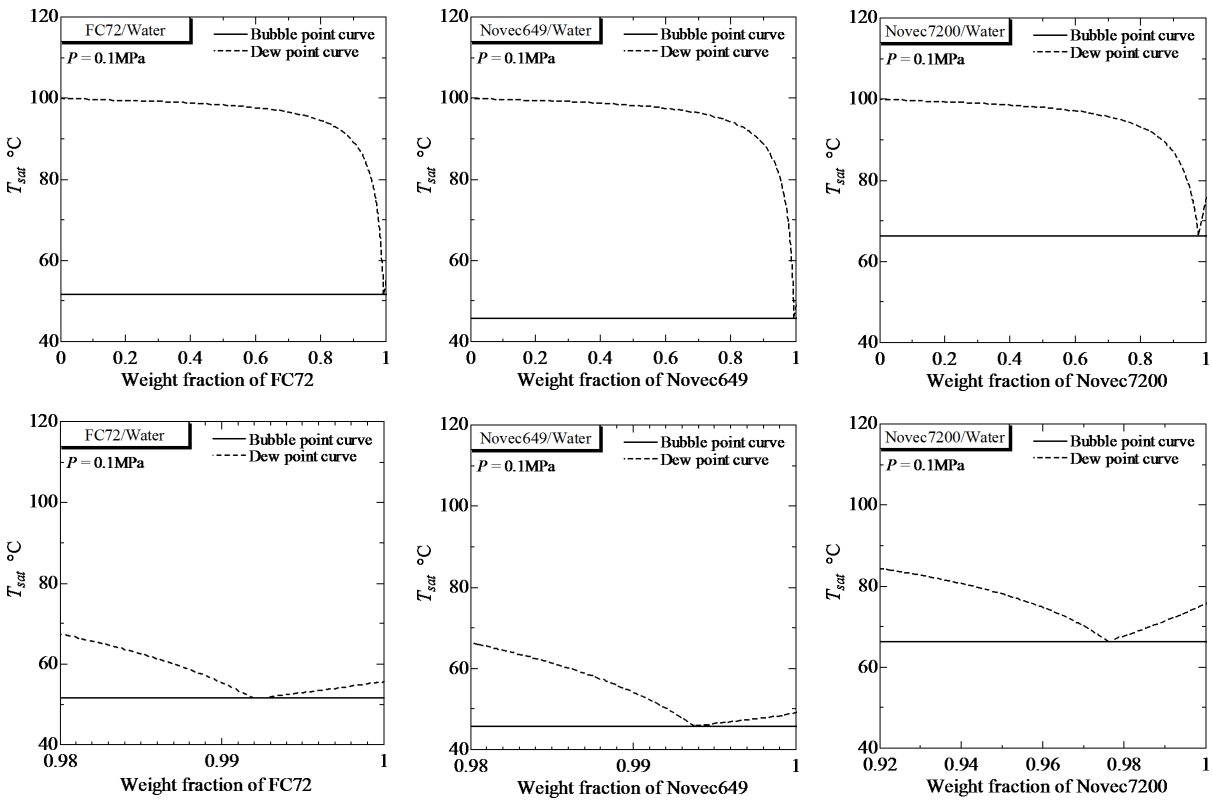

(a) FC72/Water (b) Novec649/Water (c) Novec7200/Water

FIG. 3: Phase equilibrium diagram for immiscible mixture at 0.1 MPa.

line, below which the mixture is in the liquid state. On the other hand, the mixture is in the vapor state above the dew point curve represented by broken lines. The point where the two curves merge, i.e., the point similar to the azeotropic point existing in a part of the miscible mixtures, is observed for all of the immiscible mixtures tested here at the concentration near the pure, more volatile component.

The dew point curve is calculated from the following equations (Prigogine and Dfay, 1954):

$$\ln y_1 = -\frac{h_{fg,1}}{R_1}\left(\frac{1}{T} - \frac{1}{T_{b,1}}\right) \tag{1}$$

$$\ln y_2 = -\frac{h_{fg,2}}{R_2}\left(\frac{1}{T} - \frac{1}{T_{b,2}}\right) \tag{2}$$

where, y is the mole fraction of vapor, h_{fg} is the latent heat of vaporization (kJ/kg), and R is the gas constant (kJ/kg · K). The equilibrium temperatures and subcooling of each component under the total pressure of 0.1 MPa are shown in Table 2 for three mixtures.

4. OBSERVATION OF INTERFACIAL AND BUBBLE BEHAVIORS

Figure 4 shows the interfacial and bubble behaviors of FC72/water mixtures for the thicknesses of the more volatile liquid H_1 = 50, 5 and 0 mm in addition to those for pure water at different heat fluxes. The behaviors for pure FC72 are almost the same as those for H_1 = 50 mm because its subcooling is very low as indicated in Table 2. At heat fluxes larger than 4×10^5 W/m^2 burnout occurs for H_1 = 50 mm.

TABLE 2: Equilibrium temperature and subcooling of component liquids at 0.1 MPa

	T_b (°C)[a]	$\Delta T_{\mathrm{sub},1}$ (K)	$\Delta T_{\mathrm{sub},2}$ (K)
1 : FC72 2 : water	51.6	4.3	48.4
1 : Novec649 2 : water	45.9	3.3	54.1
1 : Novec7200 2 : water	66.4	12.0	33.6

[a] Sumitomo 3M Limited, personal communication

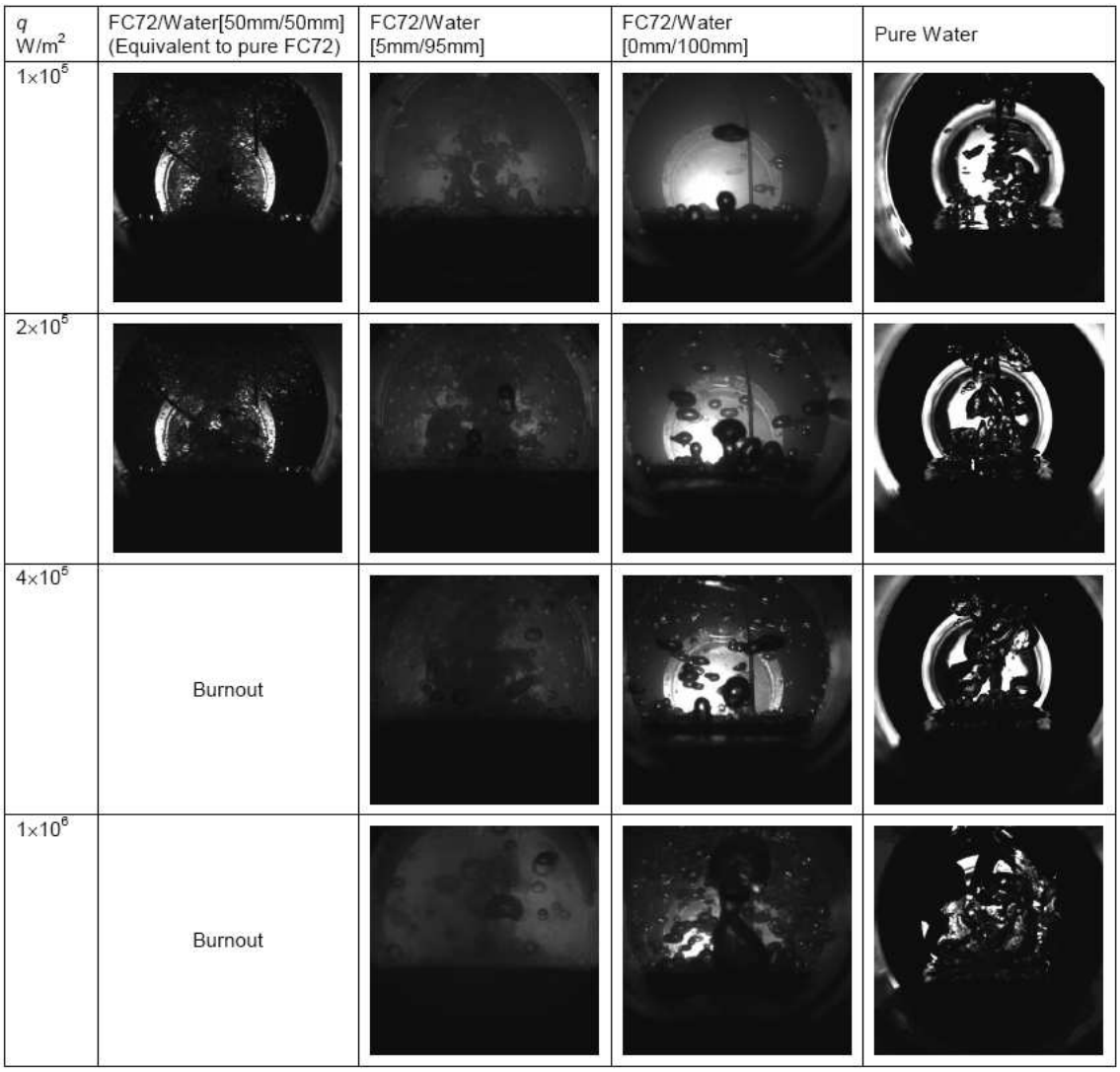

FIG. 4: Interfacial and bubble behaviors for different layer thicknesses of more volatile liquid and heat flux levels.

For H_1 = 0 mm, after free convection of the less volatile liquid occurs on the heating surface, a large disturbance is observed at the boundary of the more and less volatile liquids around the cylindrical heating block A part of the more volatile liquid is conveyed to the heating surface and evaporated. The bubbles of FC72 are much larger than

those for pure FC72. Their penetration into the water across the boundary of both liquids is interrupted before the bubble volume and then the buoyancy becomes larger by the lateral coalescence. It is clear from the pictures that the FC72 liquid is also lifted by the bubbles departing from the heating surface. After the bubbles surrounded by the FC72 liquid have reached the water surface, they collapse and only FC72 liquid droplets fall on the heating surface by the gravitational force. At low heat flux, the free convection of water plays an important role for the heat transfer. At higher heat flux, the amount of FC72 liquid conveyed to the heating surface is increased generating a larger number of bubbles. At high heat flux, the generation of water bubbles with a concentration of FC72 vapor is observed at the center of the heating surface, where the subcooling of the water pool is decreased by the free convection and by the release of latent heat from the bubbles composed partly of water vapor. In addition, the amount of vapor of FC72 is also increased by the reduction of subcooling at the center. On the other hand, no water bubble is recognized at the peripheral part of the heating surface owing to the quick condensation under the large subcooling for water still maintained in this location.

For H_1 = 5 mm, boiling of FC72 becomes a dominant heat transfer mode even at low heat flux and the contribution of free convection of water is reduced. As a consequence, the boundary of both liquid layers becomes unclear and fine FC72 bubbles similar to those for pure FC72 or for H_1 = 50 mm can penetrate into the water pool of low subcooling for FC72. The transparency of liquid is decreased for H_1 = 5 mm, because fine FC72 droplets are suspended in water like an emulsion. It is noteworthy that a large coalesced bubble is not observed at the center even under the highest heat flux condition for H_1 = 5 mm. Boiling of FC72 which occurs preferentially becomes more important for the heat trnafer compared to that of water in this case, and FC72 bubbles rise in the water pool with little reduction of their volume by the condensation. As a result, the water pool is maintained at high subcooling even at the high heat flux, and generated water bubbles immediately condense on the heating surface without their detachment. For H_1 = 10 mm, the interfacial behaviors are similar to those for H_1 = 5 mm, but burnout occurs at lower heat flux 3.5×10^5 W/m^2. Trends similar to those described above were also observed for Novec649/water and Novec7200/water mixtures.

5. HEAT TRANSFER CHARACTERISTICS

Figures 5–7 show the heat transfer data for immiscible liquid mixtures FC72/water, Novec649/ water, and Novec7200/ water. Each figure also includes the data for a pure, more volatile component and a pure, less volatile component, i.e., water. The levels for measured CHF values are also represented by dotted lines. In some cases, CHF cannot be observed even at the upper limit of supplied heat flux which is determined by the limitation of operating temperature for the heaters inserted in the heating block. Because the experimental results for three immiscible mixtures have similar tendencies, the results for FC72/water are discussed below in detail.

5.1 Boiling Curve

Figure 5(a) shows the boiling curves for FC72/water and pure components, where the temperature differences are ΔT_b defined by using the equilibrium temperature for the mixture and ΔT_{sat} by surface superheat for pure components. In the case of small thickness for the FC72 layer, i.e., FC72/water, 10 mm/90 mm and 5 mm/95 mm, the local burnout and the small temperature excursion occur at the heat flux of around 2×10^5 W/m^2 which is lower than CHF for pure FC72 at 0.1 MPa. The lower burnout heat flux at the same pressure is curious because FC72 is subcooled for the mixture by the vapor pressure of water (P_1 = 0.088 MPa, T_b = 51.6°C, $\Delta T_{\mathrm{sub},1}$ = 4.3 K, P = 0.1 MPa). The reduction of CHF seems to be caused by the insufficient supply of FC72 for such a small initial layer thicknesses.

The evaporation of FC72 from its small inventory and the extension of local dry patches induce the burnout at lower heat flux. The area of dry patches underneath a coalesced bubble is extended by its growth, resulting in the increase in the surface temperature. When the diameter of a bubble exceeds a certain value characterized, for example, by the wavelength of Taylor instability, it becomes easier for water to contact the heating surface directly. In the usual burnout for pure FC72, the liquid contacting the surface is immediately evaporated keeping the vapor film on the heating surface without its collapse. On the other hand, if the surface temperature is far below the saturation temperature of liquid, the surface begins to be quenched by the natural convection of the liquid. As a result, after the increase of the temperature difference by around 20 K, the large dry patches causing the temperature excursion

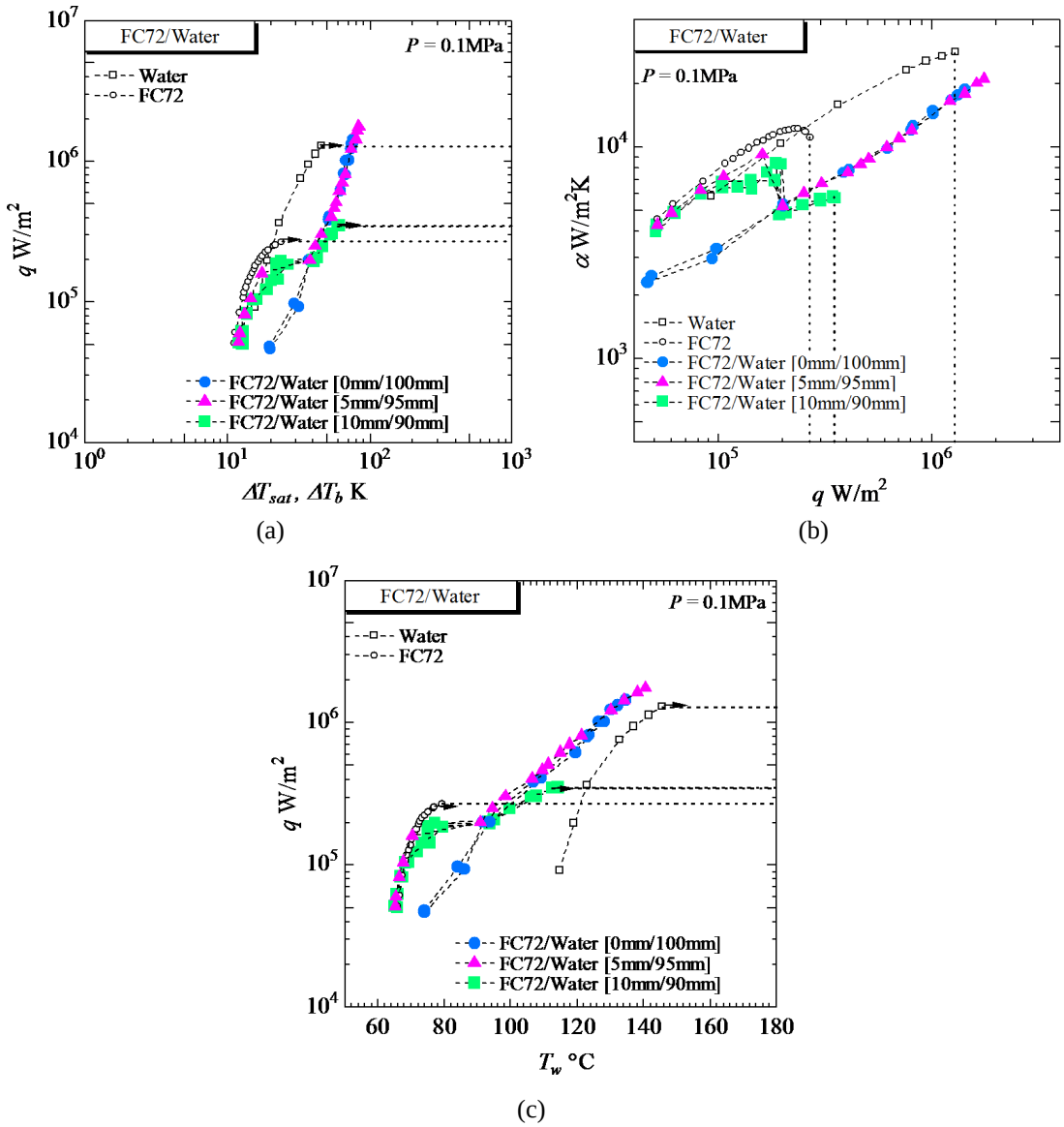

FIG. 5: Heat transfer characteristics for FC72/water.

disappear followed by the stable heat transfer. The curve for the FC72/water mixture becomes similar to that for pure water by the further increase of heat flux. The small temperature excursion at the moderate heat flux is one of the important phenomena inherent in nucleate boiling of immiscible mixtures with a small layer thickness of more volatile liquid. The phenomenon is named “intermediate burnout” in the present study.

The reduction of the temperature jump or the gradual change of surface temperature due to the intermediate burnout is desired for practical applications. The mixing of component liquids seems to be a key to determine such a transition of surface temperature. In the case of high velocity of a more volatile vapor and low density of a less volatile liquid, the physical mixing becomes more difficult, resulting in a distinct jump of surface temperature. On the other hand, with low velocity of a more volatile vapor and high density of a less volatile liquid, the physical mixing is easier and the surface temperature increases gradually. The mixing is also possible chemically by the solubility of components which becomes enhanced at higher equilibrium temperature.

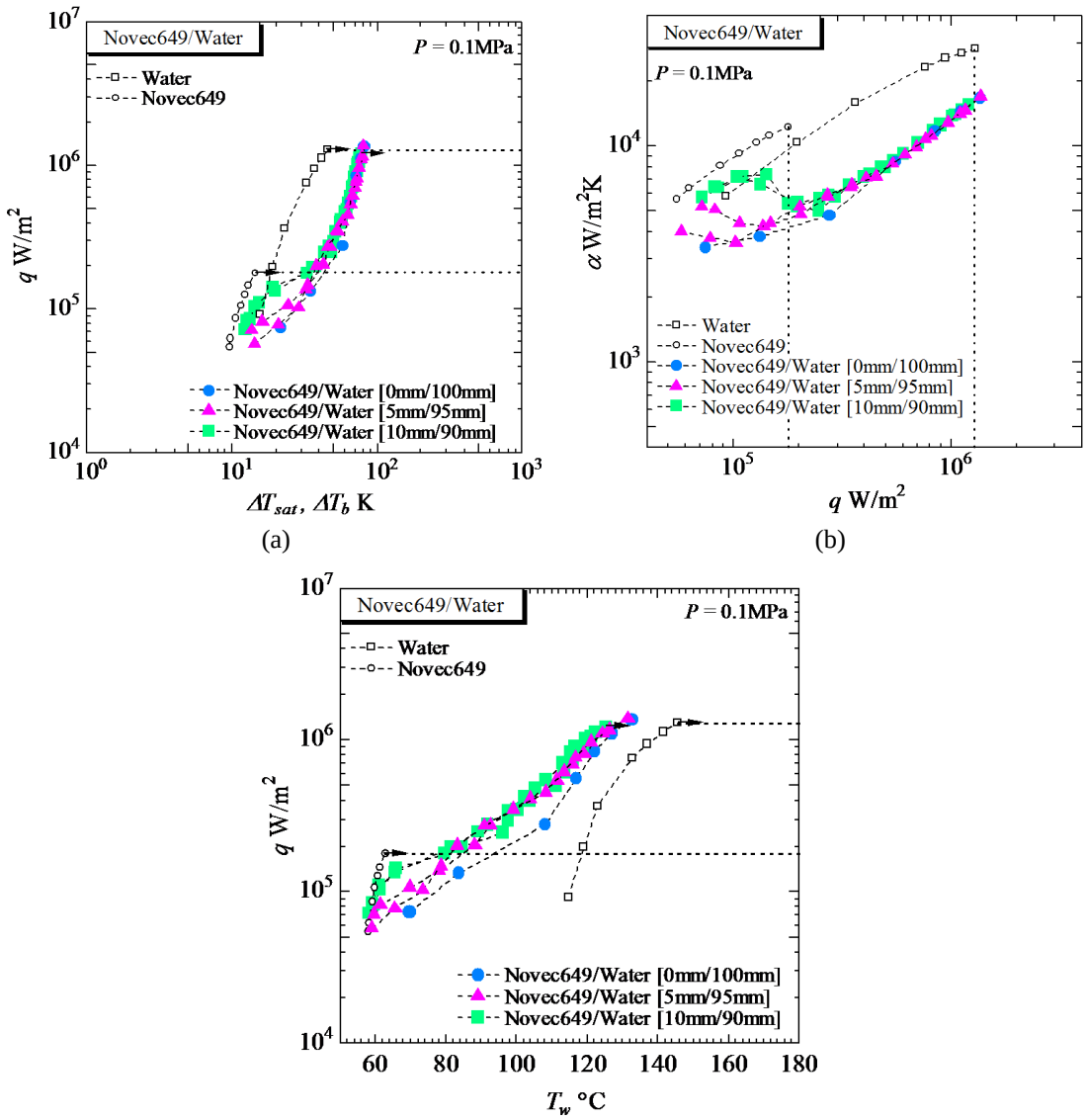

FIG. 6: Heat transfer characteristics for Novec649/water.

On the other hand, for a large thickness of FC72 (not shown), the heat transfer characteristics are almost the same as those for pure FC72 because of small subcooling as shown in Table 2. The result indicates the existence of a boundary of layer thickness for FC72, where the heat transfer characteristic for immiscible mixtures changes from those for pure FC72. The curves for the mixtures (10 mm/90 mm and 5 mm/95 mm) are shifted towards the right after the intermediate burnout keeping gradients similar to that for pure water. These curves coincide with that for FC72/water, 0 mm/100 mm, in which no layer of FC72 contacts the heating surface and the side wall of the cylindrical heating block is exposed to FC72 at least before the heating.

Figures 6(a) and 7(a) show boiling curves for Novec649/ water and Novec7200/water, respectively. For Novec649/ water (10 mm/90 mm and 5 mm/95 mm), no clear intermediate burnout is observed, but the curves shifted to that for 0 mm/90 mm at low heat flux. The trend, caused by the mixing of water with Novec649, is more emphasized

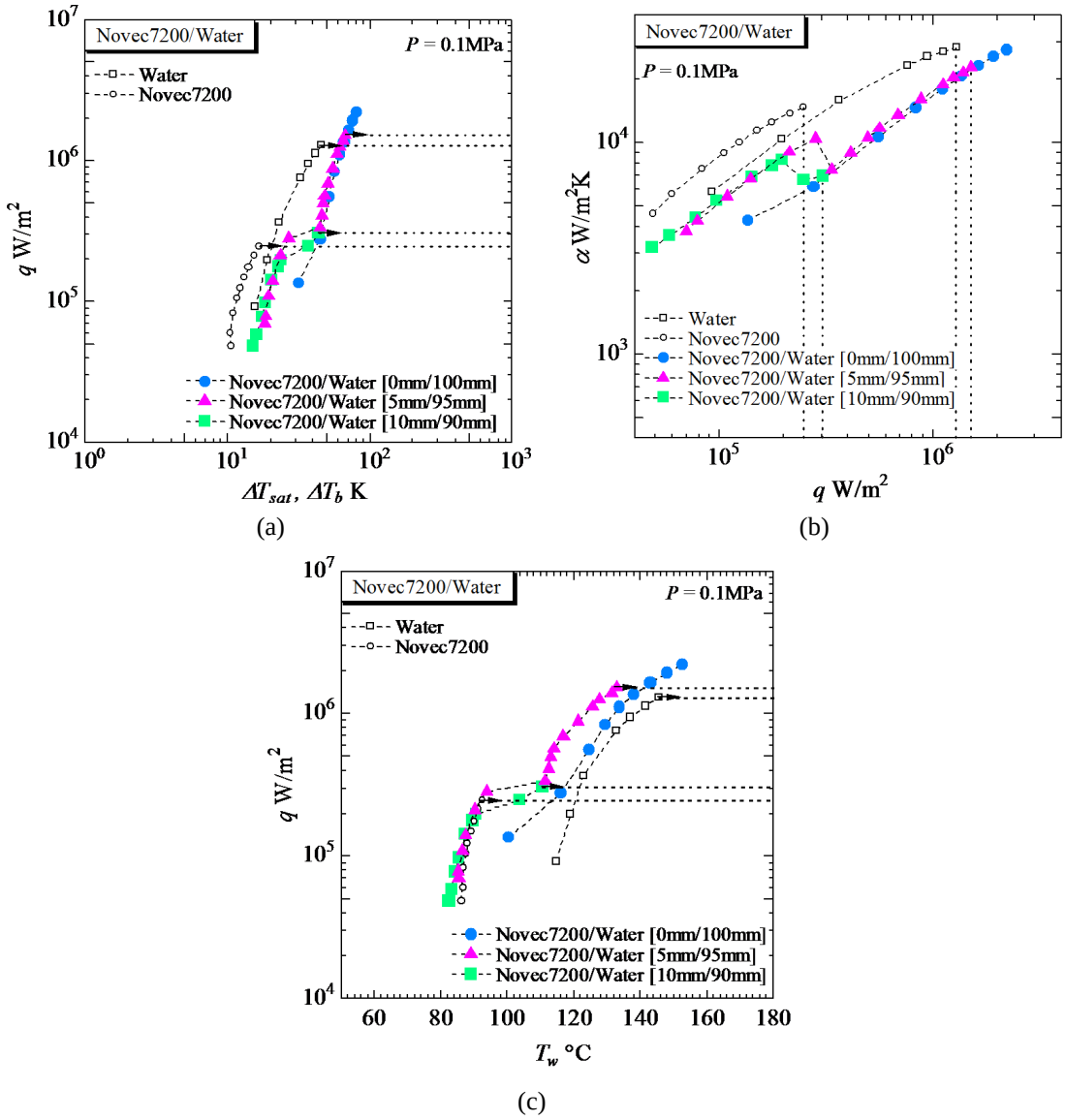

FIG. 7: Heat transfer characteristics for Novec7200/water.

for 5 mm/95 mm, where the influence of the more volatile liquid layer is smaller. The curves for the mixtures with different layer thicknesses coincide well with that for 0 mm/100 mm.

For Novec7200/water (10 mm/90 mm and 5 mm/95 mm), the clear intermediate burnout is observed again. The heat flux of intermediate burnout for 10 mm/90 mm is lower to some extent than that for pure Novec7200, while the transition heat flux for 5 mm/95 mm is higher and the temperature difference jumps more distinctively. Also in this case, the curves for the mixtures after the intermediate burnout coincide well with the curve for 0 mm/100 mm.

5.2 Heat Transfer Coefficient and Surface Temperature

Figure 5(b) shows heat transfer coefficients for FC72/water plotted against heat fluxes. The heat transfer coefficient after the intermediate burnout is clearly lower than that for pure components except the case of large H_1 (not shown)

which is almost equivalent to pure FC72 as mentioned before. For mixtures the heat transfer coefficient is defined by using the measured liquid temperature which is near the equilibrium temperature shown in Table 2 and is independent of the volumetric ratio at the constant total pressure of 0.1 MPa. At low heat flux before the occurrence of the intermediate burnout, the deteriorated heat transfer from that for pure FC72 is caused by the non-negligible contribution of natural convection by water flowing in the heating surface. The situation is essentially different from the case of miscible mixtures, where the deterioration is caused mainly by the diffusion resistance. At high heat flux beyond the intermediate burnout, the heat transfer deterioration is again observed. This is caused mainly by the definition of the heat transfer coefficient by using the subcooled temperature at around 52°C measured for mixtures instead of around 100°C for pure water at the same (total) pressure of 0.1 MPa. Heat transfer is dominated by boiling of water at least for the surface temperature far above 100°C. In Fig. 5(c), a large decrease of surface temperatures T_w for the mixtures is clearly observed after the intermediate burnout despite superficial heat transfer deterioration. It is noteworthy that such reduction of heating surface temperature is also observed for 0 mm/100 mm. If surface temperature is insensitive to the degree of subcooling, heat transfer due to nucleate boiling is enhanced rather than deteriorated as indicated by the heat transfer coefficients in Fig. 5(b). The enhancement of heat transfer is possible when bubbles or vapor columns of the more volatile component enhance the evaporation of the less volatile liquid.

Figures 6(b) and 7(b) show heat transfer coefficients for Novec649/water and Novec7200/water, respectively. For Novec649/water, the heat transfer coefficient starts to decrease from that for pure Novec649 at low heat flux. Boiling of Novec649 is gradually replaced by the natural convection of water. The heat transfer coefficients at higher heat flux coincide well with that for 0 mm/90 mm. This is true also for Novec7200/water, where the distinct intermediate burnout is observed.

Figures 6(c) and 7(c) show heating surface temperatures for Novec649/water and Novec7200/water, respectively. Reduction of surface temperature from that for pure water is clear. The degree of reduction for Novec7200/water, 0 mm/100 mm is smaller than that for 5 mm/95 mm.

5.3 Critical Heat Flux

In Figs. 5–7, the levels of critical heat flux are represented by the horizontal or vertical dotted lines. As mentioned before, the actual CHF value accompanied by the serious temperature excursion was not measured for FC72/water (5 mm/95 mm) because of the limitation in the operating temperature of cartridge heaters. However, the result shows that the CHF value is at least 36% higher than that of pure water. Ivey and Morris (1966) proposed the following correlation:

$$\frac{q_{\mathrm{CHF,sub}}}{q_{\mathrm{CHF,sat}}} = 1 + 0.1\left(\frac{\rho_g}{\rho_l}\right)^{1/4} \frac{c_{pl}\rho_l \Delta T_{\mathrm{sub}}}{\Delta h_{fg}\rho_g} \tag{3}$$

The values of CHF estimated by this correlation are as much as 4.3×10^6 W/m^2 for pure subcooled water, where the liquid subcooling of 48.4 K corresponding to the equilibrium temperature 51.6°C for FC72/water at 0.1 MPa is substituted into Eq. (3) and the CHF for the saturated condition is given by the experimental value. A similar increase of the CHF value is expected for FC72/water with small H_1 such as 5 mm. On the other hand, the experimental result shows that the CHF for FC72/water (10 mm/90 mm) is much lower than that of pure water. This difference in the trend of CHF can never be reproduced by the variation of thermophysical properties averaged by using, for example, volumetric ratios. For 10 mm/90 mm, even after the occurrence of intermediate burnout, boiling of the FC72 and water mixture continues because the evaporation of the FC72 layer is not enough. The layer of FC72 becomes a barrier for the subcooled water to make enough contact with the heating surface.

The similar trend is observed for Novec7200/water (10 mm/90 mm), while CHF value of Novec7200/water (10 mm/90 mm) is quite large and is almost the same as that for pure water.

6. SUMMARY OF NUCLEATE BOILING OF IMMISCIBLE LIQUID MIXTURES

In Fig. 8, the data of immiscible liquid mixtures for H_1 = 5 mm are summarized. In almost all of the existing studies, the surface superheat ΔT_{sat} is used as an abscissa of the boiling curve (Nukiyama, 1934). To study the boiling of

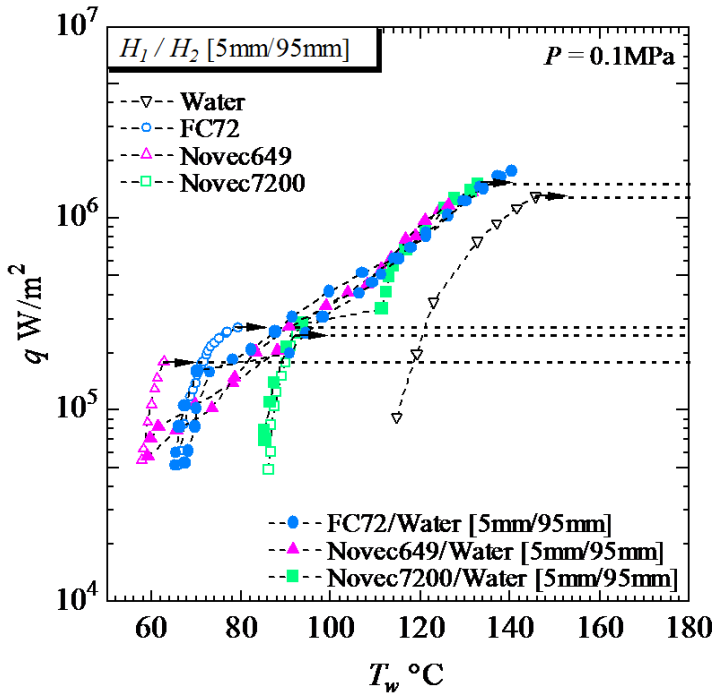

FIG. 8: Summary of nucleate boiling characteristics for three immiscible mixtures (H_1/H_2) = (5 mm/95 mm) with thin layer of more volatile component.

immiscible binary mixtures for the application to the cooling of semiconductors, the plot of heat flux versus the surface temperature T_w is more useful.

The agreement of heat transfer characteristics at high heat flux, which is almost independent of the selection of the more volatile component, implies that the thermal properties of water have a dominant role in the heat transfer. The obvious reduction of surface temperature is caused by the enhanced evaporation of water by the aid of bubbles or vapor slugs of the more volatile component. Then, the enhancement seems to be related to the evaporated vapor volume of the more volatile component. To verify the explanation, the ratios of liquid density to vapor density, i.e., multipliers to evaluate the vapor volume generated from the more volatile liquid of a fixed volume, were compared. Little difference between 121, 121 and 138 for FC72/water, Novec649/water and Novec7200/water, respectively, is consistent with the coincidence of wall temperatures at high heat flux.

Figure 9 illustrates qualitatively the trends for the nucleate boiling of immiscible mixtures on the horizontal flat plate when the liquid layer of the more volatile component with higher density is small before the heating. Nucleate boiling characteristics can be classified into two regimes; the “more-volatile-dominated regime” and the “less-volatile-dominated regime.” In the more-volatile-dominated regime, nucleate boiling of the more volatile component dominates the heat transfer. The more volatile components have, in general, low CHF values and burnout occurs easily at low heat flux. If the layer thickness of the more volatile liquid is large, the value of CHF as a pure liquid gives almost the limit of heat removal. A large effect of subcooling on the increase in CHF cannot be expected because of low partial pressure of the less volatile component. On the other hand, the heat transfer can be continued without temperature excursion at higher heat flux when the layer thickness of the more volatile liquid is small. After the jump of surface temperature due to the tentative burnout in the more volatile liquid, named here ”intermediate burnout,” the heating surface is cooled again by the less volatile component. The heat transfer mode for the less volatile component is natural convection at moderate heat flux and nucleate boiling aided by the evaporated more volatile component at high heat flux. It is noteworthy that boiling or evaporation of the less volatile component can occur even though the surface superheat, defined by the saturation temperature of the less volatile component at the total pressure, is low or

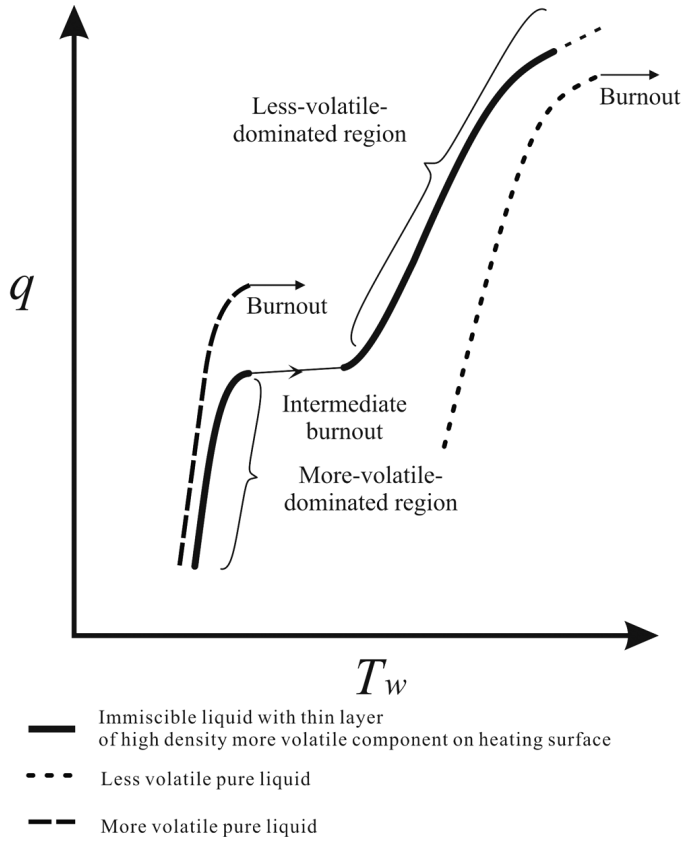

FIG. 9: Outline of heat transfer characteristics plotted by heat flux versus surface temperature when a thin layer of a more volatile component contacts the surface before heating.

even negative. This is because the vapor phase of the more volatile component enhances the evaporation of the less volatile liquid on the heating surface.

In the more-volatile-dominated regime, the boiling curve by using the temperature difference between the surface and the equilibrium temperature is almost the same as that for pure liquid, because the influence of the less volatile component occupied at the upper location on the heat transfer is not large even at the small layer thickness of 5 mm of the more volatile component (except in the case of Novec649/water). On the other hand, in the less-volatile-dominated regime, the superficial deterioration of heat transfer coefficient for immiscible mixtures is clear compared with that for the pure, less volatile component at the same (total) pressure, when the heat transfer coefficients are defined by using the equilibrium temperature or the measured temperature. This is mainly caused by the excessive temperature difference corresponding to the liquid subcooling resulting from the self-compression effect by the high partial vapor pressure of the more volatile component. The deteriorated heat transfer of the immiscible mixture is superficial and the heat transfer seems to be enhanced by the aid of the generated vapor from the more volatile liquid, because the heating surface temperature in the less-volatile-dominated regime is smaller than that for the pure, less volatile component at the same pressure.

The value of CHF, not the heat flux of intermediate burnout for the immiscible mixtures, is seriously influenced by the thickness of the liquid layer for the more volatile component. When the layer thickness of the more volatile component is small, the CHF is determined by the heat transfer to the subcooled, less volatile component. Because of high subcooling by high partial vapor pressure of the more volatile component, a drastic increase in CHF values is expected. When the layer thickness of the more volatile liquid is large, CHF does not deviate far from that for the pure, more volatile component because of low subcooling of the less volatile liquid.

Under optimized conditions, the boiling of immiscible mixtures reduces the surface temperature at the same pressure and simultaneously increases CHF from the value for the less volatile component. Additionally, nucleate boiling can be initiated without excessive increase of surface temperature by the aid of the thin layer of the more volatile liquid with low subcooling which contacts the surface before the heating.

7. CONCLUSIONS

To find a method to establish high-performance cooling systems, the boiling heat transfer and the critical heat flux of immiscible liquid mixtures were investigated by using FC72/water, Novec649/water, and Novec7200/water at 0.1 MPa. The components of the mixture liquids were horizontally stratified on a horizontal flat heating surface before the heating. The thicknesses of the liquid layers were varied as an important parameter. For thin layers of the more volatile liquid with higher density, the following heat transfer characteristics not clarified so far were obtained.

(i) Larger CHF values than that for pure water are obtained under the high subcooling condition of the less volatile liquid resulting from the compression effect by the high vapor partial pressure of the more volatile component.

(ii) The heating surface is covered by the layer of the more volatile liquid with higher density and the subcooling of the layer is small because of low vapor partial pressure of the less volatile component. The incipience of boiling is possible without excessive increase of surface temperature. The trend is necessary for the cooling of, e.g., inverters for electric automobiles with a large variation of power consumption.

(iii) A new phenomenon, "intermediate burnout," occurs accompanied by a small jump of surface temperature due to the burnout in the layer of the more volatile liquid. This phenomenon occurs when the tempertaure of the liquid located on the vapor film or on a large coalesced bubble is below the saturation temperature coprresponding to the total pressure. On the other hand, the gradual increase of the heating surface temperature keeping the steady state by the stepwise increase of heat flux is possible when both of the component liquids are physically well mixed. The stable heat transfer is continued again at higher heat flux by the penetration of the highly subcooled, less volatile liquid into the heating surface.

(iv) In the less-volatile-dominated regime at the heat flux larger than that for intermediate burnout, the surface temperature is lower than that for a pure, less volatile liquid at the same pressure. This is because bubbles or vapor slugs of a more volatile component enhance the evaporation of the less volatile liquid. This trend is not reflected in the heat transfer coefficients defined by using the equilibrium temperatures or the measured temperatures which show only superficial deterioration due to the high subcooling of the less volatile liquid.

The self-sustaining high subcooling of the less volatile liquid brings the first advantages of great importance described above. The more volatile component introduced to pressurize the less volatile liquid produces the second advantage. Furthermore, the decrease of surface temperature is possible also at a pressure higher than atmospheric pressure, which prevents the mixing of incondensable gases from the outside of the container. Because of these features, the immiscible mixtures have a large potential to become working media for the high-performance cooling systems including those of a flow boiling system.

REFERENCES

Abe, Y., Thermal management with phase change of self-rewetting fluids, In *Proc. of IMECE2005*, 2005.

Bonilla, C. F. and Eisenberg, A. A., Heat transmission to boiling binary mixtures, *Industrial Eng. Chem.*, vol. **40**, pp. 1113–1122, 1948.

Bragg, J. R. and Westwater, J. W., Film boiling of immiscible liquid mixture on a horizontal plate, *Heat Transfer 1970, Prof. Fourth International Heat Transfer Conference*, vol. **6**, B7.1, 1970.

Bulanov, N. V. and Gasanov, B. M., Peculiarities of boiling of emulsions with a low-boiling disperse phase, *High Temp.*, vol. **44**, no. 2, pp. 267–282, 2006.

Charles, M. E. and Redberger, P. J., The reduction of pressure gradients in oil pipelines by the addition of water: Numerical analysis of stratified flow, *Can. J. Chem. Eng.*, vol. **40**, no. 2, pp. 70–75, 1962.

Clark, A. F. and Shapiro, A., U.S. Patent no. 2,533,878, 1949-5-31, 1949.

Everage, A. E., Theory of stratified bicomponent flow of polymer melts, I. Equilibrium Newtonian tube flow, *Trans. Soc. Rheol.*, vol. **17**, pp. 629–646, 1973.

Filipczak, G., Troniewski, L., and Witczak, S., Pool boiling of liquid-liquid multiphase systems, In *Evaporation, Condensation and Heat Transfer*, A. Ahsan, ed., InTech, 2012, available at http://www.intechopen.com/books/evaporation-condensation-and-heat-transfer/pool-boiling-of-liquid-liquid-multiphase-systems.

Gorenflo, D., Gremer, F., Danger, E., and Luke, A., Pool boiling heat transfer to binary mixtures with miscibility gap: Experimental results for a horizontal copper tube with 4.35 mm O. D., *Exp. Therm. Fluid Sci.*, vol. **25**, no. 5, pp. 243–254, 2001.

Hasson, D., Mann, U., and Nir, A., Annular flow of two immiscible liquids, I. Mechanisms, *Can. J. Chem. Eng.*, vol. **48**, pp. 514–520, 1970.

Hasson, D. and Nir, A., Annular flow of two immiscible liquids, II. Analysis of core liquid ascent, *Can. J. Chem. Eng.*, vol. **48**, pp. 521–526, 1970.

Incropera, F. P. and DeWitt, D. P., *Fundamentals of Heat and Mass Transfer*, 5th ed., New York: John Wiley & Sons Inc., 2002.

Ivey, H. J. and Morris, D. J., Critical heat flux and subcooled pool boiling in water at atmospheric pressure, In *Proc. of Third International Heat Transfer Conference*, vol. **3**, pp. 129–142, 1966.

Minagawa, N. and White, J. L., Co-extrusion of unfilled and TiO_2-filled polyethylene: Influence of viscosity and die cross-section on interface shape, *Polym. Eng. Sci.*, vol. **15**, pp. 825–830, 1975.

Mori, Y. H., Configurations of gas-liquid two-phase bubbles in immiscible liquid media, *Int. J. Multiphase Flow*, vol. **4**, no. 4, pp. 383–396, 1978.

Nukiyama, S., The maximum and minimum values of the heat Q transmitted from metal to boiling water under atmospheric pressure, *J. Jpn. Soc. Mech. Eng.*, vol. **37**, pp. 367–374, 1934.

Prigogine, I. and Dfay, R., *Chemical Thermodynamics*, London: Longmans Green and Co., 1954.

Roesle, M. L. and Kulacki, F. A., An experimental study of boiling in dilute emulsions, Part A: Heat transfer, *Int. J. Heat Mass Transfer*, vol. **55**, nos. 7–8, pp. 2160–2165, 2012.

Russell, T. W. F. and Charles, M. E., The effect of the less viscous liquid in the laminar flow of two immiscible liquid, *Can. J. Chem. Eng.*, vol. **37**, no. 1, pp. 18–24, 1959.

Russell, T. W. F., Hodgson, G. W., and Govier, G. W., Horizontal pipeline flow of mixtures of oil and water, *Can. J. Chem. Eng.*, vol. **37**, no. 1, pp. 9–17, 1959.

Sakai, T., Yoshii, S., Kajimoto, K., Kobayashi, H., Shinmoto, Y., and Ohta, H., Heat transfer enhancement observed in nucleate boiling of alcohol aqueous solutions at very low concentration, In *Proc. of 14th International Heat Transfer Conference*, IHTC14-22737, 2010.

Shinmoto, Y., Miura, S., Suzuki, K., Abe, Y., and Ohta, H., Development of advanced high heat flux cooloing system for power electronics, In *Proc. of InterPACK' 09*, IPACK2009-89082, DVD-ROM, 2009.

Southern, J. H. and Ballman, R. L., Stratified bicomponent flow of polymer melts in a tube, *Appl. Polym. Symp.*, vol. **20**, pp. 175–189, 1973.

Southern, J. H. and Ballman, R. L., Additional observations on stratified bicomponent flow of polymer melts in a tube, *Appl. Polym. Symp.*, vol. **13**, pp. 863–869, 1975.

Stephan, K. and Körner, M., Evaluation of heat transfer in evaporating binary liquid mixtures, *Chem. Ing. Tech.*, vol. **41**, pp. 409–417, 1969.

Sump, G. D. and Westwater, J. W., Boiling heat transfer from a tube to immiscible liquid-liquid mixtures, *Int. J. Heat Mass Transfer*, vol. **14**, pp. 767–779, 1971.

Suzuki, K., Kokubu, T., Nakano, M., Kawamura, H., Ueno, I., Shida, H., and Ogawa, O., Enhancement of heat transfer in subcooled flow boiling with microbubble emission, *Exp. Therm. Fluid Sci.*, vol. **29**, pp. 827–832, 2005.

Tipman, E. and Hodgson, G. W., Sedimentation in emulsions of water in petroleum, *J. Pet. Technol.*, vol. **8**, no. 9, pp. 91–93, 1956.

Van Stralen, S. J. D., Heat transfer to boiling binary liquid mixtures at atmospheric and subatmospheric pressures, *Chem. Eng. Sci.*, vol. **5**, pp. 290–296, 1956.

Van Wijk, W. R., Vos, A. S., and Van Stralen, S. J. D., Heat transfer to boiling binary liquid mixtures, *Chem. Eng. Sci.*, vol. **5**, pp. 68–80, 1956.

Vochten, R. and Petre, G., Study of the heat of reversible adsorption at the air-solution interface, *J. Colloid Interface Sci.*, vol. **42**, pp. 320–327, 2005.

White, J. L. and Lee, B. L., Theory of interface distortion in stratified two-phase flow, *Trans. Soc. Rheol.*, vol. **19**, pp. 457–479, 1975.

Yu, H. S. and Sparrow, E. M., Experiments on two-component stratified flow in a horizontal duct, *J. Heat Transfer*, vol. **91**, pp. 51–58, 1969.

Interfacial Phenomena and Heat Transfer, 1 (1): 81–92 (2013)

INSTABILITY AND RUPTURE OF THIN LIQUID FILMS ON SOLID SUBSTRATES

Vladimir S. Ajaev

Department of Mathematics, Southern Methodist University, Dallas, Texas 75275, USA,
E-mail: ajaev@smu.edu

Studies of rupture of thin liquid films on solid surfaces are important for modeling of multiphase flows in microfluidic devices, heat exchange systems, mining industry, and for biomedical applications such as dynamics of the tear film in the eye. In the present study we review theoretical work on film rupture and discuss its comparison with some recent experiments. Conditions for the break-up of thin liquid films by London-van der Waals dispersion forces, electrostatic effects, and thermocapillary instability are discussed.

KEY WORDS: *surface tension, viscous flow, disjoining pressure, thermocapillarity*

1. INTRODUCTION

Mathematical models of instability of a liquid film between a deformable fluid interface and a solid wall are important for a number of applications of multiphase flow. The fluid interface in the present context is a boundary between liquid and vapor or gas, although some of the results discussed here are applicable to liquid-liquid interfaces as well. When the interface approaches the wall, the film can rupture, resulting in the formation of a three-phase contact line. The overall dynamics of many types of multiphase flows encountered in applications depends on these local phenomena. In microfluidic devices, drops and bubbles transported through a channel can slow down as a result of rupture of the film separating the fluid interface and the wall since the presence of such film is essential for maintaining the microfluidic transport efficiency, as discussed, e.g., in Ajaev and Homsy (2006). In cooling systems based on thin-film flows driven by either gravity or shear stresses at the liquid-gas interface, formation of dry spots results in significant reduction of heat flux from the heated wall, as shown experimentally by Kabov (2000). Liquid films flowing under gravity over a localized heater on vertical or inclined flat plates rupture for sufficiently high values of the heat flux generated by the heater. These experimental observations are important for developing guidelines to avoid rupture in cooling systems for industrial applications.

Stability of thin films separating solid and gas phases is important for studies of interaction between solid particles and gas bubbles. Of particular importance for these studies are the conditions when particles become attached to air bubbles as a result of rupture of the liquid film separating them. The main application of this work is froth flotation (Nguyen and Schulze, 2004; Rao, 2004), an important step in mineral processing during which particles of valuable minerals in a liquid tank become attached to rising air bubbles and thus separated from the gangue, i.e., commercially worthless part of the raw ore deposit that remains near the bottom of the tank. Typical minerals in froth flotation are metal sulfides, which then undergo further processing until pure metals such as copper, lead, and zinc are produced. Similar techniques are successfully applied in the coal industry and, more recently, for the de-inking process in paper recycling (Drelich and Miller, 2001).

Several recent studies of liquid film rupture have been motivated by dynamics of the tear film in the eye and are discussed in detail in Braun (2012). The tear film forms after each blink and is essential for providing a high-quality optical surface at the front of the eye and also for protection against dust and bacteria. A medical condition called the dry-eye syndrome (DES) occurs when the tear film ruptures too quickly after the blink, usually within a few seconds. Understanding the causes of this rupture is essential for developing treatment strategies for DES.

2169–2785/13/$35.00 © 2013 by Begell House, Inc.

There are situations when the surface tension of an initially flat film is highly non-uniform, e.g., due to rapid localized heating or addition of surfactants. The models of film dynamics under these conditions are discussed by, e.g., Jensen and Grotberg (1992) and Ajaev and Willis (2006) and are beyond the scope of the present review. Our objective is to focus on situations when film breakup is a result of intrinsic instability rather than imposed surface tension gradients. Only liquid films on solid substrates are considered, so the topics of free film stability and bubble coalescence are not discussed. The review is organized as follows. We start by discussing the theoretical models of film rupture under the isothermal conditions. The two key mechanisms of growth of infinitesimal perturbations of the film surface are the London-van der Waals dispersion forces and the electrostatic effects; both of these are discussed in detail, followed by a survey of models of rupture by heterogeneous nucleation. Then, the break-up of nonisothermal films due to the effects of thermocapillarity is discussed under the conditions when the effects of phase change (evaporation or condensation) are negligible. A discussion of liquid film dry-out in situations when phase change is important, e.g., in the context of boiling, can be found in a recent monograph by Peles (2012). Finally, we provide a brief overview of experiments on film rupture and discuss their connection with the predictions of the theories. We do not, however, provide a comprehensive review of experimental studies of rupture since the main focus of the present paper is on the theoretical and numerical results.

2. INSTABILITY MECHANISMS FOR ISOTHERMAL FILMS

2.1 London-van der Waals Dispersion Forces

A uniform film of a nonpolar liquid on a solid substrate in the absence of contamination and electric charges can become unstable for sufficiently small thickness d (typically of the order of 100 nm or less) due to the action of the London-van der Waals dispersion forces. Their origin is due to fluctuations of dipole moments of molecules, leading to electromagnetic interactions of dipole-dipole type as discussed by Derjaguin et al. (1987) and Israelachvili (2011). The continuum description of these interactions involves corrections to the chemical potential in the liquid film in the form

$$\mu = \mu_0 - \nu_l \Pi, \tag{1}$$

where μ_0 is the chemical potential of the liquid in the bulk phase (i.e., in the limit of macroscopic film thickness d), ν_l is the molar volume of the liquid, and Π is the so-called disjoining pressure, usually written in the form

$$\Pi = -\frac{A}{d^3}. \tag{2}$$

Here A is a dimensional constant which depends on the properties of the fluids involved and the solid material. It is referred to as the Hamaker constant and its values are typically on the order of 10^{-20} J. Eq. (2) is valid for values of film thickness d much smaller than the characteristic wavelength λ_a in the absorption spectrum of the liquid. The values of λ_a can be obtained by studying the absorption of electromagnetic waves by the dielectric liquid medium at different wavelengths. In the opposite limit of $d \gg \lambda_a$, a different analytical approximation can be derived, leading to disjoining pressure being inversely proportional to d^4. The latter approximation incorporates the effects of retardation (due to the finite value of the speed of light) in the description of fluctuating electromagnetic fields.

The London-van der Waals forces can lead to the instability of the liquid film on a solid substrate when the Hamaker constant A is positive. This instability has been investigated theoretically by several authors. Early models of the instability developed by Ruckenstein and Jain (1974) address the linear stability criteria, determined by the interplay between the disjoining pressure and the surface tension. The mechanism of the instability can be understood by considering a small perturbation of an initially flat fluid interface, as sketched in Fig. 1. The disjoining pressure Π at a point A just below the interface is lower in magnitude than at a point B since the film thickness is greater at the point A. Thus, the flow driven by disjoining pressure will be directed from B to A, resulting in further increase of the film thickness at the point A and film thinning at the point B. The surface tension, however, is stabilizing since the curvature κ is negative at the point A and positive at the point B. Note that we use a two-dimensional model here, so possible variations of curvature in the direction normal to the plane of the sketch are not considered. Based on the

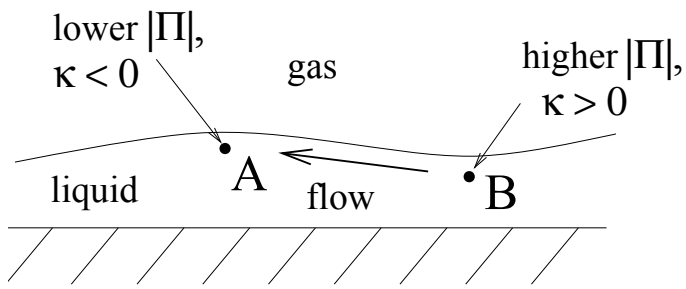

FIG. 1: A sketch illustrating the mechanism of rupture due to London van der Waals forces for a thin liquid film on a flat solid substrate.

linear theory, a sinusoidal small perturbation of a wave number k turns out to have positive growth rate under the condition

$$k^2 < \frac{3A}{\sigma d^4}, \tag{3}$$

where σ is the surface tension. The fastest growing mode of the linear stability theory corresponds to $k^2 = 3A/(2\,\sigma d^4)$ so its wavelength λ is given by

$$\lambda = 2\pi d^2 \sqrt{\frac{2\sigma}{3A}}. \tag{4}$$

Since the quantity $\sqrt{A/\sigma}$ is of the order of molecular length scales, the wavelength λ is much larger than the thickness for films considered within the continuum-level description. Therefore, a lubrication-type approximation can be used to describe the nonlinear dynamics of such films. In this approach, developed in the pioneering works of Williams and Davis (1982) and Burelbach et al. (1988), the fluid flow problem is reduced to a single evolution equation for the film thickness. Based on the numerical solution of this equation with a sinusoidal initial perturbation, it was found that the growth rate of the perturbation in the nonlinear regime is significantly higher than the value predicted by the linear stability theory. The simulations in the nonlinear regime were conducted up to the point when the minimum film thickness reached zero, resulting in the determination of the rupture time.

The work of Zhang and Lister (1999) focused on further development of the techniques for mathematical modeling of nonlinear rupture driven by the London-van der Waals dispersion forces. In particular, they found self-similar solutions describing final stages of film rupture, which incorporate the physical effects of disjoining pressure, surface tension, and viscosity. The minimum film thickness at the late stages of rupture is shown to decrease with time t as $(t_R - t)^{1/5}$, where t_R is the rupture time. Furthermore, a numerical finite-difference method for accurate simulations of rupture dynamics was developed, based on nonuniform spatial mesh and adaptive time stepping. Alternatively, the so-called positivity-preserving numerical schemes (Zhornitskaya and Bertozzi, 1999) can be used to accurately detect the point of liquid film rupture without extensive mesh refinement.

The lubrication-type approach has been extended to three-dimensional situations, when the interface is represented by an evolving two-dimensional surface, and is used by, e.g., Sharma and Khanna (1998) and Schwartz et al. (2001) to study complex patterns formed as a result of breakup of thin liquid films on solid substrates.

2.2 Electrostatic Effects

The theoretical studies of the London-van der Waals rupture discussed in the previous subsection are important for establishing the lubrication-type framework for stability theories and for developing advanced analytical and numerical methods used to describe film rupture. However, the results of these studies are not directly applicable to several situations of practical importance. Since the Hamaker constant for films of water and aqueous solutions on typical substrates is in fact *negative*, such films cannot rupture through the London-van der Waals mechanism. Thus, other mechanisms of instability have to be investigated in order to explain experimentally observed rupture. Several studies reviewed by, e.g., Churaev (2003) pointed to the importance of the electrostatic effects. Let us briefly review the

models of aqueous solutions containing ions and then discuss their application to electrostatically driven thin film rupture.

Electric charges are always present in water and aqueous solutions in the form of ions. Contamination and chemical reactions of dissociation, both in the bulk (for water molecules) and near the surface (for various surface groups) are the sources of ions. For example, when water is in contact with glass, ionization of the solid leads to the appearance of negatively charged surface groups. Similar processes take place at metal surfaces covered with oxide layers. Consider a flat solid surface carrying a negative electric charge of uniform density. It is clear that cations in the liquid will be attracted to the solid and anions repelled from it, but thermal motion will counteract these tendencies. As a result of the balance between these two physical effects, a certain equilibrium distribution of electric charges will be established near the solid, with excess positive charge near the solid-liquid interface, as schematically shown in Fig. 2. Liquid is assumed to be electrically neutral away from boundaries, so the density of electric charges will be nonzero only in the so-called electrical double layer. Assuming there are several types of ions in the liquid, of valencies z_i, the condition of constant electrochemical potential (Probstein, 1989) leads to the following formula for ion concentrations n_i in terms of the electric potential ψ:

$$n_i = n_i^{(0)} \exp\left(-\frac{z_i e\,\psi}{k_B T}\right). \tag{5}$$

Here e is the elementary charge, k_B is the Boltzmann constant, T is temperature, and $n_i^{(0)}$ denotes ion concentrations under the condition of $\psi \to 0$, which is usually far away from the solid surface. By combining the classical Poisson's equation of electrostatics and Eq. (5), the Poisson-Boltzmann equation for the field is obtained in the form

$$\nabla^2\psi = -\sum_i \frac{z_i e n_i^{(0)}}{\varepsilon} \exp\left(-\frac{z_i e\psi}{k_B T}\right), \tag{6}$$

where ε is the dielectric permittivity of the liquid. Both analytical and numerical methods for solving Eq. (6) can be used, as discussed, e.g., in Probstein (1989) and Kirby (2010). Without getting into the details of these methods, we note that for a flat uniformly charged solid surface in contact with a semi-infinite region of electrolyte, the characteristic width of the diffuse part of the double layer is defined by the Debye length,

$$\lambda_D = \left(\frac{e^2}{\varepsilon k_B T}\sum_i n_i^{(0)} z_i^2\right)^{-1/2}. \tag{7}$$

Typical values of the Debye length are between 1 and 100 nm for ionic solutions and about 1 micron for pure water. For a liquid film on a charged solid substrate, the electrostatic effects are negligible when the film thickness is much

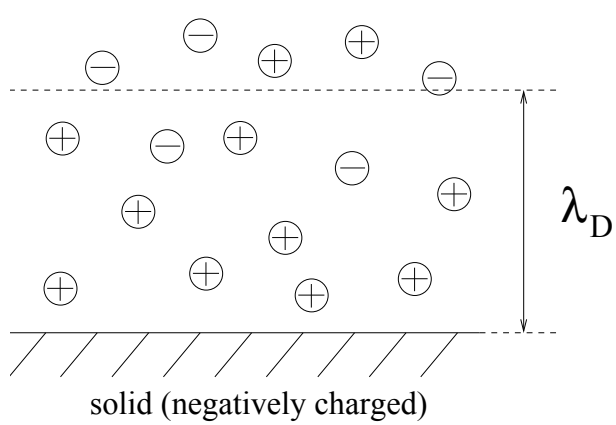

FIG. 2: Formation of diffuse layer of charge near a negatively charged solid surface. The characteristic thickness of the diffuse layer is the Debye length λ_D, defined by Eq. (7).

larger than λ_D, but become significant when the two are comparable so that there is an overlap of the double layers formed near the solid surface and the liquid-gas interface. In particular, the electrostatic effects in such films can result in rupture when the signs of charge densities at the two interfaces are opposite. While early theoretical works often assumed that liquid-gas interfaces are not charged (de Gennes, 1985), experimental investigations by, e.g., Ciunel et al. (2005) and Takahashi (2005) present convincing evidence that air-water interfaces carry negative electric charge. Therefore, water films on positively charged solid substrates can rupture due to electrostatic effects.

The linear and nonlinear stability theories for thin electrolyte films are topics of current research. Some preliminary results obtained by Ketelaar and Ajaev (2012) using the linearized version of Eq. (6), called the Debye-Hückel approximation, indicate that for the important case of fixed substrate potential ψ_0 and fixed charge density at the liquid-air interface σ_{el}, the film is linearly stable under the conditions

$$-\mathrm{csch}\frac{d}{\lambda_D} < \frac{\sigma_{el}\lambda_D}{\varepsilon\psi_0} < \sinh\frac{d}{\lambda_D}. \tag{8}$$

This result is based on the formula for the electrostatic component of disjoining pressure,

$$\Pi_{el} = \frac{\varepsilon\psi_I^2}{2\lambda_D^2}, \tag{9}$$

where ψ_I is the electrostatic potential at the liquid-air interface found by solving the linearized version of (6). The sign of the derivative of Π_{el} with respect to the film thickness determines linear stability, leading to stability bounds expressed by Eq. (8).

2.3 Nucleation and the Role of Nanobubbles

In the linear stability theories discussed in the previous sections, the initial perturbation is assumed infinitesimal, which is certainly reasonable if the perturbations are induced by thermal fluctuations and have typical amplitudes of less than 1 nm, as measured by, e.g., Sanyal et al. (1991) using the x-ray scattering techniques. However, in a typical experimental setup, much stronger perturbations are usually present due to contamination by tiny dust particles or surfactant molecules, the presence of small gas bubbles in the liquid and defects on the solid substrates. In the mathematical language, all these factors lead to finite-amplitude rather than infinitesimal perturbations. When a linearly stable state corresponds to a local but not global free energy minimum, i.e., the system is metastable, a sufficiently strong perturbation will result in a transition to a more energetically favorable configuration.

Following de Gennes et al. (2004), let us discuss the conditions when a uniform liquid film on a flat solid substrate is metastable. The Gibbs free energy per unit surface area for the liquid film of uniform thickness d is given by $\sigma + \sigma_{sl} + \rho g d^2/2$, where σ_{sl} is the surface tension at the solid-liquid interface and the last term is the hydrostatic contribution, g being the acceleration of gravity and ρ being the liquid density; the disjoning pressure is neglected here. The film is metastable when a configuration with partially dry solid corresponds to a lower energy. Suppose α is the fraction of the solid covered by nearly flat regions of the liquid film with dry regions between them, as illustrated in the cross-sectional sketch in Fig. 3. The total free energy of the system in this configuration is

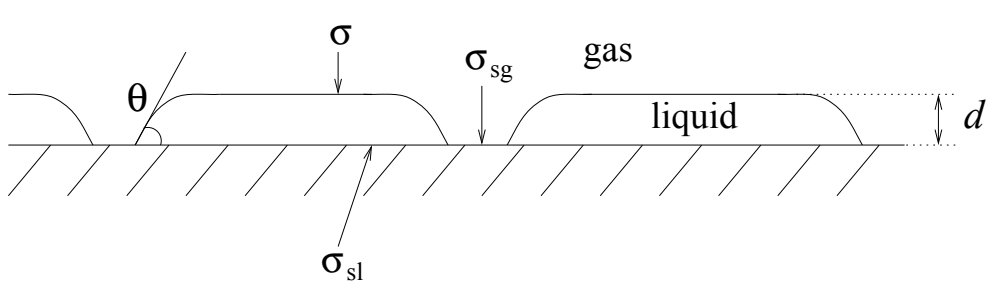

FIG. 3: Sketch of a solid surface covered by liquid film regions with dry areas between them.

$$F = \alpha \left(\sigma + \sigma_{sl} + \frac{\rho g d^2}{2} \right) + (1 - \alpha)\sigma_{sg}, \tag{10}$$

where σ_{sg} is the surface tension at the solid-gas interface. Here we assume that the difference between the total areas of the liquid-gas and liquid-solid interfaces is negligible, which is appropriate when the thickness d is much smaller that the horizontal extent of the wetted regions. For a fixed volume of the liquid, α and d are not independent but rather related by $\alpha d = c$, where c is a constant. Then, the free energy F can be expressed as a function of a single variable d,

$$F = \frac{c}{d} \left(\sigma + \sigma_{sl} + \frac{\rho g d^2}{2} \right) + \left(1 - \frac{c}{d} \right) \sigma_{sg}. \tag{11}$$

A local minimum of this function is reached at

$$d_{\mathrm{crit}} = 2\sqrt{\frac{\sigma}{\rho g}} \sin \frac{\theta}{2}, \tag{12}$$

where we use the equilibrium contact angle θ, related to the surface tensions through the Young's equation,

$$\sigma \cos \theta = \sigma_{sg} - \sigma_{sl}. \tag{13}$$

For values of d below d_{crit}, the free energy of the configuration shown in Fig. 3 is lower than that of the uniform flat film and therefore the latter is metastable. The argument here is based on comparison of free energies of static configurations, so we use the equilibrium rather than dynamic contact angle. We assume that the film is macroscopic and therefore the disjoining pressure effects are negligible, although these effects can be incorporated into the model by suitable modification of the expression for the free energy, as discussed in de Gennes et al. (2004) and Brochard Wyart and Daillant (1990). The breakup of metastable films is usually characterized by random distribution of dry patches and is often referred to as heterogeneous nucleation.

While the theory of rupture by nucleation is well established, the issue of what provides the actual mechanism for nucleation in a particular experiment is not always clear. The studies of Schulze et al. (2001) and Stoeckelhuber et al. (2004) pointed to the importance of nanobubbles for rupture of thin liquid films on hydrophobic solid substrates. The presence of nanobubbles on hydrophobic substrates was suggested by Yakubov et al. (2000) as an explanation for jumps seen in the plots of the interaction force between two hydrophobic surfaces versus the separation between them. Images of arrays of nanobubbles were obtained by Tyrrell and Attard (2001) using the data from Atomic Force Microscope (AFM) measurements. To exclude the possibility of nanobubbles being an artifact of the AFM measurement techniques, as suggested by some critics, Karpitschka et al. (2012) confirmed their existence using a nonintrusive optical method. However, the role of nanobubbles in the rupture process still remains a matter of some controversy due to lack of simultaneous observation of nanobubbles and interfacial instability leading to film breakup.

It is interesting to note that the presence of nanobubbles also provides a possible explanation for experimental results showing attraction between hydrophobic solid-liquid interfaces not explained by the standard London-van der Waals or electrostatic models of interaction. A common approach to theoretical interpretation of these results was to introduce the so-called long-range hydrophobic attraction. While the theory of hydrophobic interaction at very short distances of the order 10 nm is well established, the physical origin of the long-range hydrophobic attraction has not been clarified. Meyer et al. (2006) point out that the nanobubbles or presence of charge nonuniformities at the solid boundaries can explain many previous experimental results on the long-range hydrophobic attraction without the need to introduce any new physical effects.

3. FILM RUPTURE DUE TO THERMOCAPILLARITY

When a liquid film is on a heated surface, the situation is more complicated than the isothermal case. First, evaporation is likely to play a role, resulting in gradual thinning of the layer. Second, even for layers of uniform (or nearly uniform) thickness, the liquid in the film is not necessarily at rest. Formation of convection patterns in such layers is possible

when the Marangoni number is above a critical value, as discussed, e.g., in Nepomnyashchy et al. (2002). The studies of film rupture in heated layers can then be divided into two categories, depending on the nature of the base state. If the base state corresponds to fluid without any convection patterns, the approach to stability analysis and nonlinear simulations is similar to the isothermal case and is discussed in detail, e.g., in Oron and Rosenau (1992) [see also Oron et al. (1997) for a review].

For the base state involving convection patterns, the coupling between film deformations and changes in these patterns has to be taken into account. Boos and Thess (1999) considered such coupling in a two-dimensional configuration in the limit of small Reynolds number and used the boundary integral method to describe the viscous flow in the film and interface deformation. Oron (2000) used the long-wave approach to study the three-dimensional evolution of convection patterns in films with deforming interface on a uniformly heated substrate. The approach has been extended to the case of nonuniform heating of the substrate by Yeo et al. (2003).

4. EXPERIMENTAL STUDIES

Since the main focus of the present review is on mathematical models of thin films, we do not attempt to provide a comperensive review of the broad subject of experimental studies of film rupture. Instead, we briefly discuss several well-known works which provided the experimental confirmation of the models discussed in the present review and then proceed to survey several recent experimental studies which we believe will stimulate the development of novel mathematical models.

4.1 Polymers and Molten Metals

It has been well established that the Hamaker constant for polystyrene films on silicon substrates is positive, so this system was the focus of a number of studies of rupture driven by London-van der Waals dispersion forces, starting with the pioneering experiments of Reiter (1992). However, in these early experiments it turned out to be difficult to distinguish between truly unstable films, ruptured via amplification of surface deformations by London-van der Waals dispersion forces, and metastable films ruptured via heterogeneous nucleation. Bischof et al. (1996) used molten metal films on fused silica substrate to obtain experimental observation of both rupture mechanisms in the same system. The dewetting of polymer films was revisited by Xie et al. (1998) who clarified the different rupture regimes for this experimental system. Thiele et al. (1998) were able to observe both mechanisms of rupture in evaporating films of collagen solution, with heterogeneous nucleation being the dominant mechanism at higher values of the thickness.

4.2 Isothermal Films of Water and Aqueous Solutions

Early experimental studies of rupture of aqueous salt solutions were conducted by Blake and Kitchener (1972). They used a clean silica surface, on which water is perfectly wetting, and methylated silica which is hydrophobic. For both cases, stable films were observed for a range of salt concentrations, with equilibrium thickness decreasing as the concentration was increased. For methylated silica, the films lost stability and ruptured at sufficiently high concentration. For example, in films of aqueous solution of KCl on methylated silica, the breakup was observed at the concentration of 0.86×10^{-2} kg $\cdot$ mol $\cdot$ m^{-3} and the minimum recorded stable film thickness was 64 nm. Film thickness measurements were conducted using interferometry.

Detailed studies of rupture of thin aqueous liquid films were conducted by Schulze et al. (2001) and Stoeckelhuber et al. (2004) using microinterferometry to record film thickness and high-speed camera to record rupture and subsequent growth of dry patches. For the regime when both London-van der Waals and electrostatic interactions are stabilizing, metastable films were observed and their breakup was explained by the presence of nanobubbles. To study unstable films, the sign of electrical charge of the substrate was altered by adding $AlCl_3$ to the KCl solution. As a result, Al^{3+} ions were adsorbed at the silica surfaces and made it positively charged. Since the charge at the liquid-air interface is negative, this resulted in rupture through the amplification of thermal fluctuations as the film is linearly unstable.

4.3 Rupture of Films on Heated Surfaces

Orell and Bankoff (1971) studied ethanol films on a heated substrate and slowly increased the heat flux until the film ruptured. Heating was provided by an embedded nichrome strip, and the temperature was measured using thermocouples. The threshold heat flux for rupture was found to increase with film thickness. Convection patterns were observed prior to rupture.

Burelbach et al. (1990) investigated rupture of a silicon-oil layer on a steel plate experimentally and made comparisons with the long-wave stability analysis. They used a long heater to obtain a nearly two-dimensional picture of the flow. They also observed a thin film (of thickness less than 1 μm) on the macroscopically dry area of the substrate, but the accuracy of the experimental measurement of film thickness did not allow them to obtain data on the exact values of such thickness. Extensive experimental studies of films with thermocapillary patterns were conducted by VanHook et al. (1997) and included the experimental recordings of film rupture. A detailed review of the literature on the topic of experimental observations of thermocapillary instabilities is given by Schatz and Neitzel (2001).

Studies of rupture of liquid films flowing down vertical or inclined heated surfaces have been conducted for a range of heating intensities and flow conditions by Kabov (2000), Chinnov et al. (2001), and Zaitsev et al. (2007). A remarkable feature of this configuration is the formation of regular structures of rivulets not seen in the isothermal films (Kabov, 1998; Chinnov and Kabov, 2003); the rivulets are separated by thin films covering the solid. The rupture in such films was observed by Kabov (2000) and Zaitsev and Kabov (2005). Zaitsev et al. (2007) used fiber optical thickness probe to investigate rupture for a range of flow and heating conditions. They conducted experiments with films of water flowing down an inclined plane at inclination angles between 3° and 10°. Heating was suppplied by a heater of dimensions 150 mm × 150 mm for a range of flow rates.

The thickness is measured using the noncontact fiber optical probe placed above the film. The position of the film surface is found from the reflection of a light beam from the film surface. The light beam from a halogen lamp travels through the emitting optical fiber and the reflected light is received by another optical fiber and then sent to the photodetector. The local film thickness is found based on the intensity of the reflected signal. A more detailed description of the experimental technique can be found, e.g., in Zaitsev and Kabov (2005).

Without heating, the usual flow patterns are observed, in agreement with previous results on isothermal films (Alekseenko et al., 1994). When the heating is introduced, formation of regular structure of long rivulets separated by thin films is observed, similar to the ones seen in previous experimental studies of flows on inclined heated surfaces (Chinnov and Kabov, 2003). Note that film thickness between rivulets depends on the heat flux. Then, a rupture was observed in the thin films that separated the rivulets, as seen in Fig. 4. The Reynolds number referenced in the caption is based on the specific liquid flow rate. The critical intermediate film thickness was detected at the values of 60 μm independent from overall configuration and parameters such as the Reynolds number.

The critical film thickness for rupture of the nearly flat liquid layer on a solid substrate can be estimated from the following considerations. Suppose the substrate is maintained as a constant temperature T_s, the gas phase above the liquid film and far away from the liquid surface is at temperature T_∞, and the heat transfer coefficient from the liquid to the gas phase is α_{th}. Based on the linear stability theory prediction for the growth rate of a sinusoidal perturbation of a wavelength L [see, e.g., Eq. (2.65) in Oron et al., (2007)], the condition of stability can be written as

$$h_{cr} = \frac{3L^2\alpha_{th}\gamma(T_s - T_\infty)}{4\pi^2\sigma k_{th}} \tag{14}$$

where k_{th} is the thermal conductivity of the liquid, and γ is the slope of the surface tension curve versus temperature. Gravity is neglected since in the experiment it does not play a significant role, as was verified by varying the inclination angle. Using the value $\gamma = 1.5 \times 10^{-4}$ N/mK, the rough estimate of the wavelength as $L = 5$ mm, and the relation between the measured heat flux q and the heat loss coefficient, $q = \alpha_{th}(T^i - T_\infty)$ (T^i is the interfacial temperature), the critical thickness value estimate is consistent with the experimentally observed values.

Studies of evaporating films on different heated surfaces were also conducted by Gong et al. (2011). They found the value for critical thickness for water to be in the range of 60–150 μm.

While there is a significant amount of data on rupture on heated surfaces, as discussed above, the development of mathematical models for this situation is limited. This is especially true for configurations characterized by compli-

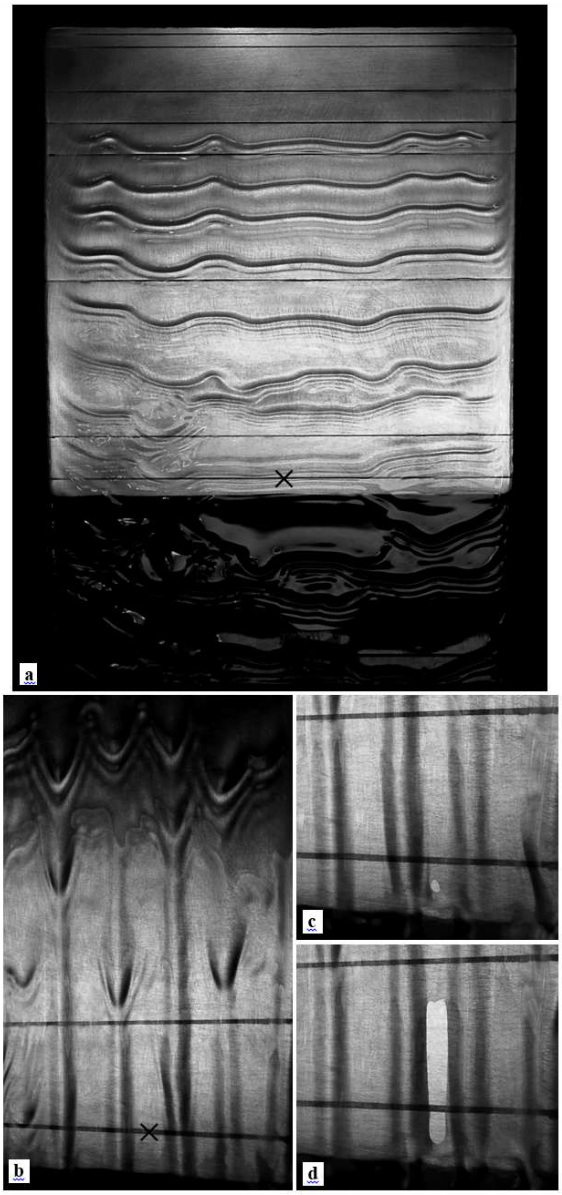

FIG. 4: Illustration of experimental observations of film rupture on a vertical wall at the Reynolds number equal to 20.6: (**a**) no heating; (**b**) formation of regular structures when the heater is on; (**c**) nucleation of dry patch; (**d**) growth of the dry patch between the rivulets. From Zaitsev et al. (2007).

cated interface shapes, i.e., regular structures, and also for situations when evaporation and condensation can play a significant role. Theoretical studies of such configurations offer an important direction for future research.

ACKNOWLEDGMENTS

The work was supported by a grant from the Russian Ministry of Science and Education (No. 8505). The author thanks Dr. D.V. Zaitsev for providing the experimental pictures shown in Fig. 4.

REFERENCES

Ajaev, V. S. and Homsy, G. M., Modeling shapes and dynamics of confined bubbles, *Annu. Rev. Fluid Mech.*, vol. **38**, pp. 277–307, 2006.

Ajaev, V. S. and Willis, D. A., Heat transfer, phase change, and thermocapillary flow in films of molten metal on a substrate, *Numer. Heat Transfer, Part A*, vol. **50**, pp. 301–313, 2006

Alekseenko, S. V., Nakoryakov, V. E., and Pokusaev, B. G., Wave flow of liquid films, New York: Begell House, 1994.

Bischof, J., Scherer, D., Herminghaus, S., and Leiderer, P., Dewetting modes of thin metallic films: Nucleation of holes and spinodal dewetting, *Phys. Rev. Lett.*, vol. **77**, pp. 1536–1539, 1996.

Blake, T. D. and Kitchener, J. A. Stability of aqueous films on hydrophobic methylated silica, *J. Chem. Soc., Faraday Trans. 1*, vol. **68**, pp. 1435–1442, 1972.

Boos, W. and Thess, A., Cascade of structures in long-wavelength Marangoni instability, *Phys. Fluids*, vol. **11**, pp. 1484–1494, 1999.

Braun, R. J., Dynamics of the tear film, *Annu Rev. Fluid Mech.*, vol. **44**, pp. 267–297, 2012.

Brochard Wyart, F. and Daillant, J., Drying of solids wetted by thin liquid films, *Can. J. Phys.*, vol. **68**, pp. 1084–1088, 1990.

Burelbach, J. P., Bankoff, S. G., and Davis, S. H., Nonlinear stability of evaporating/condensing liquid films, *J. Fluid Mech.*, vol. **195**, pp. 463–494, 1988.

Burelbach, J. P., Bankoff, S. G., and Davis, S. H., Steady thermocapillary flows of thin liquid layers, II, Experiment, *Phys. Fluids A*, vol. **2**, pp. 322–333, 1990.

Chinnov, E. A., Kabov, O. A., Muzykantov, A. V., and Zaitsev, D. V., Influence of plate inclination on heat transfer and breakdown of locally heated flowing liquid film, *Int. J. Heat Technol.*, vol. **19**, pp. 31–44, 2001.

Chinnov, E. A. and Kabov, O. A., Jet formation in gravitational flow of a heated wavy liquid film, *J. Appl. Mech. Theor. Phys.*, vol. **44**, pp. 708–715, 2003.

Churaev, N. V., Surface forces in wetting films, *Adv. Colloid Interface Sci.*, vol. **103**, pp. 197–218, 2003.

Ciunel, K., Armelin, M., Findnegg, G. H., and von Klitzing, R., Evidence of surface charge at the air/water interface from thin-film studies on polyelectrolyte-coated substrates, *Langmuir*, vol. **21**, pp. 4790–4793, 2005.

Derjaguin, B. V., Churaev, N. V., and Muller, V. M., *Surface Forces*, Plenum, New York: Plenum, 1987.

de Gennes, P. G., Wetting: Statics and dynamics, *Rev. Mod. Phys.*, vol. **57**, pp. 827–863, 1985.

de Gennes, P. G., Brochard Wyart, F., and Quere, D., *Capillarity and Wetting Phenomena: Drops, Bubbles, Pearls, Waves*, New York: Springer, 2004.

Drelich, J. and Miller, J. D., Improved flotation deinking of sorted office papers by flocculation of ink particles, *Progress in Paper Recycling*, vol. **11**, pp. 38–46, 2001.

Gong, S., Ma, W., and Dinh, T.-N., An experimental study of rupture dynamics of evaporating liquid films on different heater surfaces, *Int. J. Heat Mass Transfer*, vol. **54**, pp. 1538–1547, 2011.

Israelachvili, J. N., *Intermolecular and Surface Forces*, 3rd ed., Amsterdam: Elsevier, 2011.

Jensen, O. E. and Grotberg, J. B., Insoluble surfactant spreading on a thin viscous film: Shock evolution and film rupture, *J. Fluid Mech.*, vol. **240**, pp. 259–288, 1992.

Kabov, O. A., Formation of regular structures in a falling liquid film upon local heating, *Thermophys. Aeromech.*, vol. **5**, pp. 547–551, 1998.

Kabov, O. A., Breakdown of a liquid film flowing over the surface with a local heat source, *Thermophys. Aeromech.*, vol. **7**, pp. 513–520, 2000.

Karpitschka, S., Dietrich, S, Seddon, J. R. T., Zandvliet, H. J. W., Lohse, D., Riegler, H., Nonintrusive optical visualization of surface nanobubbles, *Phys. Rev. Lett.*, vol. **109**, p. 066102, 2012.

Ketelaar, C. and Ajaev, V. S., The effect of charge regulation on the stability of electrolyte films, *Bull. Am. Phys. Soc.*, vol. **57**, no. 17, 2012(preprint).

Kirby, B. J., *Micro- and Nanoscale Fluid Mechanics: Transport in Microfluidic Systems*, Cambridge: Cambridge University Press, 2010.

Meyer, E. E., Rosenberg, K. J., and Israelachvili, J., Recent progress in understanding hydrophobic interactions, *Proc. Natl. Acad. Sci. U.S.A.*, vol. **103**, pp. 15739–15746, 2006.

Nepomnyashchy, A. A., Velarde, M. G., and Colinet, P., *Interfacial Phenomena and Convection*, Boca Raton, FL: Chapman and Hall/CRC, 2002.

Nguyen, A. V. and Schulze, H. J., *Colloidal Science of Flotation*, New York: Marcel Dekker, 2004.

Orell, A. and Bankoff, S. G., Formation of a dry spot in a horizontal liquid film heated from below, *Int. J. Heat Mass Transfer*, vol. **14**, pp. 1835–1842, 1971.

Oron, A., Nonlinear dynamics of three-dimensional long-wave Marangoni instability in thin liquid films, *Phys. Fluids*, vol. **12**, pp. 1633–1645, 2000.

Oron, A., Bankoff, S. G., and Davis, S. H., Long-scale evolution of thin liquid films, *Rev. Mod. Phys.*, vol. **69**, pp. 931–980, 1997.

Oron, A. and Rosenau, P., Formation of patterns induced by thermocapillarity and gravity, *J. Phys. II*, vol. **2**, pp. 131–146, 1992.

Peles, Y., *Contemporary Perspectives on Flow Boiling Instabilities in Microchannels and Minichannels*, New York: Begell House, 2012.

Probstein, R. F., *Physicochemical Hydrodynamics: An Introduction*, Boston: Butterworth-Heinemann, 1989.

Rao, S. R., *Surface Chemistry of Froth Flotation: Fundamentals*, New York: Kluwer Academic/Plenum Publishers, 2004.

Reiter, G., Dewetting of thin polymer films, *Phys. Rev. Lett.*, vol. **68**, pp. 75–78, 1992.

Ruckenstein, E. and Jain, R. K., Spontaneous rupture of thin liquid films, *Chem. Soc: Faraday Trans.*, vol. **2**, pp. 132–147, 1974.

Sanyal, M. K., Sinha, S. K., Huang, K. G., and Ocko, B. M., X-ray-scattering study of capillary-wave fluctuations at a liquid surface, *Phys. Rev. Lett.*, vol. **6**, pp. 628–631, 1991.

Sharma, A. and Khanna, R., Pattern formation in unstable thin liquid films, *Phys. Rev. Lett.*, vol. **81**, pp. 3463–3466, 1998.

Schatz, M. and Neitzel, P.,Experiments on thermocapillary instabilities, *Annu. Rev. Fluid Mech.*, vol. **33**, pp. 33–127, 2001.

Schulze, H. J., Stoeckelhuber, K. W., and Wenger, A., The influence of acting forces on the rupture mechanism of wetting films – nucleation or capillary waves, *Colloids Interfaces, A: Physicochem. Eng. Aspects*, vol. **192**, pp. 61–72, 2001.

Schwartz, L. W., Roy, R. V., Eley, R. R., and Petrash, S., Dewetting patterns in a drying liquid film, *J. Colloid Interface Sci.*, vol. **234**, pp. 363–374, 2001.

Stoeckelhuber, K. W., Radoev, B., Wenger, A., and Schultze, H. J., Rupture of wetting films caused by nanobubbles, *Langmuir*, vol. **20**, pp. 164–168, 2004.

Takahashi, M., ζ-potential of microbubbles in aqueous solutions: Electrical properties of the gas-water interface, *J. Phys. Chem. B*, vol. **109**, pp. 21858–21864, 2005.

Thiele, U., Mertig, M., and Pompe, W., Dewetting of an evaporating thin liquid film: Heterogeneous nucleation and surface instability, *Phys. Rev. Lett.*, vol. **80**, pp. 2869–2872, 1998.

Tyrrell, J. W. G. and Attard, P., Images of nanobubbles on hydrophobic surfaces and their interactions, *Phys. Rev. Lett.*, vol. **87**, p. 176104, 2001.

VanHook, S. J., Schatz M. F., Swift J. B., McCormick, W. D., and Swinney, H. L., Long-wavelength surface-tension-driven Benard convection: Experiment and theory, *J. Fluid Mech.*, vol. **345**, pp. 45–78, 1997.

Williams, M. B. and Davis, S. H., Nonlinear theory of film rupture, *J. Colloid Interface Sci.*, vol. **90**, pp. 220–228, 1982.

Xie, R., Karim, A., Douglas, J. F., Han, C. C., and Weiss, R. A., Spinodal dewetting of thin polymer films, *Phys. Rev. Lett.*, vol. **81**, pp. 1251–1254, 1998.

Yakubov, G. E., Butt, H.-J., and Vinogradova, O. I., Interaction forces between hydrophobic surfaces: Attractive jump as an indication of formation of "stable" submicrocavities, *J. Phys. Chem. B*, vol. **104**, pp. 3407–3410, 2000.

Yeo, L. Y., Craster R. V., and Matar, O. K., Marangoni instability of a thin liquid film resting on a locally heated horizontal wall, *Phys. Rev. E*, vol. **67**, p. 056315, 2003.

Zaitsev ,D. V. and Kabov, O. A., Study of the thermocapillary effect on a wavy falling film using a fiber optical thickness probe, *Exp. Fluids*, vol. **39**, pp. 712–721, 2005.

Zaitsev, D. V., Rodionov, D. A., and Kabov, O. A., Study of thermocapillary film rupture using a fiber optical thickness probe, *Microgravity Sci. Technol.*, vol. **19**, pp. 100–103, 2007.

Zhang, W. W. and Lister, J. R., Similarity solutions for van der Waals rupture of a thin film on a solid substrate, *Phys. Fluids*, vol. **11**, pp. 2454–2462, 1999.

Zhornitskaya, L. and Bertozzi, A., Positivity-preserving numerical schemes for lubrication-type equations, *SIAM J. Numer. Anal.*, vol. **37**, pp. 523–555, 1999.